



NAVAL POSTGRADUATE SCHOOL

MONTEREY, CALIFORNIA

THESIS

**COMPOSITE CASE DEVELOPMENT FOR WEAPONS
APPLICATIONS AND TESTING**

by

Cassandra C. Mitchell

March 2015

Thesis Advisor:
Co-Advisor:

Young W. Kwon
John D. Molitoris

Approved for public release; distribution is unlimited

THIS PAGE INTENTIONALLY LEFT BLANK

REPORT DOCUMENTATION PAGE			Form Approved OMB No. 0704-0188	
Public reporting burden for this collection of information is estimated to average 1 hour per response, including the time for reviewing instruction, searching existing data sources, gathering and maintaining the data needed, and completing and reviewing the collection of information. Send comments regarding this burden estimate or any other aspect of this collection of information, including suggestions for reducing this burden, to Washington headquarters Services, Directorate for Information Operations and Reports, 1215 Jefferson Davis Highway, Suite 1204, Arlington, VA 22202-4302, and to the Office of Management and Budget, Paperwork Reduction Project (0704-0188) Washington, DC 20503.				
1. AGENCY USE ONLY (Leave blank)		2. REPORT DATE March 2015	3. REPORT TYPE AND DATES COVERED Master's Thesis	
4. TITLE AND SUBTITLE COMPOSITE CASE DEVELOPMENT FOR WEAPONS APPLICATIONS AND TESTING			5. FUNDING NUMBERS	
6. AUTHOR(S) Cassandra C. Mitchell				
7. PERFORMING ORGANIZATION NAME(S) AND ADDRESS(ES) Naval Postgraduate School Monterey, CA 93943-5000			8. PERFORMING ORGANIZATION REPORT NUMBER	
9. SPONSORING /MONITORING AGENCY NAME(S) AND ADDRESS(ES) Lawrence Livermore National Laboratory			10. SPONSORING/MONITORING AGENCY REPORT NUMBER	
11. SUPPLEMENTARY NOTES The views expressed in this thesis are those of the author and do not reflect the official policy or position of the Department of Defense or the U.S. Government.				
12a. DISTRIBUTION / AVAILABILITY STATEMENT Approved for public release; distribution is unlimited			12b. DISTRIBUTION CODE	
13. ABSTRACT (maximum 200 words) Analysis of the dynamic response of cylindrical carbon fiber/epoxy cases containing high explosive fill was conducted using ALE3D finite element software. To develop an accurate model, material compression testing was performed with a Split Hopkinson Pressure Bar apparatus and Instron SATEC machine to verify high-strain rate and low-strain rate behavior, respectively. Resulting failure modes of compression test samples were similar to those found in current literature. Izod pendulum impact testing was performed to provide an intermediate strain rate comparison. An ANSYS model was developed to ensure fracture energy values obtained from Izod impact testing resulted in material stresses within the bounds of the high strain rate and low strain rate testing. The resulting material properties were input parameters for the ALE3D carbon fiber composite model developed by Kwon. The carbon fiber model and this thesis research provide critical information for testing and development in support of Lawrence Livermore National Laboratory's Agent Defeat Penetrator Project.				
14. SUBJECT TERMS Carbon fiber epoxy, carbon fiber composite, ALE3D, Split Hopkinson Pressure Bar, compression testing, Izod impact testing, Agent Defeat Penetrator			15. NUMBER OF PAGES 119	
			16. PRICE CODE	
17. SECURITY CLASSIFICATION OF REPORT Unclassified	18. SECURITY CLASSIFICATION OF THIS PAGE Unclassified	19. SECURITY CLASSIFICATION OF ABSTRACT Unclassified	20. LIMITATION OF ABSTRACT UU	

NSN 7540-01-280-5500

Standard Form 298 (Rev. 2-89)
Prescribed by ANSI Std. Z39-18

THIS PAGE INTENTIONALLY LEFT BLANK

Approved for public release; distribution is unlimited

**COMPOSITE CASE DEVELOPMENT FOR WEAPONS APPLICATIONS AND
TESTING**

Cassandra C. Mitchell
Lieutenant, United States Navy
B.S., Alfred University, 2007

Submitted in partial fulfillment of the
requirements for the degree of

MASTER OF SCIENCE IN MECHANICAL ENGINEERING

from the

**NAVAL POSTGRADUATE SCHOOL
March 2015**

Author: Cassandra C. Mitchell

Approved by: Young W. Kwon
Thesis Advisor

John D. Molitoris, Lawrence Livermore National Laboratory
Co-Advisor

Garth V. Hobson
Chair, Department of Mechanical & Aerospace Engineering

THIS PAGE INTENTIONALLY LEFT BLANK

ABSTRACT

Analysis of the dynamic response of cylindrical carbon fiber/epoxy cases containing high explosive fill was conducted using ALE3D finite element software. To develop an accurate model, material compression testing was performed with a Split Hopkinson Pressure Bar apparatus and Instron SATEC machine to verify high-strain rate and low-strain rate behavior, respectively. Resulting failure modes of compression test samples were similar to those found in current literature. Izod pendulum impact testing was performed to provide an intermediate strain rate comparison. An ANSYS model was developed to ensure fracture energy values obtained from Izod impact testing resulted in material stresses within the bounds of the high strain rate and low strain rate testing. The resulting material properties were input parameters for the ALE3D carbon fiber composite model developed by Kwon. The carbon fiber model and this thesis research provide critical information for testing and development in support of Lawrence Livermore National Laboratory's Agent Defeat Penetrator Project.

THIS PAGE INTENTIONALLY LEFT BLANK

TABLE OF CONTENTS

I.	INTRODUCTION.....	1
A.	BACKGROUND	1
B.	THESIS OBJECTIVE	5
C.	EXPERIMENTAL OVERVIEW	6
D.	LITERATURE REVIEW.....	9
II.	QUASI-STATIC AND DYNAMIC COMPRESSION TESTING	11
A.	QUASI-STATIC COMPRESSION TESTING BACKGROUND	11
B.	QUASI-STATIC COMPRESSION TESTING PROCEDURE.....	11
C.	INSTRON COMPRESSION TEST RESULTS.....	13
D.	DYNAMIC COMPRESSION TESTING BACKGROUND	17
E.	SHPB SAMPLE PREPARATION AND TESTING	18
F.	SHPB RESULTS.....	19
III.	IZOD EXPERIMENTAL IMPACT TESTING	27
A.	IZOD TESTING BACKGROUND	27
B.	IZOD TESTING PROCEDURE	28
C.	ACRYLIC IZOD IMPACT RESULTS.....	29
D.	KAFB CASE 1 IMPACT RESULTS	30
E.	LLNL CASE 2 IMPACT RESULTS	33
IV.	IZOD MODELING WITH ANSYS EXPLICIT DYNAMICS.....	35
A.	BACKGROUND	35
B.	PROBLEM SET-UP	35
C.	IZOD IMPACT MODEL RESULTS.....	37
V.	ALE3D HIGH-EXPLOSIVE FILLED CASE MODEL.....	41
A.	MODEL BACKGROUND	41
B.	IMPLEMENTATION OF THE CARBON FIBER MODEL.....	46
C.	COMPARISON OF STEEL CASE AND CFC CASE	48
D.	ALE3D MODEL CONCLUSIONS	69
VI.	CONCLUSIONS.....	71
A.	EXPERIMENTAL TESTING REMARKS.....	71
B.	ALE3D MODELING REMARKS	72
C.	RECOMMENDED FUTURE WORK.....	73
	APPENDIX A. CALCULATIONS FOR CONTROL SAMPLE (HY-80 STEEL) TO DETERMINE TEST MACHINE COMPLIANCE	75
	APPENDIX B. ADDITIONAL EXPERIMENTAL RESULTS	79
A.	LLNL CASE 2 “SCRAP” SAMPLE RESULTS.....	79
	APPENDIX C. ADDITIONAL ALE3D CODE.....	81
A.	CFC CODE AND NOTES.....	81
B.	CFC ALE3D INPUT CODE	85

LIST OF REFERENCES.....	95
INITIAL DISTRIBUTION LIST	99

LIST OF FIGURES

Figure 1.	Artist's concept of the Agent Defeat Penetrator, from [4].....	2
Figure 2.	Conceptual flexible agent defeat weapon designed with high-strength carbon fiber composite case, from [4].....	3
Figure 3.	Schematic of high-strength carbon fiber detonation test article utilized in support of the ADP project, from [4].	4
Figure 4.	Experimental testing at Lawrence Livermore National Laboratory Energetic Materials Center of acrylic (left) and carbon fiber composite (right) cases containing high explosive payload, from [4]. ...	5
Figure 5.	Samples extracted from the acrylic cylindrical case.	7
Figure 6.	Samples extracted from KAFB CFC case 1.	7
Figure 7.	Images demonstrating LLNL case 2 and typical dimensions of Carbon Fiber/Epoxy Cases wound at LLNL.	8
Figure 8.	KAFB CFC case data for three quasi-static compression test orientations.....	12
Figure 9.	LLNL case 2 data for three quasi-static compression test orientations.....	13
Figure 10.	Image of failed samples from KAFB case 1 subjected to radial, circumferential and axial compression orientations.	14
Figure 11.	Image of failed samples from LLNL case 2 subjected to radial, circumferential and axial compression orientations.	14
Figure 12.	Out-of-plane (radial) (left) and in-plane (circumferential) (right) quasi-static compression of Ma et al.'s woven fabric carbon fiber composite sample, after [6].	14
Figure 13.	Schematic of Split Hopkinson Pressure Bar apparatus, after [6].	18
Figure 14.	Raw Hopkinson data collected for carbon fiber LLNL case sample 2.	19
Figure 15.	SHPB stress-strain data for the acrylic samples subject to varying gas gun pressures.	20
Figure 16.	SHPB stress-strain data for the CFC samples subject to constant gas gun pressure of 50psi.	23
Figure 17.	Fractured sample (LLNL sample 2: circumferential orientation) depicting delamination and failure.	23
Figure 18.	Fractured sample (LLNL sample 1: radial orientation) depicting shear damage and failure.....	24
Figure 19.	Out-of-plane (radial) (left) and in-plane (circumferential) (right) high strain rate compression of Ma et al.'s woven fabric carbon fiber composite sample, after [6].	25
Figure 20.	Tinius Olsen low energy impact system for plastics, from [23].	28
Figure 21.	Photo of acrylic samples following impact. Half of sample 5 was lost due to the force of the strike.	30
Figure 22.	Image of KAFB case samples following impact testing.	31
Figure 23.	Image of LLNL case 2 samples following impact testing.	33

Figure 24.	ANSYS Explicit Dynamic refined mesh and support constraints for Izod pendulum impact problem. Plane of interest is outlined immediately above the supports.	36
Figure 25.	Von-Mises Stress along the plane of the Izod hammer impact for the Aluminum 6061 test specimen.	38
Figure 26.	Von Mises stress of CFC Izod sample subject to radial strike orientation (impact wedge not shown).	39
Figure 27.	Von Mises stress associated with the circumferential strike orientation of the CFC sample (impact wedge not shown).	39
Figure 28.	Quarter cylinder geometry (right) was utilized to cut computation time. Green center represents C4 explosive, red cylinder outer layer represents the steel shell. Air (not shown) was meshed around the cylinder as represented by the schematic (left).	42
Figure 29.	VisIt images depicting expansion of HE and damage progression of steel case with failure model at a time of: A. 1 μ sec, B. 10 μ sec, C. 20 μ sec and D. 30 μ sec. A damage value of 1.0 is considered a failed element.	45
Figure 30.	Image of the steel case and mesh with equivalent mass as the CFC case. The case thickness for the “thin” steel case was 0.07cm (0.026”).	46
Figure 31.	The unit cell composed of eight subcells utilized in Kwon and Park’s micromechanics model, from [27].	47
Figure 32.	Image depicting the mesh used for CFC case analysis containing 5520 elements and 6648 nodes.	49
Figure 33.	Graph illustrating the radial expansion of the CFC case at five axial locations measured from the base of the case along the carbon fiber shell. The locations are measured at the midpoint of the case thickness.	50
Figure 34.	Graph illustrating the radial expansion of the steel cases at five different axial locations along the shell. (Left) Cases contain no failure model. (Right) Cases contain failure model. (Top) Cases are mass-equivalent to the CFC case. (Bottom) Cases have equivalent thickness as the CFC case.	51
Figure 35.	Graph of Von Mises stress within the CFC case at six axial locations along the case.	52
Figure 36.	Comparison of steel case Von Mises stresses, without fracture models (left) and with fracture models (right). The color legend is the same for each case.	54
Figure 37.	Initial CFC case quarter geometry and mesh. The HE fill interior is hidden.	56
Figure 38.	CFC at a time of 10 microseconds after detonation. Thinning of the case is observed near the top of the case.	56
Figure 39.	CFC at a time of 14 microsecond following detonation. Case thinning and erosion of elements is observed.	57

Figure 40.	CFC case at a time of 20 microseconds following detonation. Significant case failure and erosion of CFC elements are observed. .	57
Figure 41.	Hoop (circumferential) stress of the CFC case at varying axial locations.	58
Figure 42.	Pressure at the detonation location for each model analyzed. The detonation pressure was identical for both thin steel cases and very similar for the CFC and thick steel cases.	59
Figure 43.	Hoop stress of steel cases at varying axial locations.....	61
Figure 44.	HE pressure within the CFC case at a time of 1 microsecond.....	62
Figure 45.	HE pressure within the CFC case at a time of 5 microseconds.....	63
Figure 46.	HE pressure within the CFC case at a time of 10 microseconds.....	63
Figure 47.	HE pressure within the CFC case at a time of 15 microseconds.....	64
Figure 48.	HE pressure within the CFC case at a time of 20 microseconds.....	64
Figure 49.	Unit cell level fiber stress averaged for all unit cells along the 15 cm axial location for each layer.	66
Figure 50.	Unit cell level fiber stress averaged for all unit cells along the 10 cm axial location for each layer.	67
Figure 51.	Unit cell level fiber stress averaged for all unit cells along the 5 cm axial location for each layer.	68
Figure 52.	Hydra radiographic time sequence of carbon fiber composite case containing high explosive payload, from [4].	70
Figure 53.	Plot of compression stress-strain data as-received from SATEC test. This data includes test machine compliance and requires “toe compensation.”	75
Figure 54.	Determination of equivalent young’s modulus from linear elastic region of raw data. The trend line is utilized to provide toe compensation.	76
Figure 55.	Graph showing corrected data as compared to raw data. Note the non-linear region at the “toe” of the graph due to slack in the machine and alignment of the specimen. To achieve the correct yield strength, this artifact must be compensated for and a new “zero point” established [15].	76
Figure 56.	Graph illustrated Raw Data (blue dashed line), corrected elastic region (red dot-dashed line) and final, shifted data (black dotted line) for a carbon fiber composite sample.	77
Figure 58.	Image of LLNL case 2 “Scrap” samples following impact testing. Similar to actual samples, Scrap samples 1 through 4 show similar failure as case 2 samples 1 through 3. Scrap samples 1 through 4 were struck radially and demonstrated significant delamination between carbon fiber winding layers. Samples 5 through 7 closely resemble actual case 2 samples 4 and 5. These were struck circumferentially and exhibited fiber breakage. Scrap sample 6 was mechanically separated by hand to better examine fiber.....	79
Figure 59.	Image of LLNL case 2 “Scrap” samples following impact testing.	80

Figure 60.	Internal (C4) pressure distribution for the thin steel case with no failure model at a time of approximately 5 microseconds.	81
Figure 61.	Internal (C4) pressure distribution for the thin steel case with failure model at a time of approximately 5 microseconds.	82
Figure 62.	Internal (C4) pressure distribution for the thick steel case with failure model at a time of approximately 5 microseconds.	83
Figure 63.	Internal (C4) pressure distribution for the thick steel case with no failure model at a time of approximately 5 microseconds.	84

LIST OF TABLES

Table 1.	Summary of compression test results. Significant plastic deformation was observed in the acrylic samples.	16
Table 2.	Split Hopkinson Pressure Bar Results.....	21
Table 3.	Summary of Izod test acrylic and KAFB case 1 samples.	32
Table 4.	Summary of Izod test sample results for LLNL CFC case.	34
Table 5.	Summary of the five different model input parameters and results.....	55
Table 6.	Summary of maximum and average hoop stress results.....	60
Table 7.	Maximum and average pressures exerted on the interior case wall by the C4.	61
Table 8.	Comparison of Elastic Modulus between the experimentally determined LLNL results and Kwon's Model.	70
Table 9.	Summary of failure modes of carbon fiber cases for various experimental tests.	72
Table 10.	Summary of IZOD test results for set of LLNL case 2 "scrap" samples. Even though geometry does not match Izod ASTM standards, the standard deviation among fracture energy results is small.	80

THIS PAGE INTENTIONALLY LEFT BLANK

LIST OF ACRONYMS AND ABBREVIATIONS

ADW	Agent Defeat Weapon
ALE3D	Arbitrary Lagrange/Eulerian 2D and 3D code
CFC	carbon fiber composite
DTRA	Defense Threat Reduction Agency
EMC	Energetic Materials Center
HE	high explosive
LLNL	Lawrence Livermore National Lab
NPS	Naval Postgraduate School
SHPB	Split-Hopkinson Pressure Bar
TDC	Top Dead Center

THIS PAGE INTENTIONALLY LEFT BLANK

ACKNOWLEDGMENTS

I would like to thank my advisor, Professor Young W. Kwon, for contributing his guidance and extensive experience with composites and structures to this thesis. I appreciate his ability to analyze problems in the most fundamental way possible and will continue to strive to do the same. Additionally, thanks to my co-advisor, Dr. John Molitoris, for contributing the interesting topic and providing insight and direction on this project. I owe a very sincere thank you to Dr. Andy Anderson and Dr. Al Nichols for their assistance with coding and explanations of ALE3D throughout this project. Also, I would like to thank Professor Jake Didoszak, who donated a significant amount of his valuable time and advice. Finally, I would like to acknowledge the Lawrence Livermore National Laboratory National Security Office for its support of our collaboration and the AMEA Initiative that made this work possible.

Most of all, I need to thank my husband, Phil, for his constant support and ability to help me keep things in perspective.

THIS PAGE INTENTIONALLY LEFT BLANK

I. INTRODUCTION

A. BACKGROUND

In October of 1998, the U.S. Department of Defense established the Defense Threat Reduction Agency (DTRA) as the official Combat Support Agency for countering chemical, biological, radiological and nuclear weapons that pose a threat to U.S. security [1]. Since the inception of DTRA, specialized Agent Defeat Weapons (ADW) have been developed to attack enemy chemical and biological agent manufacturing and storage facilities to neutralize the agent without spreading it. Current ADW include the CBU-107 Passive Attack Weapon (PAW) and the BLU-119/B CrashPAD. These weapons generally consist of a standard weapons case (such as the MK-84 for the CrashPAD device) and a high-temperature incendiary filler or payload. The warhead containment system is designed to penetrate the target, disperse and ignite the high temperature incendiary fill, which destroys the target agents via thermal, chemical or biocidal techniques. Incendiary air delivery agent defeat weapon systems rely primarily on thermal kill and continue to be developed as a means of destroying chemical and biological weapons while minimizing effects on civilians by preventing agent dispersion.

ADW payloads are unique in that they are required to produce high-temperature reactions for a long duration with low overpressure [2]. This combination provides optimal conditions to neutralize a biological or chemical agent, while the low overpressure prevents spreading the agent. These are the primary properties for prompt agent defeat. Challenges exist in designing the delivery system and payload to effectively destroy a variety of enemy agents, to include viruses, toxins and chemical agents [2]. Additionally, these agents may be stored in any number of containment devices or housed in a variety of structures: above ground, buried below ground, in a facility with doors, windows, dividing walls, etc. Ideally, a single ADW would be able to destroy a variety of

agents located in any number of storage configurations in order to limit the cost and operational burden of carrying multiple types of ADW [3].

Lawrence Livermore National Laboratory (LLNL) is currently working on techniques and development of ADW at the Energetic Materials Center (EMC). LLNL has been conducting energetic materials research for decades in an effort to fully understand the physics and chemistry involved with detonation of high explosives (HE) under various environmental conditions. With high-power computer simulation codes such as ALE3D, theoretical models of HE are developed and analyzed to predict the behavior of an ADW prior to experimental analysis. The LLNL EMC, in collaboration with DTRA is developing an Agent Defeat Penetrator. As observed in Figure 1 [4], the Agent Defeat Penetrator (ADP) Project utilizes a BLU-109 case for its penetration capabilities with proprietary filler material developed by LLNL/DTRA. High-explosive is used to disperse and ignite the payload.

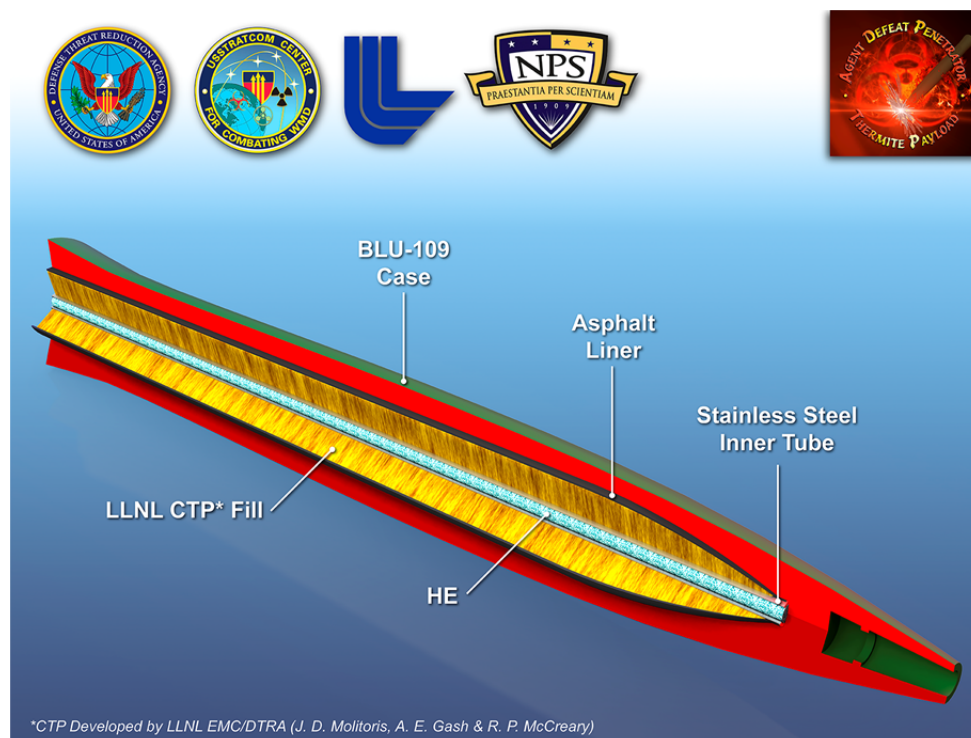


Figure 1. Artist's concept of the Agent Defeat Penetrator, from [4].

Current development of the ADP includes fabrication and analysis of a high strength carbon fiber composite (CFC) case for critical intermediate testing. High strength composites are important to this development as they simulate the final weapons case in dynamic experiments without the creation of high velocity fragments. Furthermore, composite cases could prove important to weapons other than the ADP where a more flexible multi-use device is required. Such a device concept is illustrated below in Figure 2 [4] where a fragmenting liner could be used to liberate agent for subsequent combustion.

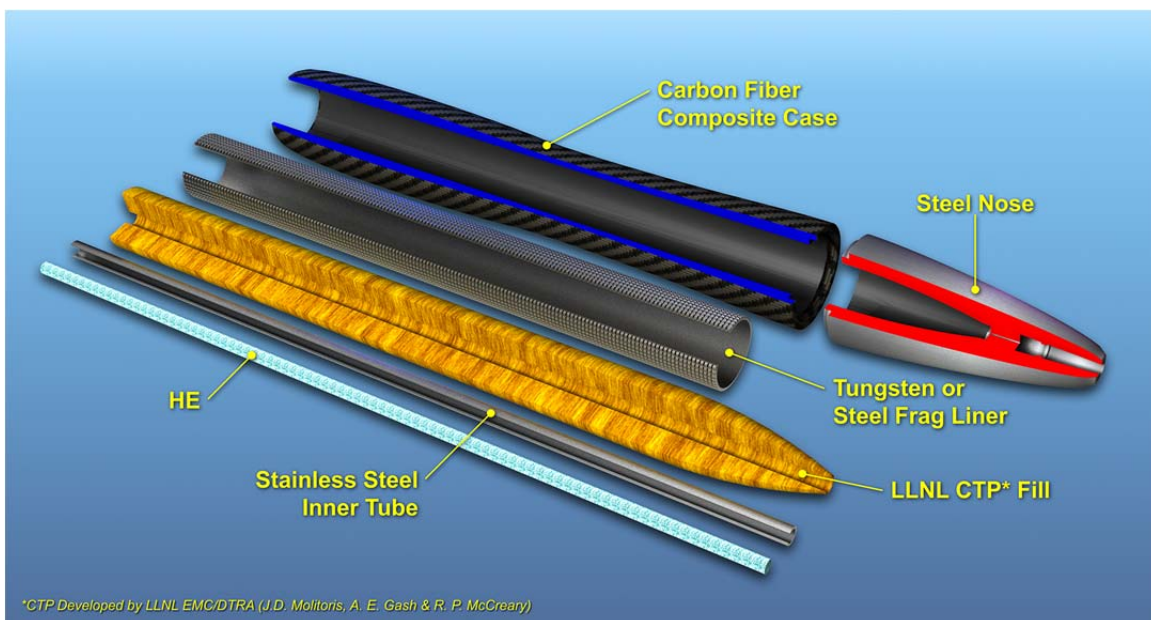


Figure 2. Conceptual flexible agent defeat weapon designed with high-strength carbon fiber composite case, from [4].

Composites such as carbon fiber/epoxy are manufactured to create a superior material or structure that takes advantage of the properties of its constituents. Several advantages exist for using carbon fiber as opposed to traditional aluminum or steel alloys. First, a higher strength-to-weight ratio is achievable with a CFC. Second, a greater containment time for the HE fill can be achieved, which is required to allow for adequate burn and compression of the payload. Third, carbon fiber properties can be manipulated with only small

adjustments to the current fabrication process. Changing parameters such as the winding angle or volume fraction of fiber will change the final composite's strength characteristics.

In support of the development of numerous ADWs such as the ADP, energetic tests have been conducted at LLNL EMC on aluminum, acrylic and CFC cylindrical cases containing a HE payload, similar to the set-up observed in Figures 3 and 4 [4]. Detonation of high explosive occurs at top dead center of the cylindrical cases. These tests allow for comparison of parameters such as the case containment time and payload compression ratio with respect to the material's strength and other dynamic properties. Although energetic tests provide valuable information, the cost associated with performing these experimental studies is substantial. The investment required to build and test models highlights the necessity of a reliable computational model that accurately predicts the containment time and failure response of the test specimen prior to experimental testing.

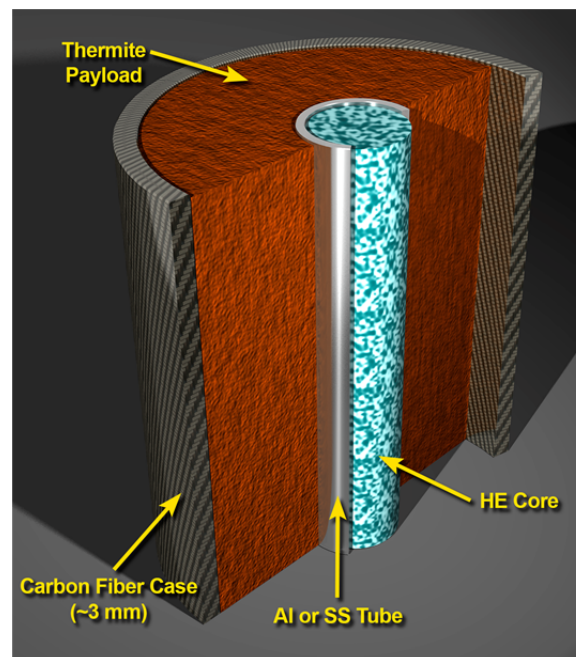


Figure 3. Schematic of high-strength carbon fiber detonation test article utilized in support of the ADP project, from [4].

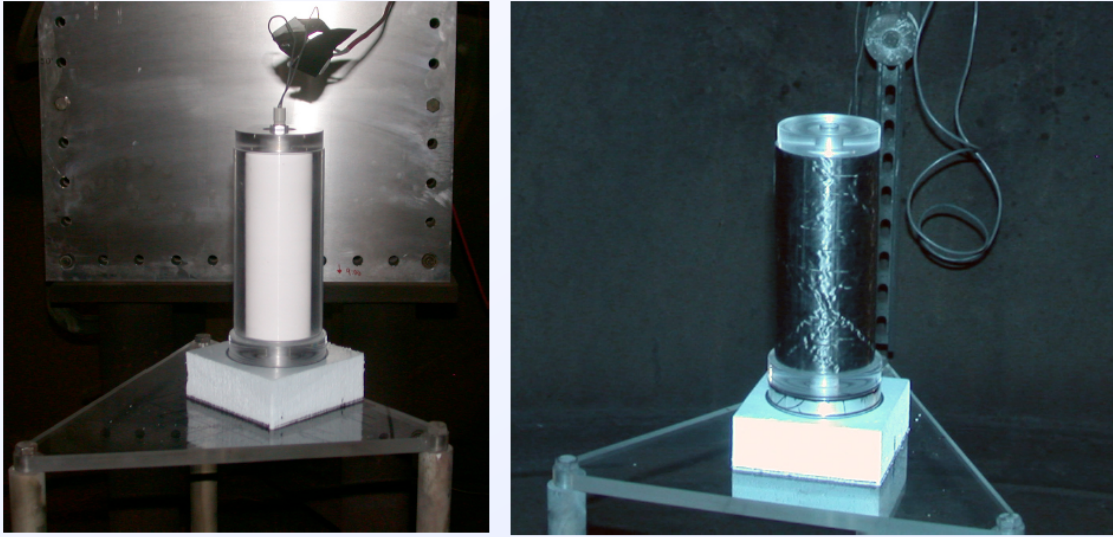


Figure 4. Experimental testing at Lawrence Livermore National Laboratory Energetic Materials Center of acrylic (left) and carbon fiber composite (right) cases containing high explosive payload, from [4].

Accurate computer simulations for these test articles could lead to an improved weapons case; giving us the ability to couple the advantages associated with high-strength carbon fiber composite cases with the LLNL thermitic CTP fill. Hence, allowing for fabrication of a flexible agent defeat device unlike any current ADW. This light-weight device would achieve the primary ADW goal of neutralizing a variety of threatening agents in a wide arrangement of potential storage facilities and environments with minimal agent dispersion.

B. THESIS OBJECTIVE

This thesis is in support of LLNL EMC's ongoing ADW research and will ultimately be used in the development of the Agent Defeat Penetrator Project. The primary thesis objective was to develop a model utilizing LLNL's Arbitrary Lagrange/Eulerian 2D and 3D code (ALE3D) to analyze the dynamic and failure responses of cylindrical cases subjected to high explosive (HE) payloads. Different case materials and configurations were analyzed to determine comparative strength and time to failure. Ultimately, the code will be used to

adjust and analyze the properties of CFCs to achieve the optimal case performance for the desired application.

Additionally, samples of acrylic and CFC cases were supplied by LLNL, and material properties were determined from several laboratory experiments. Performance of the case samples under various loading conditions was analyzed in order to obtain the most accurate model possible. The results of the ALE3D code were compared to experimental results of cases with HE payloads detonated at LLNL.

C. EXPERIMENTAL OVERVIEW

Three sample cases were received from LLNL for testing at NPS mechanical labs. The first case was an acrylic sample fabricated by PolyOne in July of 2014, similar to those tested at EMC in Figure 4 (left). Figure 5 illustrates the acrylic case and extracted samples. The second case was a CFC case with epoxy resin matrix manufactured by the carbon fiber winding facility at Kirtland Air Force Base for LLNL EMC in 2007. As shown in Figure 6, this case is will be referred to as the KAFB case 1. The last case was a CFC manufactured by the carbon fiber winding facility at LLNL. This CFC is referred to throughout this thesis as LLNL case 2, as shown in Figure 7.

Unfortunately, little is known about the manufacturing of KAFB case 1, since the carbon fiber winding facility at KAFB did not keep records dating back to 2007. The LLNL case 2 was manufactured with known carbon fiber and resin type and a well-documented process. This CFC was wound with 12 repeating layers of fiber orientations measured from the axial direction as 10°, 45°, 10° and 80°. It was cured with a 7 hour ramp to 300°F and a soak for 6 hours. The measurements of the final product are displayed in Figure 7.



Figure 5. Samples extracted from the acrylic cylindrical case.



Figure 6. Samples extracted from KAFB CFC case 1.

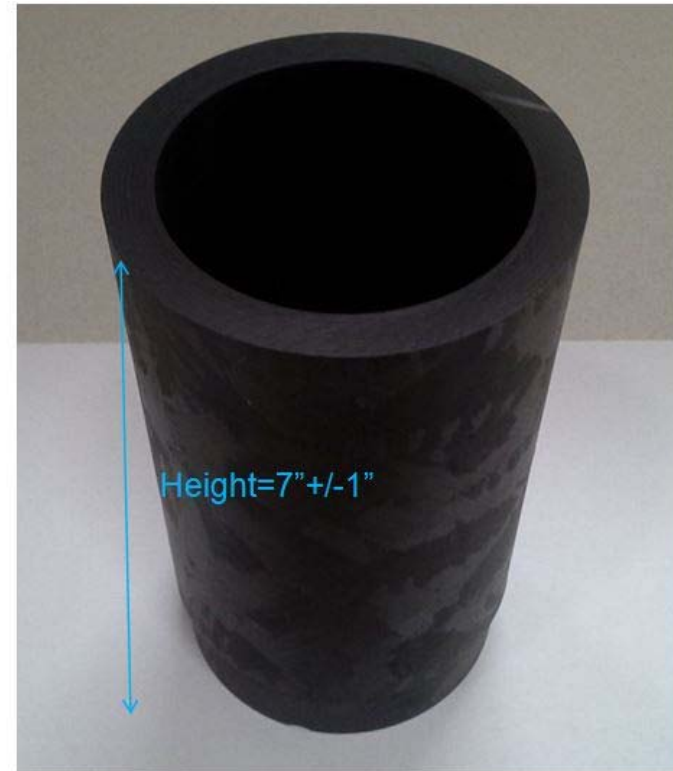
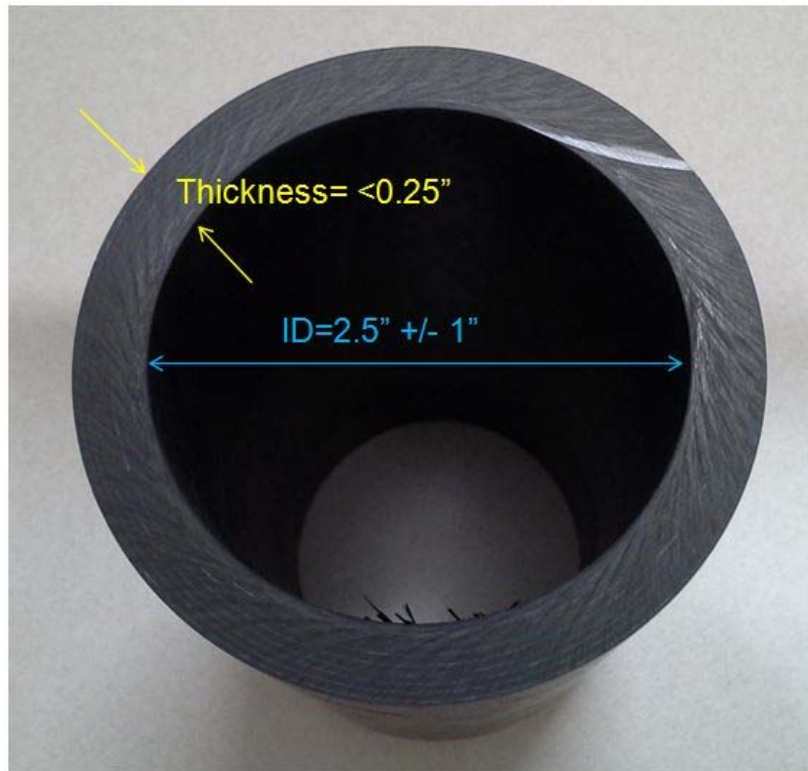


Figure 7. Images demonstrating LLNL case 2 and typical dimensions of Carbon Fiber/Epoxy Cases wound at LLNL.

Each of these cases were sectioned into cubes with edge lengths of approximately 6.95mm (0.27") for high strain rate testing on the Split Hopkinson Pressure Bar and quasi-static compression testing utilizing the Instron SATEC. Samples with approximate dimensions of 6.95mm by 6.95mm by 64.4mm (0.27" by 0.27" by 2.5") were extracted from the cylindrical cases for Izod pendulum impact testing.

A comparison of dynamic yield strength and quasi-static yield strength was needed for implementation into the ALE3D model. For this reason, high strain-rate testing was performed on the Split Hopkinson Pressure Bar and low strain-rate compression testing was done on the SATEC. Izod impact testing was performed to determine failure energy of the samples subject to different hammer strike orientations. An ANSYS Izod impact model was developed with bulk CFC material properties applied to ensure that the yield strength associated with the pendulum impact failure fell within the bounds of the quasi-static and dynamic failure stresses.

D. LITERATURE REVIEW

There is a significant amount of current literature that has performed both quasi-static [5] and dynamic testing on carbon fiber composites [6], [7]. However, CFC properties vary significantly with epoxy type, fiber type, manufacturing procedure and curing process. Because of the wide variety of CFC properties currently being researched, it is difficult to accurately compare the KAFB and LLNL CFC sample properties to values found in current literature. Carbon fiber epoxy properties from other research used in this thesis work are generally used as verification that the values obtained from NPS experiments are reasonable.

Research conducted by Ma et al. [6]. exposed woven carbon fiber samples of similar dimensions to both quasi-static compression and dynamic compression tests. The failure modes observed by Ma et al. are compared to the modes seen with the KAFB and LLNL CFC in this work.

Additionally, many carbon-fiber computer simulations and models exist for both cylindrical specimens under load [8] and impact tests [9], [10], [11]. Most of these research topics involve quasi-static models; the dynamic response of carbon fiber composites “has not been studied to a great extent” [12]. One study by Alexander et al. [12] modeled the dynamic response of unidirectional carbon fiber-epoxy plates when subjected to high-speed impact. This study, however, differs from the current thesis in that the carbon fiber was unidirectional, impact was achieved with a compressed gas gun and the resulting shock wave was measured utilizing a velocity interferometer system for any reflector probe. Their micromechanical modeling of the CFC did not include a fracture model. Currently, no published findings on carbon fiber models with HE cores are available.

II. QUASI-STATIC AND DYNAMIC COMPRESSION TESTING

A. QUASI-STATIC COMPRESSION TESTING BACKGROUND

Compression testing was performed to obtain stress-strain curves, as well as the corresponding yield strength and modulus of elasticity, for the samples under quasi-static loading. Due to the anisotropic nature of the CFC samples, testing was performed in the longitudinal, radial and circumferential directions for each case. The purpose of this testing was to achieve a lower bound for the material properties to implement into the carbon fiber composite ALE3D model. Since the number of samples was limited for each case, each orientation of interest was only tested once.

B. QUASI-STATIC COMPRESSION TESTING PROCEDURE

SATEC Instron Materials Testing machine (Model MII-20UD) was used with a hemispherical bearing plate to perform compression tests on carbon fiber composite cube samples with an approximate dimension of 6.85mm (0.27") per side. A compression rate of 2 to 3mm/min was used for the samples and all were compressed until failure, as determined by delamination or fracture for the carbon fiber samples and a marked drop in stress.

Accurately measuring the test machine compliance was a concern, as slack in the system set-up could lead to incorrect modulus readings for the samples. Test machine compliance is set-up dependent, so prior to testing the carbon fiber, a sample of HY-80 steel with a known elastic modulus was tested as a control. The validity of this approach has been verified by [13] and [14]. More accurate modulus measurements could be achieved with strain gauges or another type of extensometer; however, the available carbon fiber samples received from LLNL were too small to adhere a strain gauge to. Young's modulus for each sample was determined utilizing the procedure described in [13] and detailed in Appendix A.

Toe compensation was required, per reference [15], in order to obtain the correct zero starting point for the stress-strain curves. Figures 8 and 9 compare corrected stress-strain data for each case in three compression orientations. Additionally, the area under each stress-strain curve up to the point of fracture was calculated from the corrected data. This area under the stress-strain curve is known as the specimen toughness [16], and is sometimes referred to as the strain energy density. The toughness represents the energy absorbed by the material up to fracture. Table 1 summarizes the toughness of each sample calculated using the trapezoid rule between consecutive stress (σ) and strain (ϵ) points and summed along the entire area:

$$Area_{1-2} = (\epsilon_2 - \epsilon_1) \left(\frac{\sigma_2 + \sigma_1}{2} \right) \quad (1.1)$$

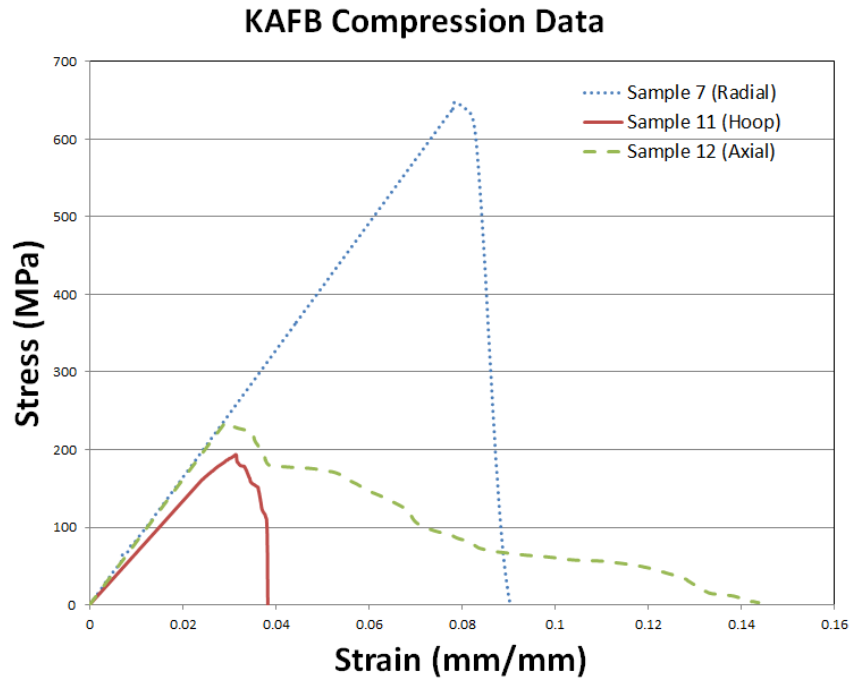


Figure 8. KAFB CFC case data for three quasi-static compression test orientations.

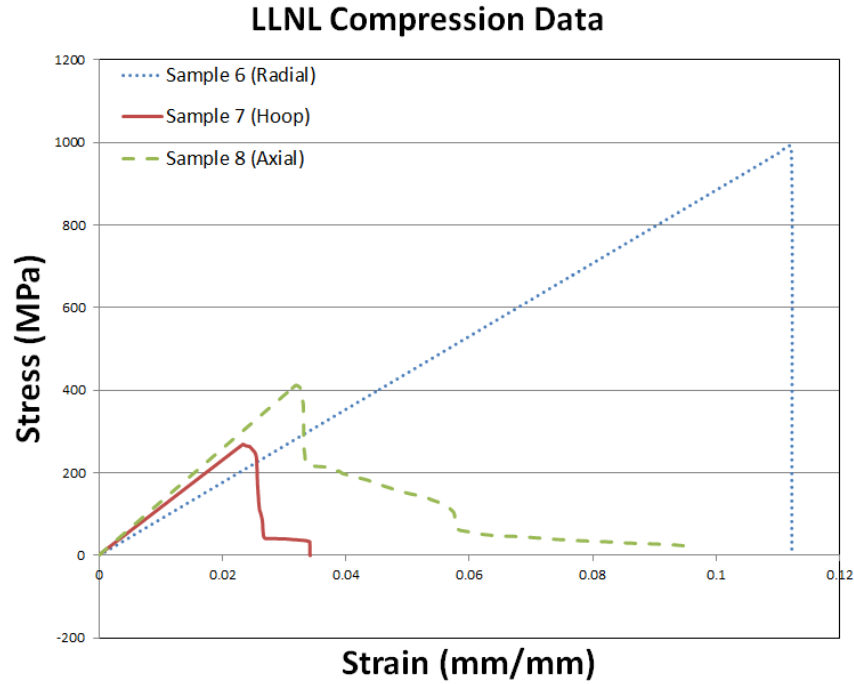


Figure 9. LLNL case 2 data for three quasi-static compression test orientations.

C. INSTRON COMPRESSION TEST RESULTS

As observed in Figures 10 and 11, the failures exhibited by the CFC samples based on compressive load orientations listed in Table 1 are relatively consistent between the two cases. Shear damage and fracture occurred in the radial compression orientation for both cases, as illustrated by KAFB case 1 sample 7 and LLNL case 2 sample 6. Significant delamination of the samples is apparent in the circumferential compression orientation for both cases (KAFB case 1 sample 11 and LLNL case 2 sample 7). Delamination is observed, to a slightly lesser extent, in the axial orientation (KAFB case 1 sample 12 and LLNL case 2 sample 8). These failure types are consistent with Ma et al.'s findings with woven carbon fiber epoxy composites as illustrated in Figure 12 [6]. In Figure 12, Ma et al.'s left image is consistent with LLNL and KAFB radial compression orientation, and illustrates shear deformation and fiber breakage. The right image shows delamination failure, similar to circumferential compression orientations in LLNL and KAFB cases.

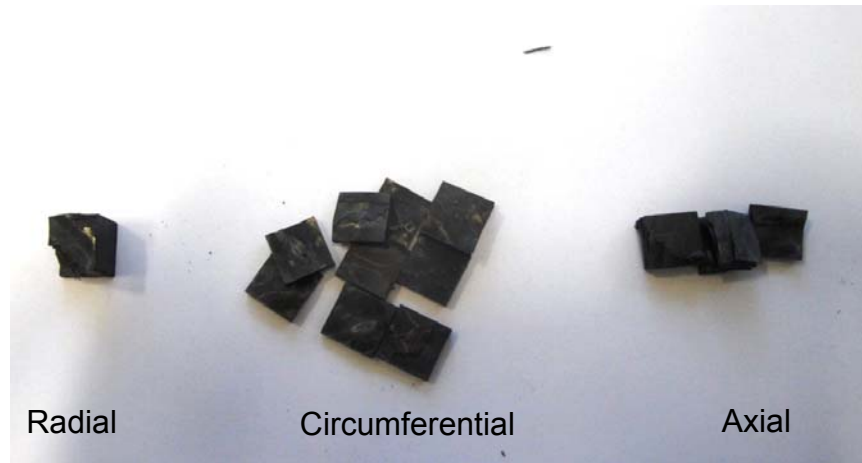


Figure 10. Image of failed samples from KAFB case 1 subjected to radial, circumferential and axial compression orientations.



Figure 11. Image of failed samples from LLNL case 2 subjected to radial, circumferential and axial compression orientations.

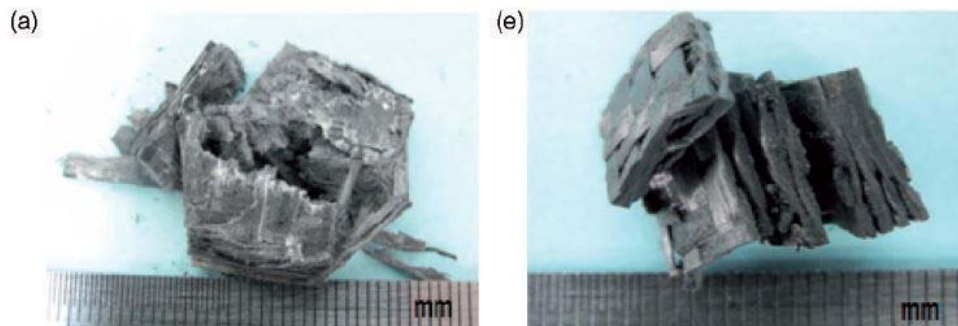


Figure 12. Out-of-plane (radial) (left) and in-plane (circumferential) (right) quasi-static compression of Ma et al.'s woven fabric carbon fiber composite sample, after [6].

Table 1 summarizes the maximum compressive strength, toughness and calculated elastic modulus for each sample. LLNL case 2 exhibits greater compressive strength and toughness than KAFB case 1, which is likely due to differences in fiber orientation, but aging of the first case may also cause decreased strength. Despite the higher overall strength of the second case, both cases display greater strength in the radial orientation than in the axial or circumferential directions. The fibers are the load carrying component of the composite, so the CFC is expected to be strongest when the load is applied parallel to the fiber orientation. It is expected that the circumferential orientation be the weakest, since few of the load-carrying fibers are oriented to carry load in this direction. Instead, more layers have fibers oriented axially and force exerted in the circumferential direction leads to rapid delamination.

Additionally, for the LLNL composite, the interfaces between the composite layers formed when the filament winding manufacturing process changed winding orientations were one of the weaker points in the composite. While the axial and circumferentially loaded orientations applied stress parallel to the weak interfaces and caused delamination failure, the radial orientation applied stress perpendicular and resulted in greater yield strength. Although mechanical properties of carbon fiber composites can vary greatly with curing agent and regime [17], as well as fiber orientation and volume fraction of fiber in the matrix [18], similar composites studied in published data [17] exhibit elastic moduli that agree with the findings in Table 1.

Table 1. Summary of compression test results.
Significant plastic deformation was observed in the acrylic samples.

Sample	Orientation	Young's Modulus (GPa)	Max Compressive Stress (MPa)	Toughness (kJ/m ³)
HY-80 Control	Axial	213.8	761.99	
Case 1 Sample 7	Radial	11.2	647.04	256.7
Case1 Sample 11	Circumferential	8.457	193.65	43.1
Case 1 Sample 12	Axial	10.852	234.899	163.8
Case 2 sample 6	Radial	12.32	987.59	481.7
Case 2 sample 7	Circumferential	18.102	269.396	53.7
Case 2 sample 8	Axial	21.9	412.31	133.1
Acrylic sample 4	Axial	5.13	547.08*	
Acrylic sample 5	Circumferential	5.23	686.72*	

D. DYNAMIC COMPRESSION TESTING BACKGROUND

Although the strain rate associated with a pendulum impact apparatus, such as the Izod or Charpy impact machines, is about 100s^{-1} [19], neither Charpy nor Izod impact tests produce a stress-strain curve. For the high strain rate testing required for explosive or ballistic impact experiments, the Split-Hopkinson Pressure Bar is the ideal apparatus to achieve strain rates ranging from 10^2 to 10^3 s^{-1} .

The Split Hopkinson Pressure Bar (SHPB) utilizes two long cylindrical bars, an incident bar and a transmitter bar, both made of high strength steel and approximately 3/4" in diameter. The specimen to be tested is sandwiched between the bars with a small amount of vacuum grease between the contact surfaces. Strain gages are mounted on the incident and transmitter bars, as shown in Figure 13. Aligned with the incident bar is the striker bar, which is accelerated by a gas gun and designed to impact the incident bar square on the end [20]. The velocity of the bar at the moment of impact is dependent on the pressure to which the gas is compressed, and is measured typically by a magnetic pickup [19]. This impact produces a compression pulse which travels down the incident bar. The pulse has a reflected component and a component transferred through the specimen and into the transmitter bar. The specimen between the incident and transmitter bars is compressed and plastic deformation occurs. The stress pulses are detected by the strain gages in real time, and from dynamic wave propagation theory a stress-strain curve for the failed material specimen can be extracted [20].

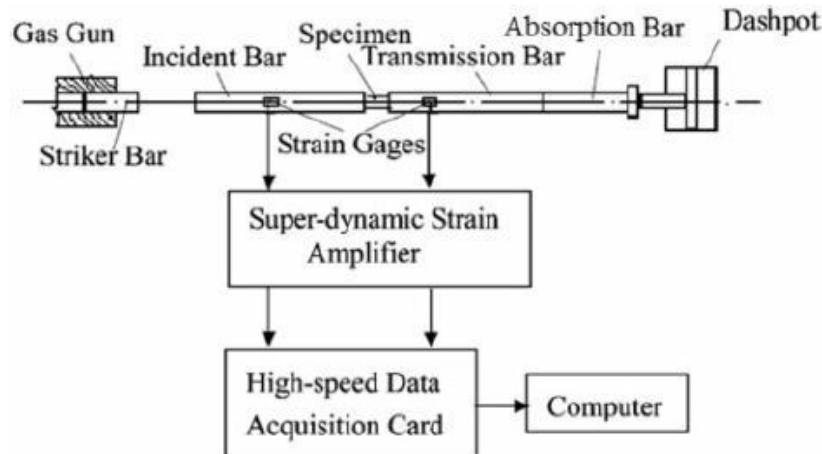


Figure 13. Schematic of Split Hopkinson Pressure Bar apparatus, after [6].

E. SHPB SAMPLE PREPARATION AND TESTING

Typically, SHPB specimens are cylindrical to avoid the possibility of corners receiving uneven load during the compression test. Because the samples received from LLNL were sectioned from a pre-existing case, the case was not thick enough to remove cylindrical samples. The samples received were cubes with approximate dimensions of 6.85mm (0.27") per side. The cube CFC samples were mounted onto a polishing disk with resin and hand polished so that the faces in contact with the incident bar and transmission bar were parallel to within 40–80 μ m. An equivalent diameter was calculated for each sample and the samples were tested in the SHPB apparatus as described above. Three acrylic samples were tested under varying gas gun pressures to determine the optimal pressure for the carbon fiber samples. The carbon fiber samples were consistently tested at the same pressure for ease of comparison. The resulting raw data from the data acquisition software is shown in Figure 14 for one of the samples.

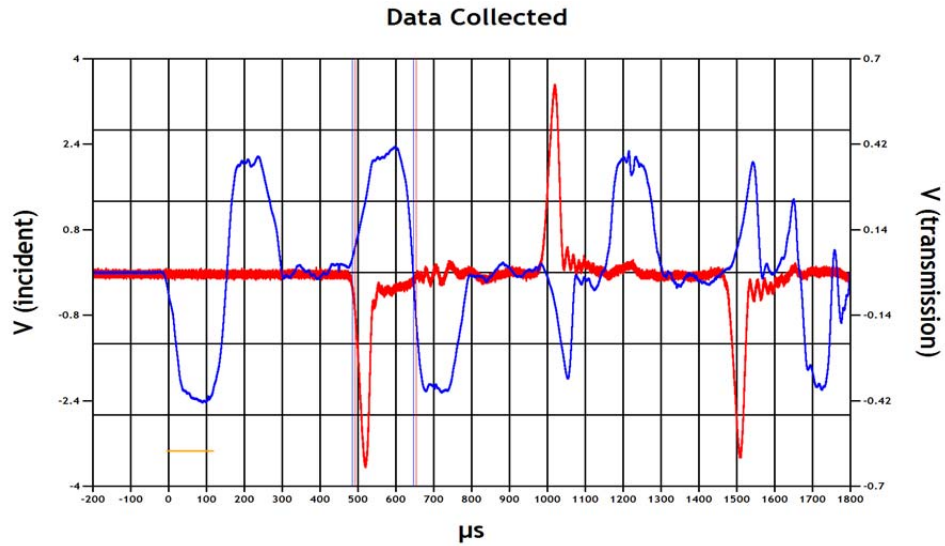


Figure 14. Raw Hopkinson data collected for carbon fiber LLNL case sample 2.

F. SHPB RESULTS

The three acrylic samples were compressed almost to powder following the SHPB testing, so no final image is available for these samples. The resulting stress strain curves for the acrylic samples are observed in Figure 15 and a summary of results is provided in Table 2. As anticipated, the stress-strain curves for the acrylic samples illustrate the dependence of the yield stress on strain rate. As the gas gun pressure was increased, the strain rate increased, and the corresponding maximum stress increased for the sample. Related to the increase in yield strength is an increase in the toughness, as Table 2 clearly illustrates. Toughness was calculated by Equation 1.1 as discussed previously in Section B.

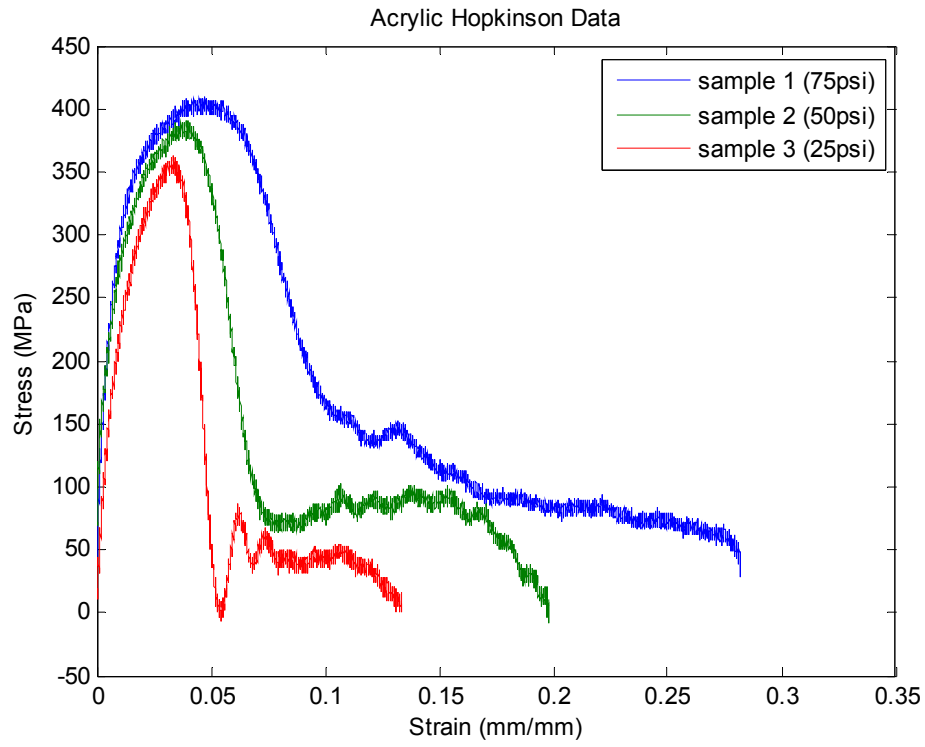


Figure 15. SHPB stress-strain data for the acrylic samples subject to varying gas gun pressures.

Table 2. Split Hopkinson Pressure Bar Results.

	Orientation	Gas Gun Pressure (psi)	Avg Strain Rate of Shot	Avg Stress of linear Zone (MPa)	Slope of linear Zone (GPa)	Max Stress (MPa)	Toughness (kJ/m ³)
Acrylic Sample 1	Circumferential	75	2043.6	157.64	218.9	410.4	455.6
Acrylic Sample 2	Circumferential	50	1382.2	166.25	198.8	391.1	291.9
Acrylic Sample 3	Radial	25	726.4	36.88	101.8	363.6	154.2
KAFB Sample 1	Circumferential	50	1317.3	160.4	233.6	411.5	143.8
KAFB Sample 2	Circumferential	50	1334.2	35.43	184.6	408	92.96
LLNL Sample 1	Radial	50	721	573.15	159.7	911.7	538.5
LLNL Sample 2	Circumferential	50	1322.9	52.25	194.9	373.7	121.6

Due to the limited quantity of CFC samples available for SHPB testing, to accurately compare the composite data of the two cases with respect to varying orientations, the same gas gun pressure was used for each shot. If more CFC samples were available for testing, the same strain-rate dependence of the yield strength would be apparent as in the acrylic samples. However, for the purposes of this experiment, the yield strength of the various samples when exposed to the same strain rate was sufficient for the purpose at hand.

The KAFB case demonstrated consistent strain rate, yield strength and failure modes for the samples subjected to circumferential strike orientation. Two shots were performed in the circumferential orientation to ensure that the cube sample shape was not affecting the resulting data. The consistency of the data observed in Table 2 and in Figure 16 confirms no significant effect from the cube edges, so long as the cube sides are well-polished to ensure the contact faces are parallel. Figure 17 depicts the circumferentially oriented sample following failure.

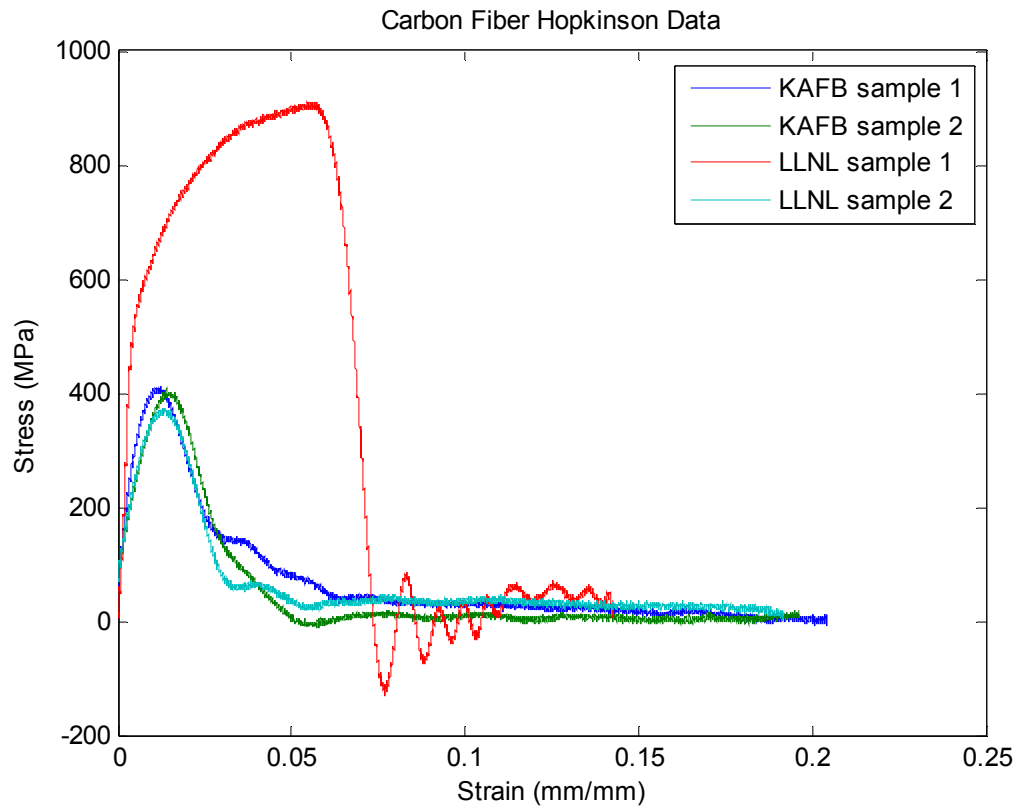


Figure 16. SHPB stress-strain data for the CFC samples subject to constant gas gun pressure of 50psi.



Figure 17. Fractured sample (LLNL sample 2: circumferential orientation) depicting delamination and failure.

As observed in Figure 17, the LLNL sample subjected to circumferential loading experienced failure from delamination of the composite layers. This failure mode is consistent with KAFB case samples loaded circumferentially. Additionally, delamination was the failure mode observed for the quasi-static compression testing. Samples oriented in this manner appeared to exhibit the same failure mode regardless of strain rate, and this orientation consistently achieved higher yield strength values for dynamic compression testing than the quasi-static compression testing for both sets of cases. The maximum yield strength for the circumferential orientation was almost twice the quasi-static values.

The LLNL sample 1 experienced a radial strike orientation. This orientation exhibited significantly higher yield strength and toughness values than the circumferential orientation, but the dynamic yield strength was surprisingly similar to the quasi-static yield strength observed during Instron compression testing. Furthermore, failure of this sample was due to shear damage, as observed in Figure 18, which is consistent with the quasi-static failure mode.



Figure 18. Fractured sample (LLNL sample 1: radial orientation) depicting shear damage and failure.

These findings are consistent with Ma et al.'s findings [6] with woven carbon fiber epoxy composites, as depicted in Figure 19. Ma reported that “fiber breakage and shear deformation occur at various strain rates and the main damage mode is shear failure” for out-of-plane loading, which is analogous to the radial loading of the LLNL CFC sample. He also annotated that the “composites are compressed almost into debris” as strain rate becomes large ($\sim 2000/s$). This is consistent with the failure mode experienced by LLNL sample 1, although strain rates for the LLNL samples were well below Ma et al.'s maximum observed strain rates. Similarly, delamination failure was seen for in-plane loading until strain rates become large (1400-1600/s) at which time the woven carbon fiber composites fail under both shear and delamination modes. For Figure 19, the left image illustrates shear deformation and fiber breakage occurring at a strain rate of 1600/s, while right image shows delamination failure at a strain rate of 1400/s. The in-plane orientation is similar to the circumferential compression orientation observed in Figure 17.

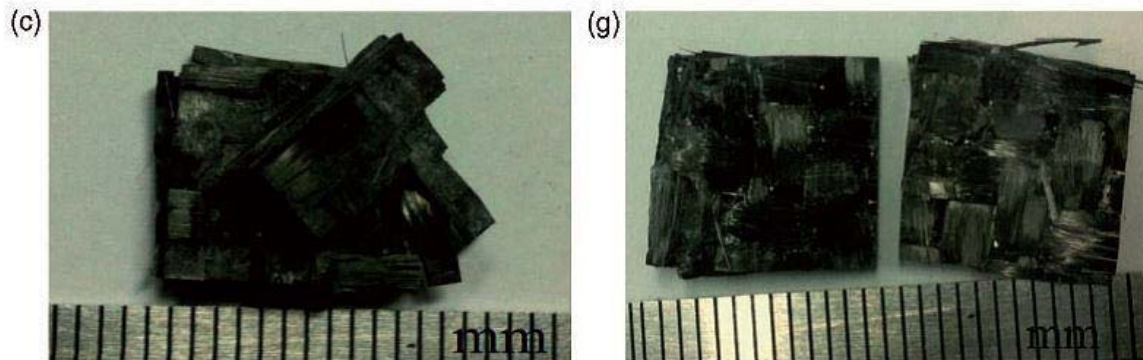


Figure 19. Out-of-plane (radial) (left) and in-plane (circumferential) (right) high strain rate compression of Ma et al.'s woven fabric carbon fiber composite sample, after [6].

THIS PAGE INTENTIONALLY LEFT BLANK

III. IZOD EXPERIMENTAL IMPACT TESTING

A. IZOD TESTING BACKGROUND

Izod low-energy impact testing is typically conducted on standard notched samples to determine the amount of energy required to deform and fracture the specimen. This impact energy (or impact resistance) is typically found by measuring the pendulum angles at the beginning of the pendulum swing and at the end of the pendulum swing, following impact with the test specimen. The energy lost by the pendulum during the impact is a result of the summation of the following energies [21]:

- Energy required to initiate the fracture
- Energy to indent or deform the specimen at the impact
- Energy required to propagate the fracture
- Energy required to overcome friction between the pendulum striker and the specimen
- Energy required to eject the fractured piece(s)
- Energy required to bend the specimen
- Energy required to produce vibration in the pendulum
- Energy required to produce vibration or movement in the test stand
- Energy to overcome bearing friction
- Energy required to overcome windage

Accurate results require the pendulum to completely fracture the specimen with one pendulum swing, so additional weight can be added to ensure failure of the sample occurs upon impact. Frictional loss in the bearings and windage loss (between the swinging pendulum and the air) is corrected for by calibrating the machine with a series of pendulum swings prior to testing a set of samples. The

pendulum is assumed to be rigid, so any possible radial play in the bearings is ignored [22].

The impact velocity of the pendulum can be solved for by relating the kinetic energy immediately prior to impact to the initial potential energy of the pendulum at its starting (latched) height:

$$\begin{aligned}\frac{1}{2}mv^2 &= mgh \\ v &= \sqrt{2gh}\end{aligned}\tag{1.2}$$

Windage and frictional losses are neglected in this calculation of velocity. For all samples tested, the latched height was 609.6mm (24 in).

B. IZOD TESTING PROCEDURE

Tinius Olsen model IT504 low energy impact tester (Figure 20) was used to test acrylic and CFC samples with approximate dimensions of 6.95mm by 6.95mm by 64.4mm (0.27" by 0.27" by 2.50").



Figure 20. Tinius Olsen low energy impact system for plastics, from [23].

An Olympus *i*-speed high speed camera was set up to ensure the samples did not move excessively during impact. Neither LLNL nor the NPS machine shop owned the equipment required to produce a consistent notch in the samples per the ASTM standard [21], so the testing was conducted with un-notched samples. The samples were oriented so that approximately half of the sample was secured in the sample holder, consistent with the geometry of a notched sample. The KAFB case 1 samples 5 and 6 were oriented so approximately 1/3 of the sample was contained in the holding vice to ensure bending of the samples was not occurring.

As illustrated in Table 3, the hammer was aligned with respect to the samples so that the pendulum strike occurred at the inner wall (radial ID) or outer wall (radial OD) for the acrylic samples. All carbon fiber samples were aligned so that the hammer strike occurred at the inner wall (radial ID) or along the circumferential (hoop) direction. Only five of the eight provided acrylic samples were tested, six of the eight KAFB case 1 and LLNL case 2 samples were tested. LLNL case 2 was delivered with several “scrap” samples, whose dimensions did not precisely match that of the IZOD standard. These scrap samples were tested to ensure correct operation of the high-speed camera and adequate sample fixturing prior to testing actual samples. For completeness, the dimensions and impact energy of these “scrap” samples is summarized in Appendix B.

C. ACRYLIC IZOD IMPACT RESULTS

The nominal pendulum weight used for testing of the acrylic samples was 12.46N (2.800 lbf). The acrylic test samples displayed consistent results for the specimen impact energy (table 3). Figure 21 illustrates the fracture surface for all five samples tested was consistent, exhibiting a flat, linear region from the propagating crack. All acrylic samples were considered a complete break, as defined in ASTM D256 [21]. High speed photography displayed minimal movement of the acrylic samples axially in the sample vice. Upon further investigation, some axial movement in the clamp is typical of acrylic samples subjected to impact

testing and should not adversely influence the resulting energy readings. Comparison of the acrylic data is consistent with published values.

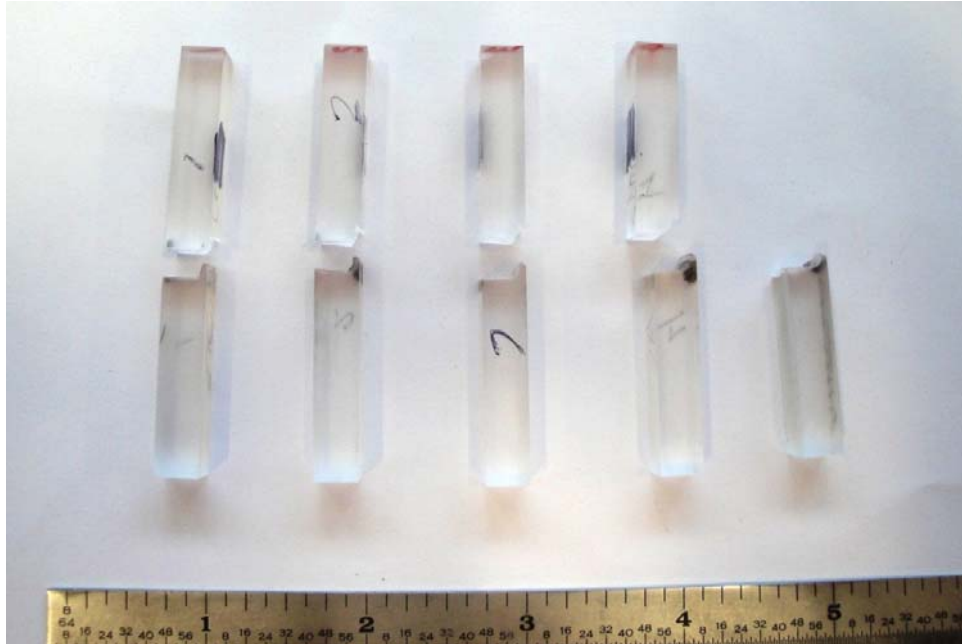


Figure 21. Photo of acrylic samples following impact. Half of sample 5 was lost due to the force of the strike.

D. KAFB CASE 1 IMPACT RESULTS

The CFC samples from KAFB case 1 produced less consistent results. The procedure for Izod testing of plastic specimen recommends using the lightest standard pendulum expected to break each sample with a loss of not more than 85% of its energy [21]. For the first CFC sample tested, the weight of the pendulum was insufficient to cause a failure, as shown in Figure 22. Sample 1 was classified as a non-break. A non-break, according to ASTM D 256, is one in which the fracture extends less than 90% the distance of the fracture line of the specimen.

For the second specimen, the weight of the impact hammer was increased to 41.14N (9.248lbf). The mounting of the mass on the Tinius Olsen test machine ensures that the equivalent mass of the pendulum is centered in the striking bit

[23]. The remaining samples exhibited partial or incomplete breaks in that the pendulum did not have the energy necessary to toss the broken piece(s), due to the toughness of the carbon fibers. These samples were still considered structurally failed, since they exhibited significant delamination or fiber breakage, and were easily mechanically separated by hand, as observed in Figure 22 sample 2. Prior to being mechanically separated, samples 2, 3 and 4 exhibited similar fractures. Samples 5 and 6 were oriented so that approximately 1/3 of the sample was contained in the holding vice to ensure bending of the samples was not occurring (the fracture energy values were approximately the same as the previous orientation). The reading on Sample 6 failed to register.

The three samples that were oriented for a circumferential failure produced consistent impact energy results. Only one reading of radial impact energy was obtained, due to initial set-up issues. Figure 22 illustrates the failed samples. Although the recommendation is for at least five, and preferably ten, samples are tested in each orientation to determine impact resistance; we were limited in the number of samples available for testing.



Figure 22. Image of KAFB case samples following impact testing.

An accurate comparison of the KAFB case results with published data is unlikely due to the amount of ambiguity surrounding the samples. As discussed previously, when the Kirtland Air Force Base carbon fiber winding facility was contacted for information on the manufacturing of the case the lab had no records dating back to 2007 of products manufactured. As a result, the resin composition, method of preparation and curing, carbon fiber type and orientation are unknown. Furthermore, CFCs are susceptible to material property degradation upon aging, depending on the composition. The KAFB case samples were in storage for years, so it is possible that aging of the composites could result in a change in fracture energy values.

Table 3. Summary of Izod test acrylic and KAFB case 1 samples.

	Sample Number	Orientation of Strike	Energy (J)	kJ/m ²	J/m
Acrylic Case	1	Radial ID	0.8110	16.937	117.201
	2	Radial ID	0.7802	15.971	110.521
	3	Radial OD	0.7056	14.736	101.975
	4	Radial OD	0.7117	14.864	102.858
	5	Radial ID	0.7151	15.108	103.940
	Avg Radial ID		0.7688	16.005	110.554
	STD Dev Radial ID		0.0490	0.9150	6.6306
	Avg Radial OD		0.7087	14.800	102.417
	STD Dev Radial OD		0.0043	0.0902	0.6244
	Average (total)		0.7447	15.5232	107.2990
	STD Dev (total)		0.0478	0.925	6.477
KAFB Case 1	1	Radial ID	Failed Test		
	2	Hoop	9.6191	209.577	1408.360
	3	Hoop	10.1420	183.992	1379.940
	4	Radial ID	8.2014	154.966	1134.350
	5	Hoop	10.1690	184.482	1355.950
	6	Radial ID	No reading		
	Avg Hoop		9.9767	192.6837	1381.4167
	STD Dev (hoop)		0.3100	14.6321	26.2362

E. LLNL CASE 2 IMPACT RESULTS

Although the ability to compare the LLNL case to the KAFB case is limited due to the ambiguity surrounding the KAFB case specification, it appears that the LLNL case is tougher in both directions (Figure 23). One overwhelming difference between the cases is the failure mode with respect to different strike orientations. As displayed in Figure 23, samples 1 through 3 were struck radially and demonstrated significant delamination between (what appears to be) carbon fiber winding layers. Samples 4 and 5 were struck circumferentially and exhibited fiber breakage.

While the KAFB case exhibited fiber breakage in every strike orientation, LLNL case samples clearly exhibit delamination when oriented in the radial direction. In the circumferential direction, fiber breakage was prevalent. The same results were illustrated in the “scrap” samples (Appendix B). Although these samples did not meet Izod ASTM standard dimensions, their failure modes were consistent and followed the trends of the Izod samples in Figure 23. The “scrap” samples are included in Appendix B for informational purposes.



Figure 23. Image of LLNL case 2 samples following impact testing.

Table 4. Summary of Izod test sample results for LLNL CFC case.

	Sample Number	Orientation of Strike	Dimensions W x D (mm)	Energy (J)	kJ/m^2	J/m
LLNL Case #2	1	Radial ID	6.93 x 6.95	6.4909	134.7680	936.6430
	2	Radial ID	6.94 x 6.94	9.2048	191.116	1326.350
	3	Radial ID	6.94x 6.95	10.7300	222.465	1546.130
	4	Hoop	6.94x6.95	5.5602	115.777	801.182
	5	Hoop	6.95 x 6.96	5.7569	119.015	828.344
	Avg Radial			8.8086	182.7830	1269.7077
	STDDev (Radial)			2.1471	44.4384	308.6663
	Avg Hoop			5.6586	117.3960	814.7630
	STDDev (Hoop)			0.1391	2.2896	19.2064

IV. IZOD MODELING WITH ANSYS EXPLICIT DYNAMICS

A. BACKGROUND

After performing both low strain rate quasi-static compression testing and high strain rate dynamic compression testing, it was desired to perform a moderate-strain rate test for comparison. Izod impact tests can achieve strain rates of about 100s^{-1} , although it is difficult to measure the strain rate produced from a pendulum impact test, and no stress strain curve results. For this reason, an Izod impact model was developed in ANSYS to model the resulting stresses immediately upon impact. The desired goal was to have a simplified Izod model with custom material properties that would produce stresses that were bound by the previous compression tests. The resulting information could then be used as a bound for the ALE3D composite model.

B. PROBLEM SET-UP

The Izod test specimen and impact hammer were modeled in SolidWorks utilizing the standard dimensions found in ASTM D256 [21] with the exception of the notch and loaded into ANSYS. For simplicity, only the wedge was modeled in place of the entire impact pendulum assembly, as observed in Figure 24. Initial mesh and time steps were chosen based on Lee's explicit dynamics example of a bullet impacting a plate [24]. The problem was initially run in the explicit dynamics suite of ANSYS with a stainless steel Izod impact wedge and an aluminum Izod sample. Fixed supports were applied to the faces of the Izod model where the clamp grips the specimen on the Tinius Olson test machine. The final Izod impact specimen had a mesh refinement consisting of 21,116 elements and 4286 nodes.

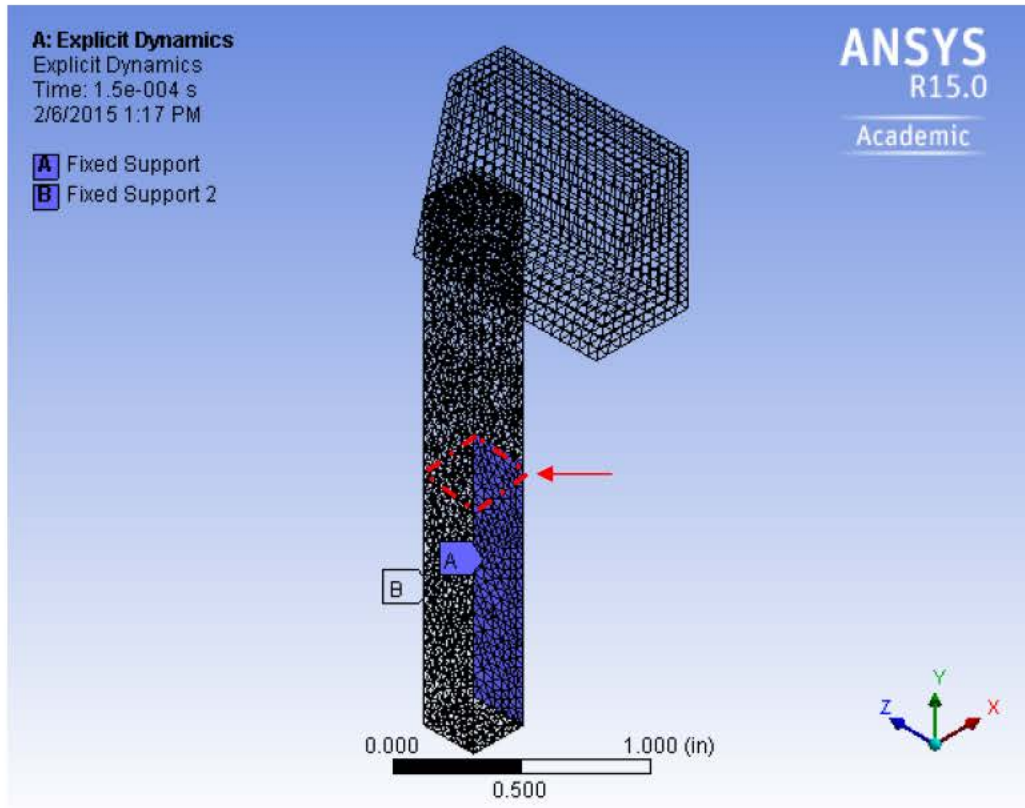


Figure 24. ANSYS Explicit Dynamic refined mesh and support constraints for Izod pendulum impact problem. Plane of interest is outlined immediately above the supports.

The Tinius Olsen test machine instruction manual [23] provides impact velocity values of the pendulum, based on Equation 1.2. An equivalent impact velocity was determined for the adjusted impact wedge mass of the simplified model. The wedge was given an initial velocity immediately prior to impact based on maintaining an equivalent kinetic energy as compared to the original pendulum system as follows:

$$\frac{1}{2} m_{\text{pendulum}} v_{\text{pendulum}}^2 = \frac{1}{2} m_{\text{wedge}} v_{\text{wedge}}^2$$

$$v_{\text{wedge}} = \sqrt{\frac{m_{\text{pendulum}} v_{\text{pendulum}}^2}{m_{\text{wedge}}}} \quad (1.3)$$

Although this approach neglects the losses associated with the Izod impact test as discussed in Section IV. A., this analysis provides a good approximation of the impact velocity of the wedge.

Custom material properties were input into the model using the bulk properties of the LLNL case samples. The density of LLNL case samples was calculated as 1.5 g/cm^3 , and the elastic moduli listed for the radial and circumferential directions listed in Table 1 were input into the custom material. Artificially high yield strength was used for the CFC, since failure of the specimen was not of interest to us for this analysis.

Stress along the plane of the top of the fixed support through the Izod sample (along the line of fracture) was observed. The maximum stress immediately upon impact was desired to ensure that it was bounded by the dynamic yield stress and the static yield stress determined by the SHPB and compression tests.

C. IZOD IMPACT MODEL RESULTS

After confirming the Izod impact problem was producing reasonable results by initially running the simulation with an Al 6061-T6 specimen (Figure 25), the custom material was implemented to simulate the CFC samples tested in the radial and circumferential strike orientations.

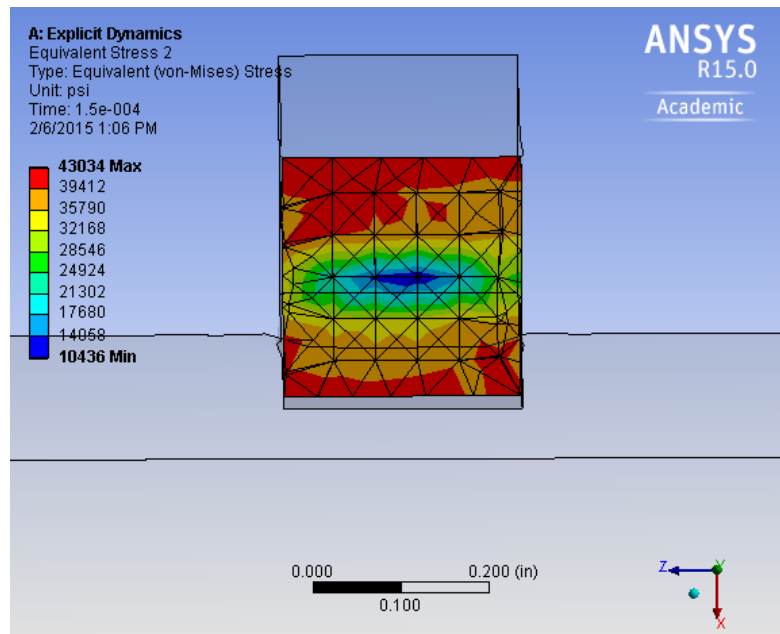


Figure 25. Von-Mises Stress along the plane of the Izod hammer impact for the Aluminum 6061 test specimen.

Figures 26 and 27 display the ANSYS results upon impact of the wedge with the Izod specimen for the radial orientation and the circumferential orientation of the carbon fiber sample. The two figures display nearly the same time step and very similar maximum stresses at the location of the strike and along the location of specimen bending. The resulting maximum stress of approximately 303MPa (44kpi) falls below the maximum dynamic yield stress of the SHPB for both orientations, and above the quasi-static yield stress for the circumferential orientation.

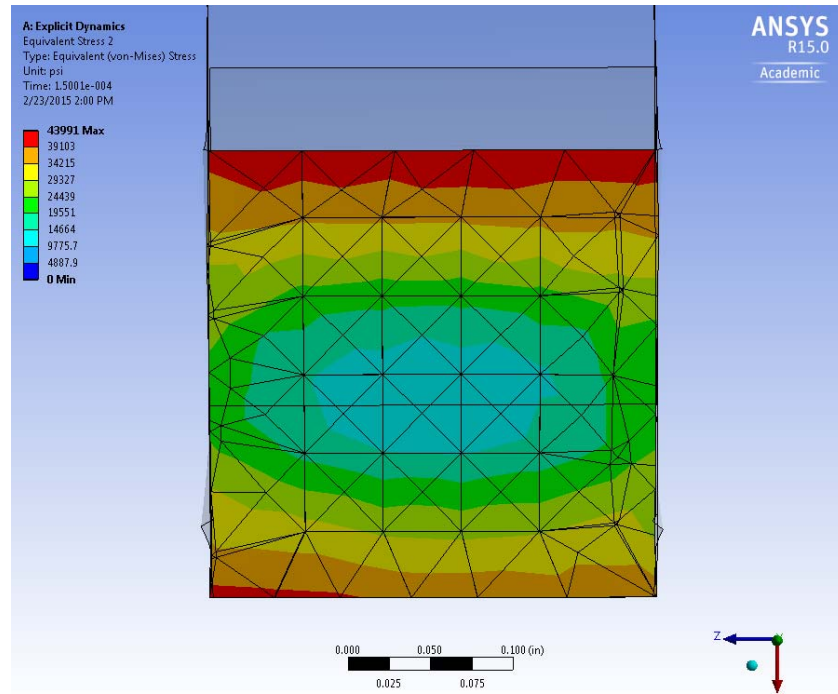


Figure 26. Von Mises stress of CFC Izod sample subject to radial strike orientation (impact wedge not shown).

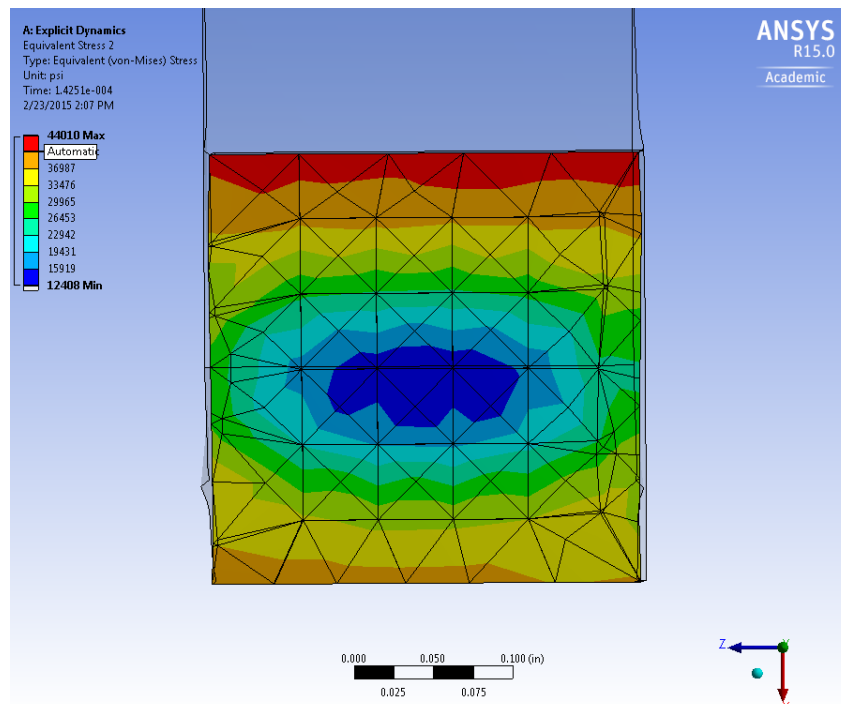


Figure 27. Von Mises stress associated with the circumferential strike orientation of the CFC sample (impact wedge not shown).

Although the maximum Von Mises stress obtained from the ANSYS model for the circumferential strike orientation falls within the expected bounds of the quasi-static and dynamic compression tests, this does not hold true for the radial CFC orientation. This is most likely due to the fact that the failure modes were different between the Izod impact tests and the compression tests for samples in the radial orientation. Whereas the compression samples exhibited high strength and finally failed due to shear damage, the Izod samples exhibited delamination failure due to bending. Each independent test of the various orientations of CFC consistently demonstrated the higher strength of the samples subject to radial loading. However, without a failure model to depict the anisotropic nature of the CFC, ANSYS cannot anticipate that failure in this situation will occur due to delamination.

As a result, this ANSYS model is still a valid preliminary approach to illustrate the stresses in the specimen as a result of pendulum impact. Further analysis would necessitate better implementation of the anisotropic material properties to include a carbon fiber failure model. Additional verification can be performed by comparing the updated CFC material properties to a known isotropic material, such as the Al6061 utilized in the first iteration of this model.

V. ALE3D HIGH-EXPLOSIVE FILLED CASE MODEL

A. MODEL BACKGROUND

ALE3D (Arbitrary Lagrange/Eulerian 2D and 3D) code system is a high performance, multi-physics code which is used to solve a variety of structural, thermal, hydro, and chemical problems. It was developed under the purvue of the U.S. Department of Energy by Lawrence Livermore National Laboratory. It is a code that integrates the science behind physical and material interactions for a wide range of applications. This makes it ideal for modelling dynamic problems that are highly rate-dependent such as hypervelocity impact problems, simulations involving high-explosives, underwater explosions, dynamic heat transfer problems, problems involving complex chemical reactions, and many others [25].

To best simulate the test articles used at LLNL (Figures 3 and 4), a computational model of a simple “pipe bomb” was developed in ALE3D utilizing the second approach discussed. A high explosive (C4) was inserted into a cylindrical shell and detonated at top dead center (TDC). The dynamics of the problem were analyzed initially with a steel shell to ensure the code was operating properly before implementing the carbon fiber code. Dimensions of a typical case (Figure 7) were utilized so that the base model had an inner radius of 3.49cm, an outer radius of 3.81 cm, and a case thickness of 0.32cm. The case height was 17.7 cm.

Due to the axisymmetric nature of the problem, the model was adjusted to have quarter-cylinder geometry with outflow boundary conditions along the symmetry planes. Air was meshed around the case to allow for room for the expanding case and product gases to move into, as displayed in Figure 28. This combined a Lagrangian approach with an Eulerian approach to modelling, so that the material could move through the mesh as relaxation and advection of the material occurred. This was more accurate than a strictly Lagrangian approach,

since it allowed product gases to escape from the pipe as the material fractured. However, as the material advected, some detail was lost around the fractured areas.

The domain was meshed utilizing a coarse mesh consisting of 5520 elements and 6648 nodes, as illustrated in Figure 28. All variations of the models were designed to have the same mesh sizing for consistency in comparing the results. Parameters of greatest interest were the Von Mises stress, circumferential (hoop) stress, C4 pressure and radial case displacement. Fiber stress was also observed in the carbon fiber case, as the fibers are the load carrying component of the composite. These parameters were measured as time history variables in the code and plotted using MATLAB.

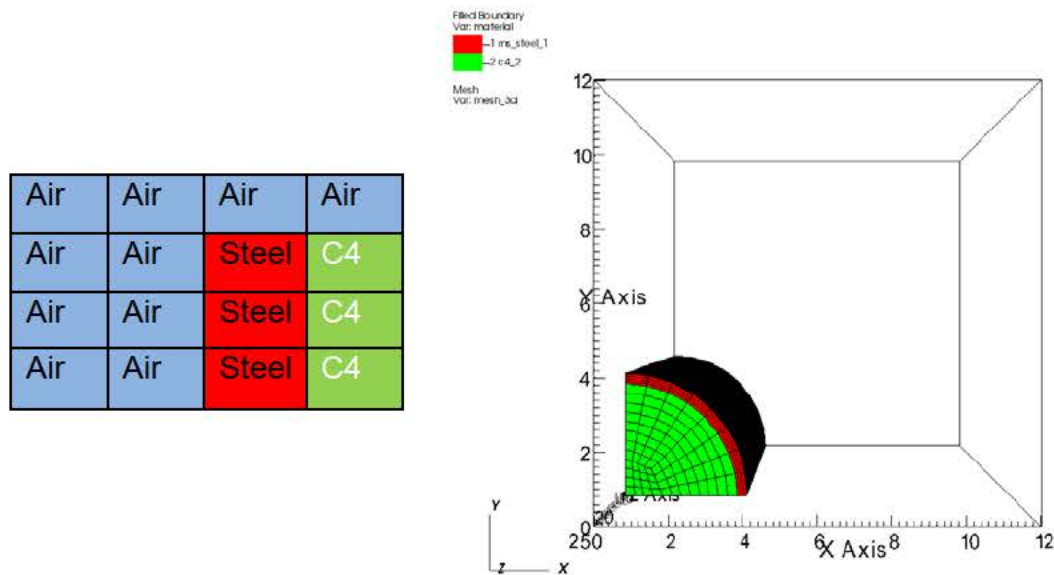


Figure 28. Quarter cylinder geometry (right) was utilized to cut computation time. Green center represents C4 explosive, red cylinder outer layer represents the steel shell. Air (not shown) was meshed around the cylinder as represented by the schematic (left).

The steel case was analyzed with a Johnson-Cook failure model as well as without a failure model. The Johnson-Cook failure model predicts failure (fracture) of ductile materials experiencing high stress or strain rates. It describes

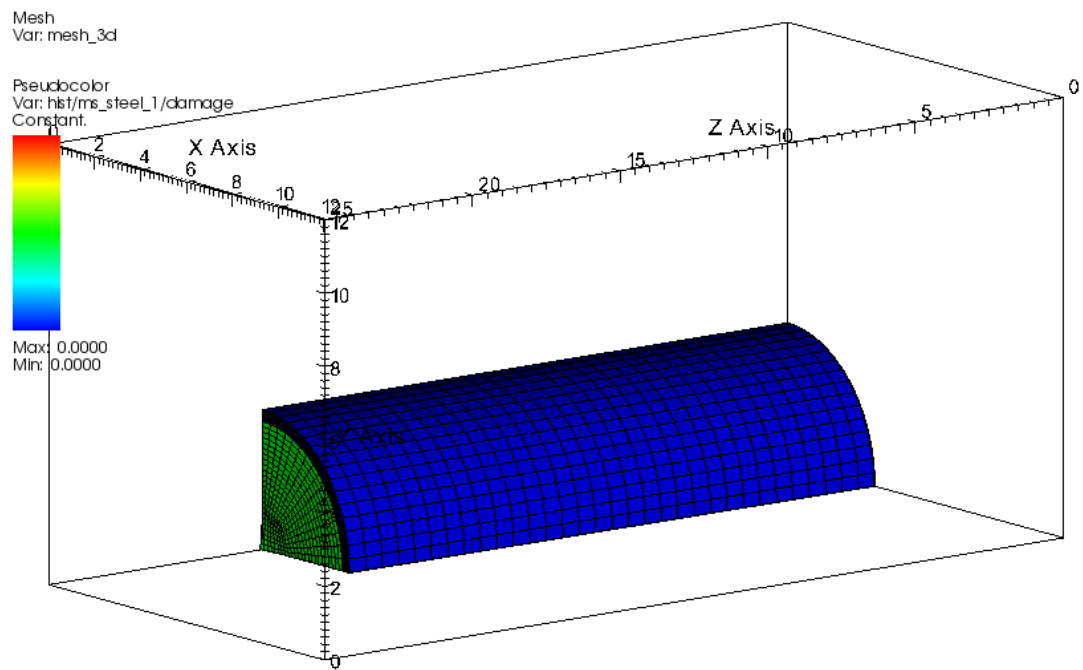
the rate-dependent behavior of the material and operates under the principal that the yield surface changes as the material is deformed. The yield strength of the material is given by:

$$Y = \left(a + b\varepsilon^N \right) \left(1 + c \ln \left(ed1 + \frac{\dot{\varepsilon}}{ed0} \right) \right) \left(1 - T^{*M} \right) \quad (1.4)$$

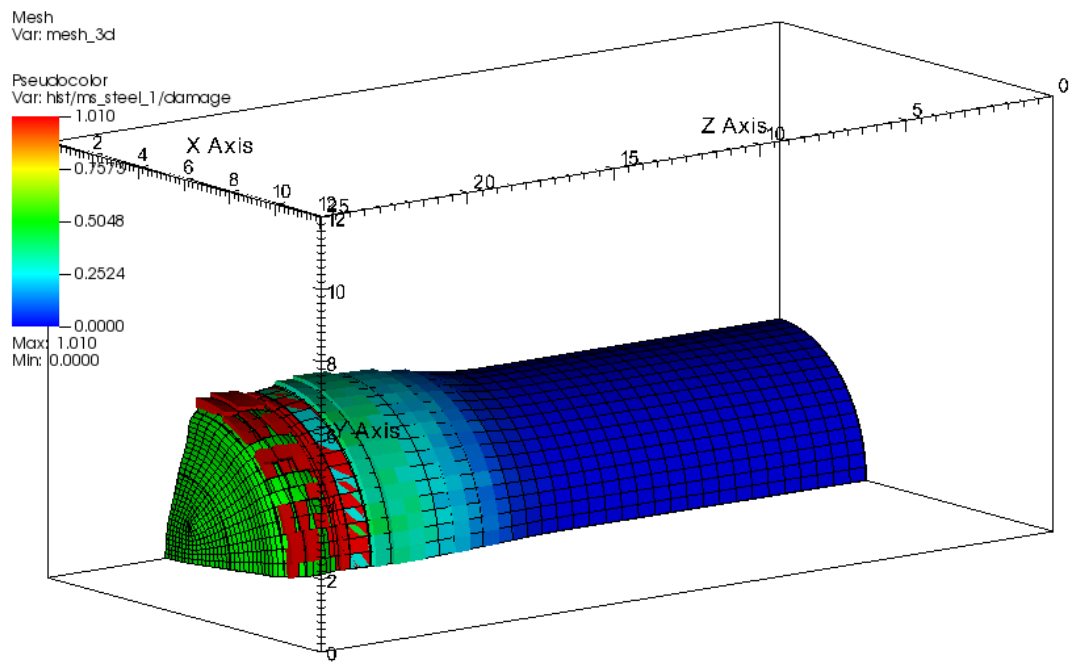
Where a, b, c, N and M are material constants [25]. Failure in the Johnson-Cook ALE3D model is dependent on the material in a given element reaching the failure plastic strain, which is given by the equation [25]:

$$\varepsilon_{fail} = \left(D_1 + D_2 \exp \left(D_3 \frac{p}{\sigma} \right) \right) \left(1 + D_4 \ln \left(ed1 + \frac{\dot{\varepsilon}}{ed0} \right) \right) (1 + D_5 T^*) \quad (1.5)$$

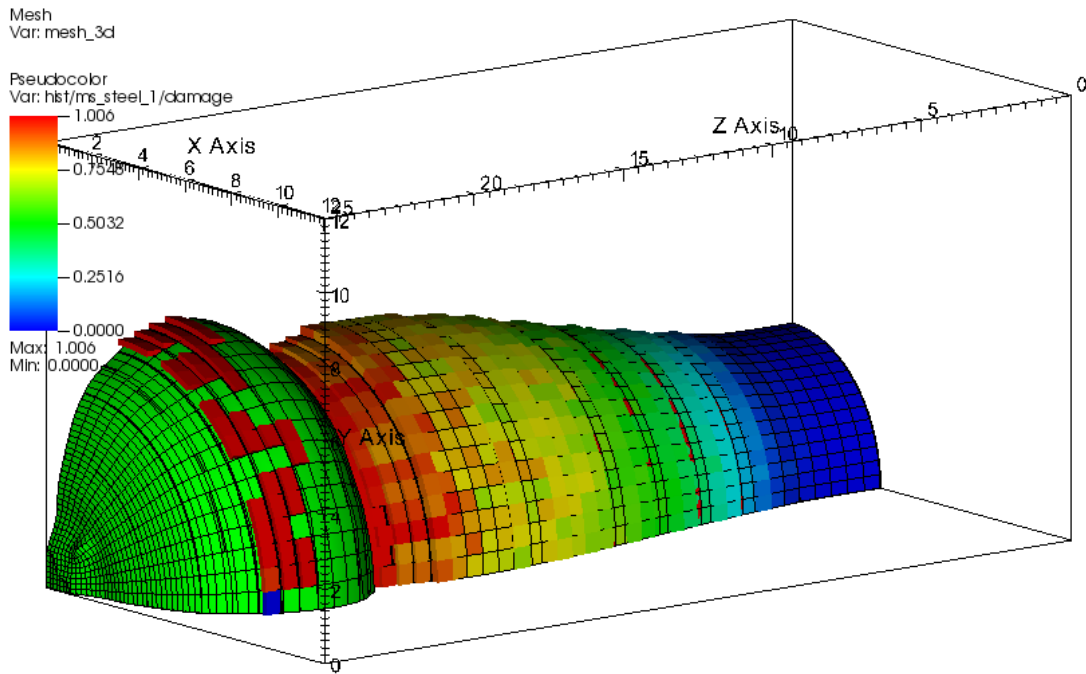
where the D coefficients are damage parameters. When the damaged element reaches the failure plastic strain, that element has fractured and the resulting stresses are zero. ALE3D incorporates the material parameters required for use of this failure model on ductile materials such as steel and aluminum. Typical damage progression of the explosion within the case is illustrated in Figure 29, where the red/orange color indicates a damage value of 1.0 or greater and that the material has fractured. To model the steel case without the failure model, the same code was used for simplicity with the yield stress arbitrarily raised so that the failure model had no effect.



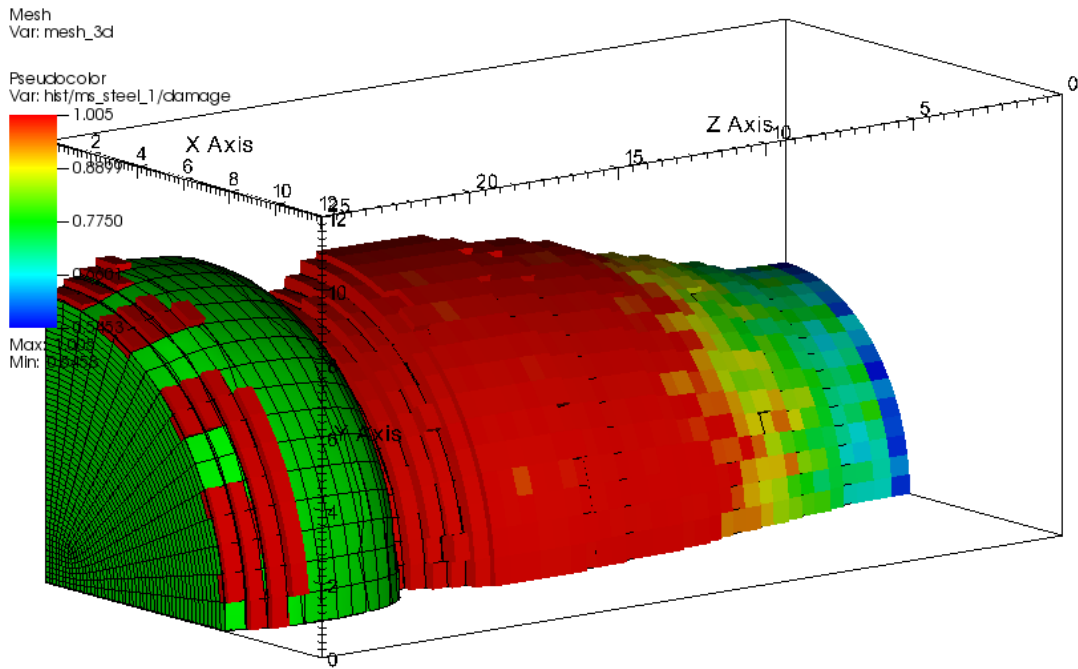
A.



B.



C.



D.

Figure 29. VisIt images depicting expansion of HE and damage progression of steel case with failure model at a time of: A. $1\mu\text{sec}$, B. $10\mu\text{sec}$, C. $20\mu\text{sec}$ and D. $30\mu\text{sec}$. A damage value of 1.0 is considered a failed element.

In addition to modeling the steel case with and without the failure model, the steel case was also modeled as having either an equivalent thickness as the carbon fiber case, or an equivalent mass. The steel case with the equivalent mass was the same length and inner diameter as the CFC case, but the thickness was reduced significantly, as observed in Figure 30. Properties of each case configuration, to include dimensions of the model, are summarized in Table 5 and detailed in Appendix C.

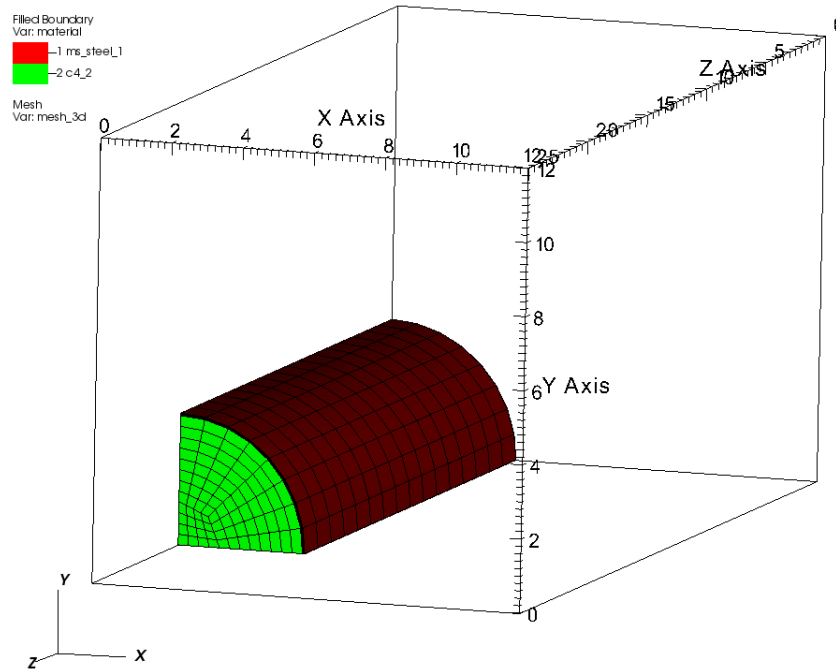


Figure 30. Image of the steel case and mesh with equivalent mass as the CFC case. The case thickness for the “thin” steel case was 0.07cm (0.026”).

B. IMPLEMENTATION OF THE CARBON FIBER MODEL

With the pipe bomb model functioning as expected, the composite code developed by Drs. Y.W. Kwon and M.S. Park was integrated into the model. This code analyzes the composite unit cell to predict material stresses and strains. The unit cell is the “smallest representative volume that can describe the repetitive geometry and mechanical properties” [26] of the composite material.

The model analyzes the unit cell by sectioning it into eight subcells, as illustrated in Figure 31, each of which contain either the fiber(s) or matrix.

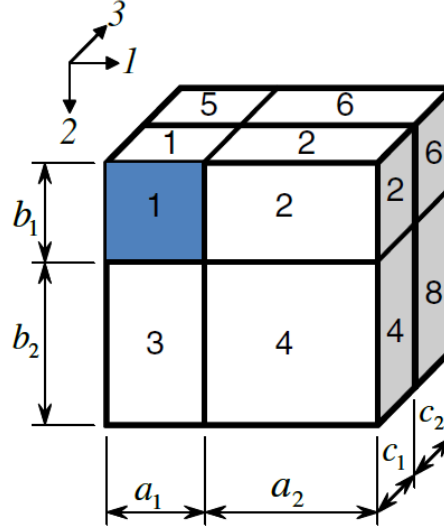


Figure 31. The unit cell composed of eight subcells utilized in Kwon and Park's micromechanics model, from [27].

The stresses and strains within each of the eight subcells are considered uniform and the boundaries of adjacent subcells equate shear and normal stresses [26]. The subcells have the capability to account for a composite model with long fibers, short whiskers, particulates and/or microvoids within the matrix. The code requires inputs of the fiber orientation and the mechanical properties of the matrix and fiber(s), to include volume fraction, elastic modulus, poisson's ratio and yield strength. Once the subcell properties are calculated based on the geometry and the individual constituent properties, as described by Kwon and Park [27], the volume average of the subcell properties are then applied to the unit cell of the composite.

$$\begin{aligned}\bar{\sigma}_{ij} &= \sum_{n=1}^8 V^n \sigma_{ij}^n \\ \bar{\epsilon}_{ij} &= \sum_{n=1}^8 V^n \epsilon_{ij}^n\end{aligned}\tag{1.6}$$

Equation 1.6 displays the unit-cell stress and strain based on the volume fraction of the n -th subcell (V^n) and the n -th subcell stress (σ^n) or strain (ϵ^n). The finite element analysis is then conducted on the composite composed of the unit cells, and the resulting deformation, stresses and strains are obtained for the composite as a whole structure [27]. The results for the composite structure are then decomposed by the micromechanics model to determine the stresses and strains experienced by the fibers and matrix on the unit cell level. The model differs from most commercial models, which approximate the composite properties by averaging the properties of the matrix and fibers based on volume fraction of the constituents, then applies the averaged values through the composite volume. These commercial models cannot predict failure of the individual constituents as Kwon and Park's code can.

The unit cell micromechanics model was implemented in ALE3D utilizing a simple 4-layer cylindrical composite consisting of fiber orientations of 10° , 45° , 10° and 80° for each respective layer (Figure 32). These orientations were chosen to model a simplified LLNL case, which is typically manufactured with 12 repeat layers of the same fiber orientations. Although Kwon's composite code currently models the fiber and matrix with quasi-static yield stress, a dynamic failure model similar to the Johnson-cook model for the ductile materials is still needed.

The purpose of performing the SHPB tests was to obtain high strain rate data necessary for implementation into the dynamic model. However, at the time of this writing, the dynamic model is still in development. Because of the lack of dynamic failure model for the CFC, comparison of the current quasi-static model was made both with steel cases containing the Johnson-cook failure model and without.

C. COMPARISON OF STEEL CASE AND CFC CASE

Figure 32 illustrates the CFC case with typical dimensions as Figure 7 and coarse mesh. This carbon fiber case was compared to four steel models:

1. A “thin” steel case (having equivalent mass as the CFC case) without a failure model.
2. A “thin” steel case (having equivalent mass as the CFC case) with a Johnson-cook failure model.
3. A “thick” steel case (having equivalent thickness as the CFC case) without a failure model.
4. A “thick” steel case (having equivalent thickness as the CFC case) with a Johnson-cook failure model.

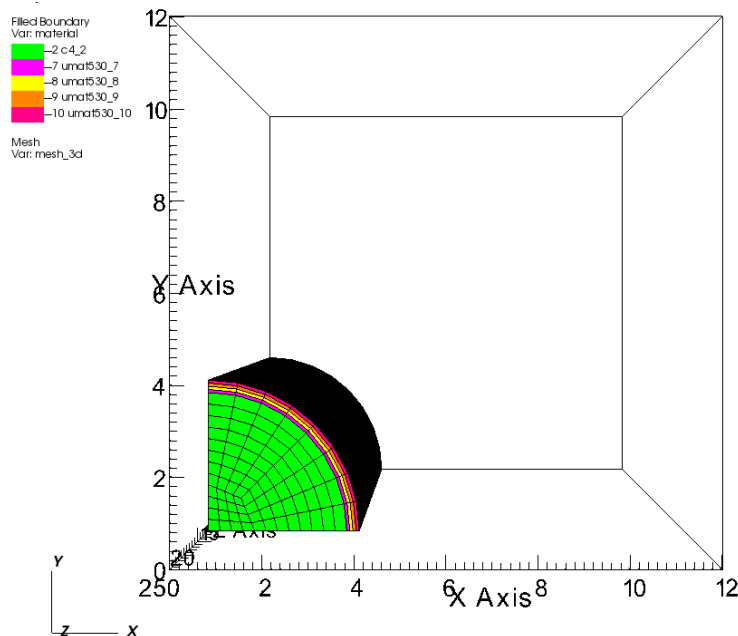


Figure 32. Image depicting the mesh used for CFC case analysis containing 5520 elements and 6648 nodes.

Comparison was made between the cases by comparing the previously discussed time history variable of interest at six axial locations along the length of the shell: 0cm, 5cm, 10cm, 15cm, 17.7cm and 20cm. The 0cm location represented the point at the base of the case, furthest from the detonation point. The 17.7 cm location was the height at which the detonation originated. The

20cm location was a point in the air hovering over 2cm above the rim of the case. The first time history variable of interest was the radial expansion of the case. Figure 32 displays a graph of the radial expansion of the CFC case at five different axial locations (no useful data was obtained from the 20cm point outside of the case). A comparison of the four steel cases can be observed in Figure 34.

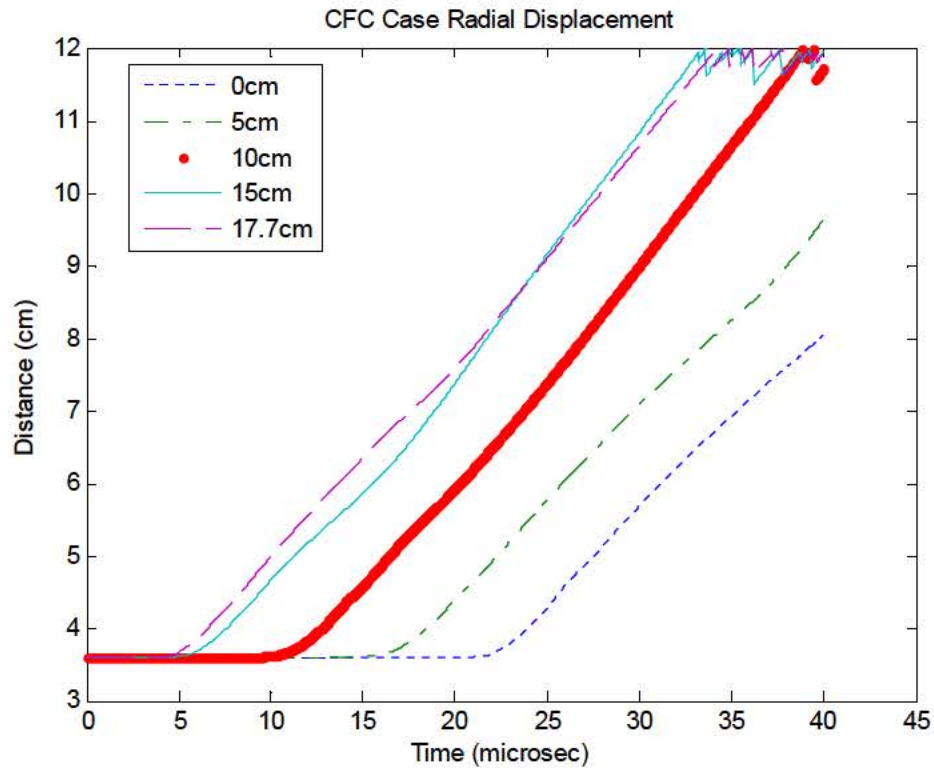


Figure 33. Graph illustrating the radial expansion of the CFC case at five axial locations measured from the base of the case along the carbon fiber shell. The locations are measured at the midpoint of the case thickness.

The CFC graph depicting radial expansion of the case followed a predictable pattern as the elements located near the detonation location (17.7cm and 15cm) experienced deformation and displacement sooner than the case elements located farther from the detonation (10cm through 0cm). The element at 20cm was an element of air, so the displacement of this element was due to the pressure associated with the blast and the expansion of the product gases.

Displacement of this element was not included in Figure 33. It should be noted that at a time of about 30 microseconds, the tracer particles tracking displacement for axial locations of 15cm and 17.7cm moved outside of the meshed domain. This explains the saw-tooth graph for the radial displacement after 30 microseconds, due to the program attempting to “find” the tracer particle.

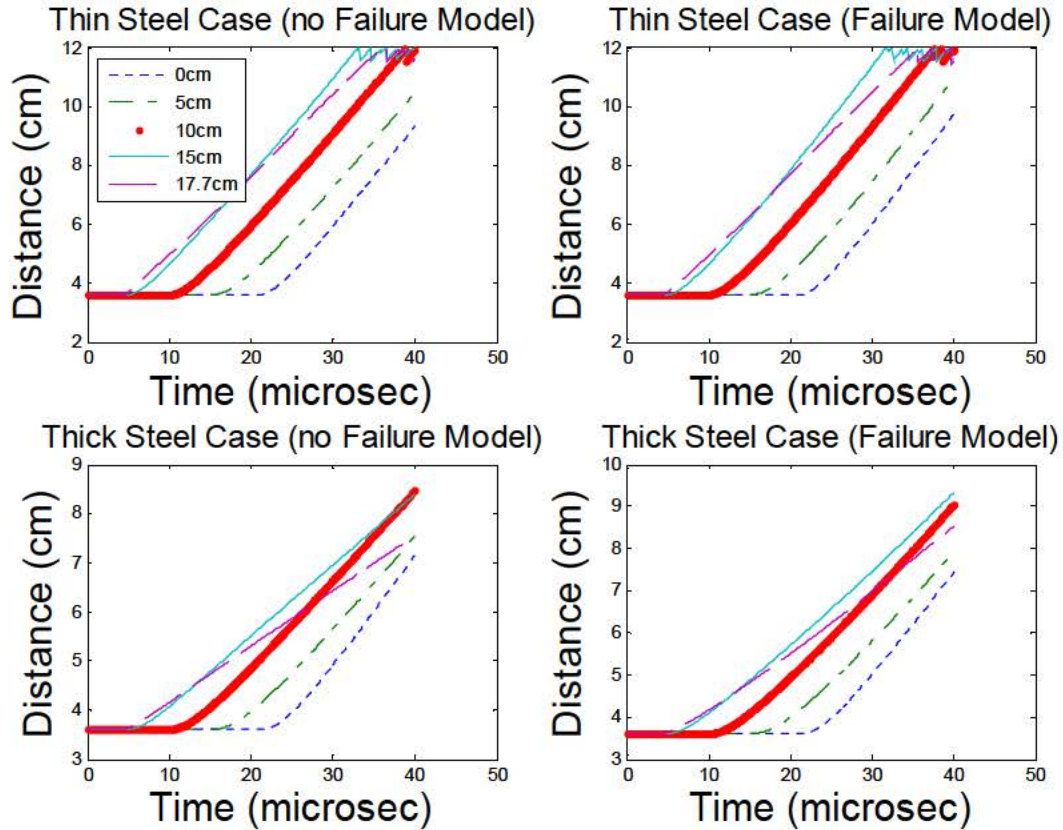


Figure 34. Graph illustrating the radial expansion of the steel cases at five different axial locations along the shell. (Left) Cases contain no failure model. (Right) Cases contain failure model. (Top) Cases are mass-equivalent to the CFC case. (Bottom) Cases have equivalent thickness as the CFC case.

No significant difference in radial displacement of the steel cases was seen between the models containing the Johnson-cook failure model and those without. The steel cases with equivalent mass as the carbon fiber case experienced nearly identical displacement at every longitudinal location and time

step. The steel cases with the equivalent thickness as the carbon fiber contained the HE for slightly longer prior to case failure, a parameter known as containment time. This resulted in a lower value for radial displacement at every time step. Unlike the CFC case and the thin steel cases, the fragments of the thick case never exit the meshed domain. It appears that mass of the case plays a large role in the radial displacement of the case fragments. The cases with larger masses, regardless of failure model, exhibit longer containment time and slower radial expansion, as illustrated in Table 5.

The next parameter of interest was the Von Mises stress. The same six axial locations were analyzed for each of the previous models. Figure 35 displays the Von Mises stress experienced within the CFC case. Without a failure model, the maximum stress achieved in this case was on the order of 45 GPa, which is significantly larger than the steel cases without the Johnson-cook failure models implemented (Figure 36).

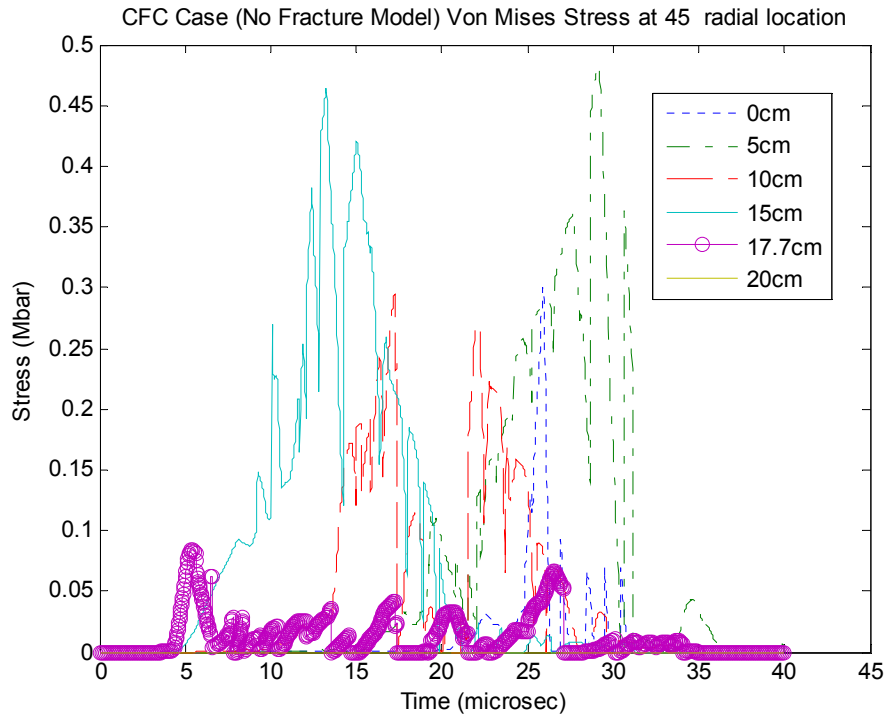


Figure 35. Graph of Von Mises stress within the CFC case at six axial locations along the case.

Significant thinning of the CFC case occurred prior to the case failing, as illustrated in Figures 37 through 40. As the case thinned, the associated stresses increased drastically. Judging from the different stresses obtained by the steel cases, the average Von Mises stress could be up to an order of magnitude lower when the failure model is applied, as shown in Table 5.

As discussed previously, when the case material elements began to expand due to the high explosive detonation, the eroded space around the element was filled with void and the stress associated with this element was reduced to zero. The graphs displayed in Figures 35 and 36 show drastic reductions in the Von Mises stress because the tracer particles picked up the void material around the eroded elements. As expected, no stress is felt at the 20 cm axial location, as this element represented the air outside of the case.

With a failure model implemented, it was expected that each axial location be subjected to approximately the same Von Mises stress prior to failure. This was seen in the thick steel case with fracture model in the lower right graph of Figure 36, as pointed out by the box. The thin steel case with fracture model followed this trend until the detonation front reached the 5cm and 0cm locations near the bottom of the case, where a large portion of the case fractured and some of the energy had already dissipated.

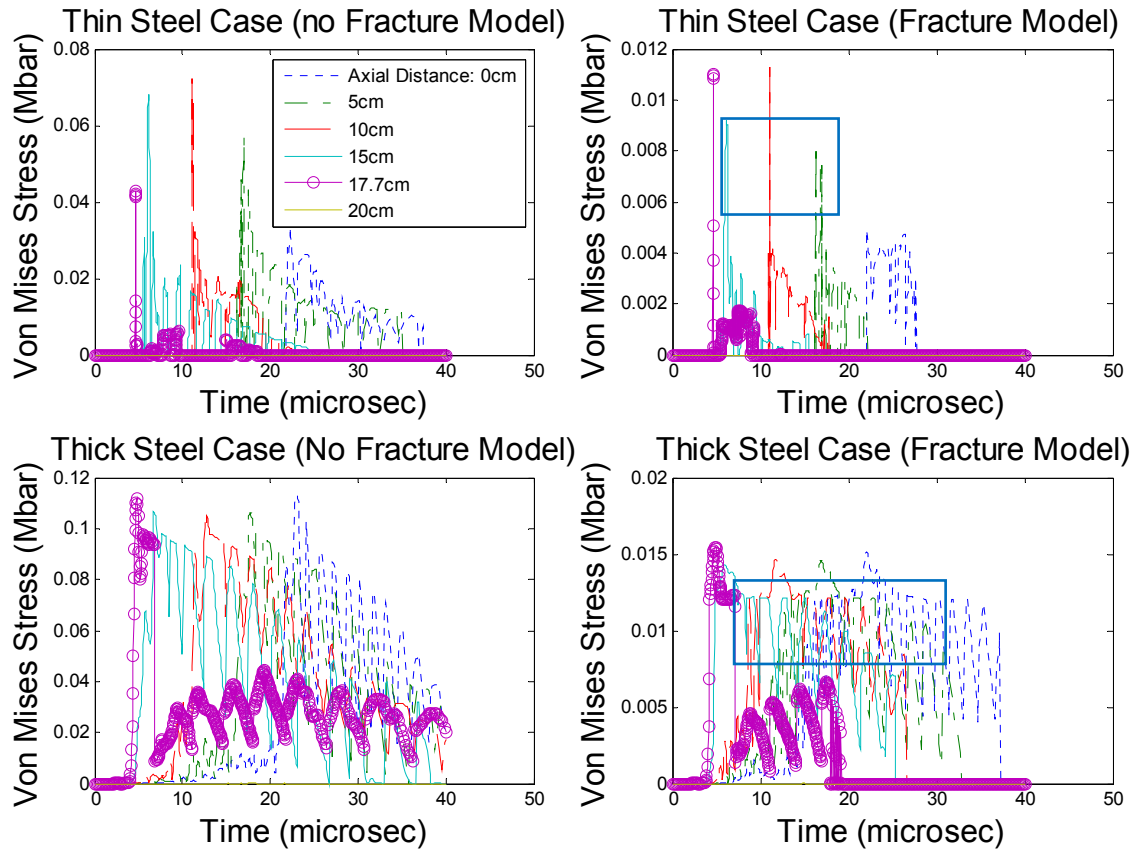


Figure 36. Comparison of steel case Von Mises stresses, without fracture models (left) and with fracture models (right). The color legend is the same for each case.

Table 5. Summary of the five different model input parameters and results.

					Average Radial Displacement (cm) at time=		
Model	Thickness cm(in)	Length cm(in)	Max Von Mises Stress Mbar (GPa)	AVG. Von Mises Stress GPa	10 microsec	15 microsec	20 microsec
Carbon Fiber Case (1/8")	0.32 (.126)	17.8cm (7in)	0.48 (48)	4.3	4.05	4.76	5.72
Thin Steel Case(no fracture model)	0.067 (.026)	17.8cm (7in)	0.072 (7.2)	0.29	4.04	4.79	5.78
Thin Steel Case (with fracture model)	0.067 (.026)	17.8cm (7in)	0.011 (1.1)	0.031	4.04	4.79	5.82
Thick Steel Case (no fracture model)	0.32 (.126)	17.8cm (7in)	0.11 (11)	2.73	3.81	4.26	4.84
Thick Steel Case (with fracture model)	0.32 (.126)	17.8cm (7in)	0.015 (1.5)	0.42	3.81	4.28	4.92

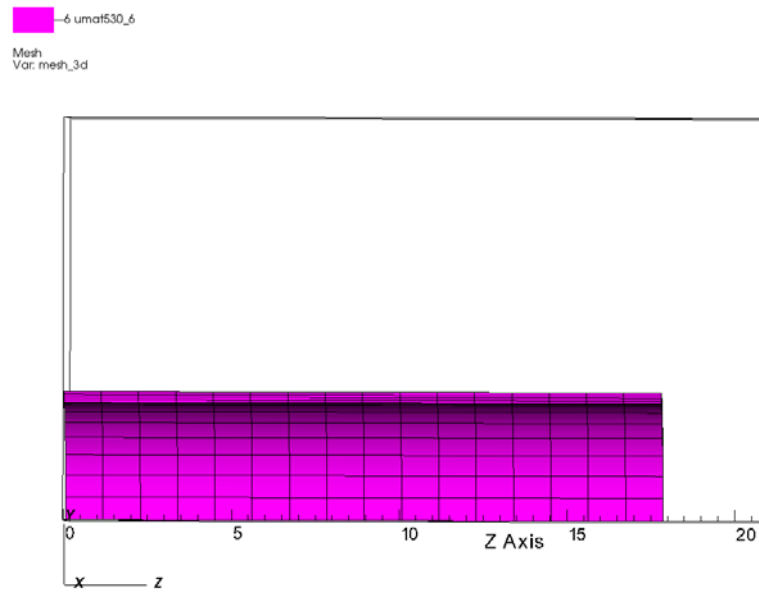


Figure 37. Initial CFC case quarter geometry and mesh. The HE fill interior is hidden.

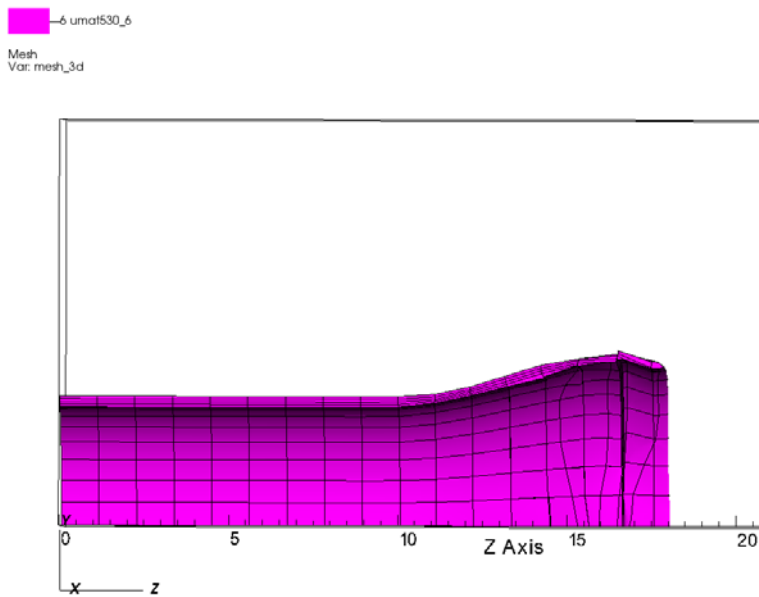


Figure 38. CFC at a time of 10 microseconds after detonation. Thinning of the case is observed near the top of the case.

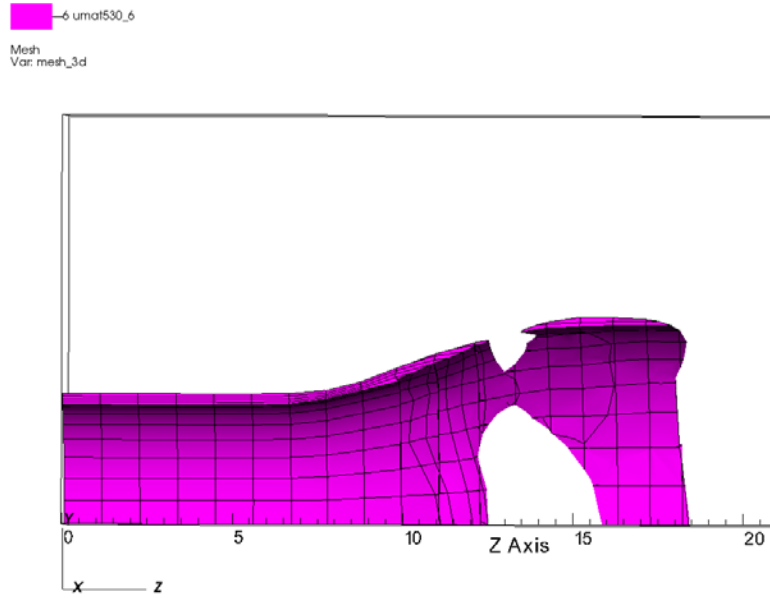


Figure 39. CFC at a time of 14 microsecond following detonation. Case thinning and erosion of elements is observed.

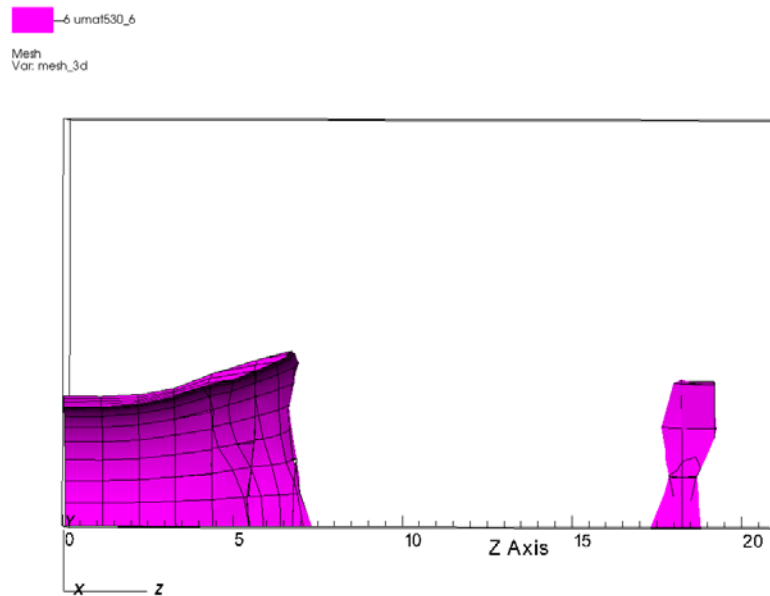


Figure 40. CFC case at a time of 20 microseconds following detonation. Significant case failure and erosion of CFC elements are observed.

Comparison of the hoop (circumferential) stress for each case is summarized in Table 6, analyzed at each of the axial positions discussed previously. The hoop stress, predictably, followed the same trend as the internal

pressure results, which are displayed in Table 7. It was originally anticipated that the hoop stresses be largest for the cases that contained the highest internal pressure and the thinnest case wall. Figure 41 illustrates the hoop stress experienced by the CFC case.

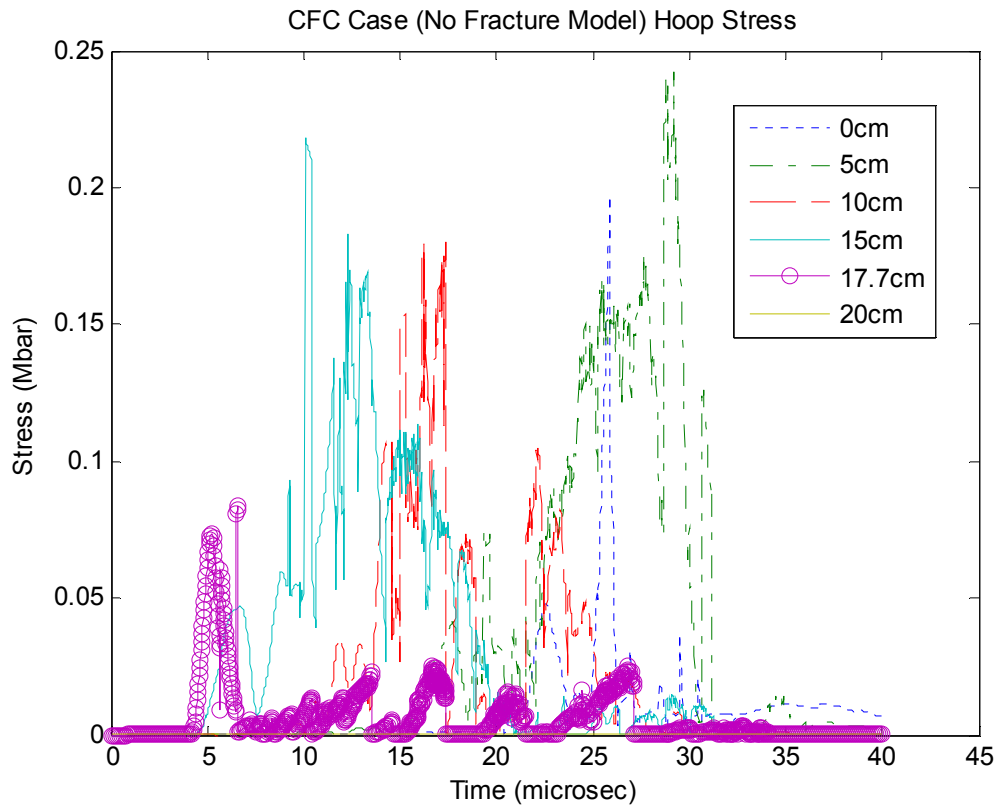


Figure 41. Hoop (circumferential) stress of the CFC case at varying axial locations.

As displayed in Figures 37 and 38 previously, the CFC case experienced significant thinning prior to erosion of the case as the detonation front advanced. The thinned wall contributed to the high stresses observed. As a quick check, the anticipated hoop stress was calculated based on expected quasi-static hoop stress from the geometry of the CFC case displayed in Figure 32 and from the maximum detonation pressure (10 GPa) and average detonation pressure (0.8 GPa) given in Figure 42. Although containment of the HE within the cases

caused maximum internal pressure to peak at a higher value than the maximum detonation pressure, the average and maximum pressure at the detonation point did not vary significantly between the different cases so this point was used as an estimate. From Equation 1.7, the expected quasi-static average hoop stress for the CFC case was significantly larger than the observed hoop stress, but on the same order of magnitude:

$$\sigma_{hoop} = \frac{Pd}{2t}$$

$$\sigma_{hoop,max} = 119 \text{ GPa} (1.19 \text{ Mbar}) \quad (1.7)$$

$$\sigma_{hoop,average} = 9.5 \text{ GPa} (0.095 \text{ Mbar})$$

This calculation was a very rough estimate since it assumed constant pressure and thickness and neglects a failure mechanism; however, it was helpful for obtaining an approximate bound to compare the observed results to.

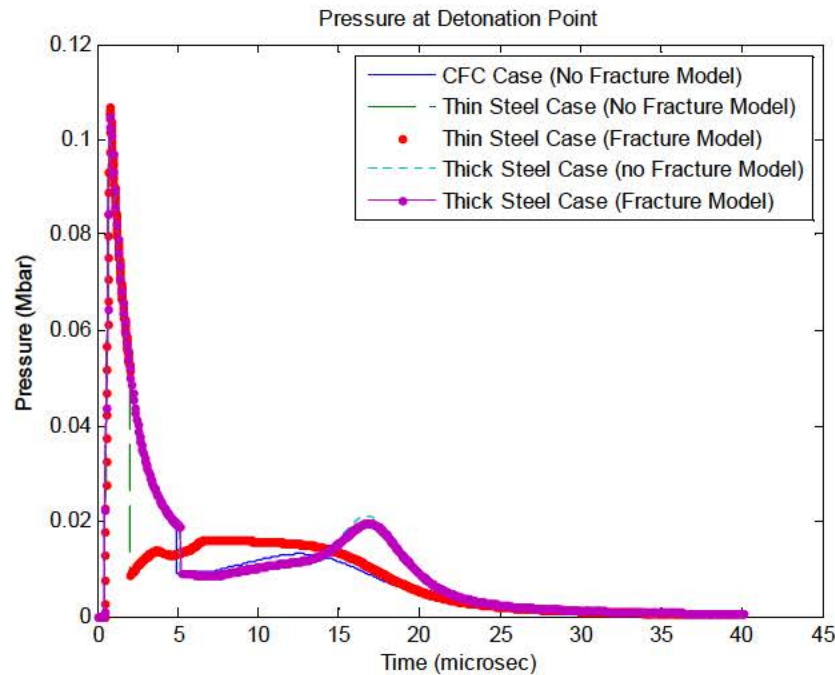


Figure 42. Pressure at the detonation location for each model analyzed. The detonation pressure was identical for both thin steel cases and very similar for the CFC and thick steel cases.

Although from the quasi-static analysis of hoop stress given in Equation 1.7, it appeared that the thin walled cases would exhibit greater hoop stress than the thick walled cases, Figure 43 and Table 7 illustrate this was not the case. Due to the thicker cases exhibiting a larger containment time, the internal pressure climbed to larger values for the thick steel cases. The larger average pressure, displayed in Table 7, resulted in higher hoop stresses.

Table 6. Summary of maximum and average hoop stress results.

Model	Max Hoop Stress (Mbar)	Average Hoop Stress (Mbar)	Average Hoop Stress (GPa)	Standard Deviation
Carbon Fiber Case (1/8")	0.2421	0.0202	2.02	0.0200
Thin Steel Case(no fracture model)	0.0780	0.0023	0.225	0.0029
Thin Steel Case (with fracture model)	0.0790	0.0016	0.162	0.0022
Thick Steel Case (no fracture model)	0.1544	0.0187	1.869	0.0092
Thick Steel Case (with fracture model)	0.2138	0.0097	0.9705	0.0107

Additionally, the steel cases with failure models exhibited fracture much sooner than the cases without the failure model. This resulted in the product gases escaping and the pressure decreasing. The failure model results in lower average pressures and average hoop stresses than the cases with no failure model. This trend is observed for the average hoop stress in Table 6 and the average pressure in Table 7.

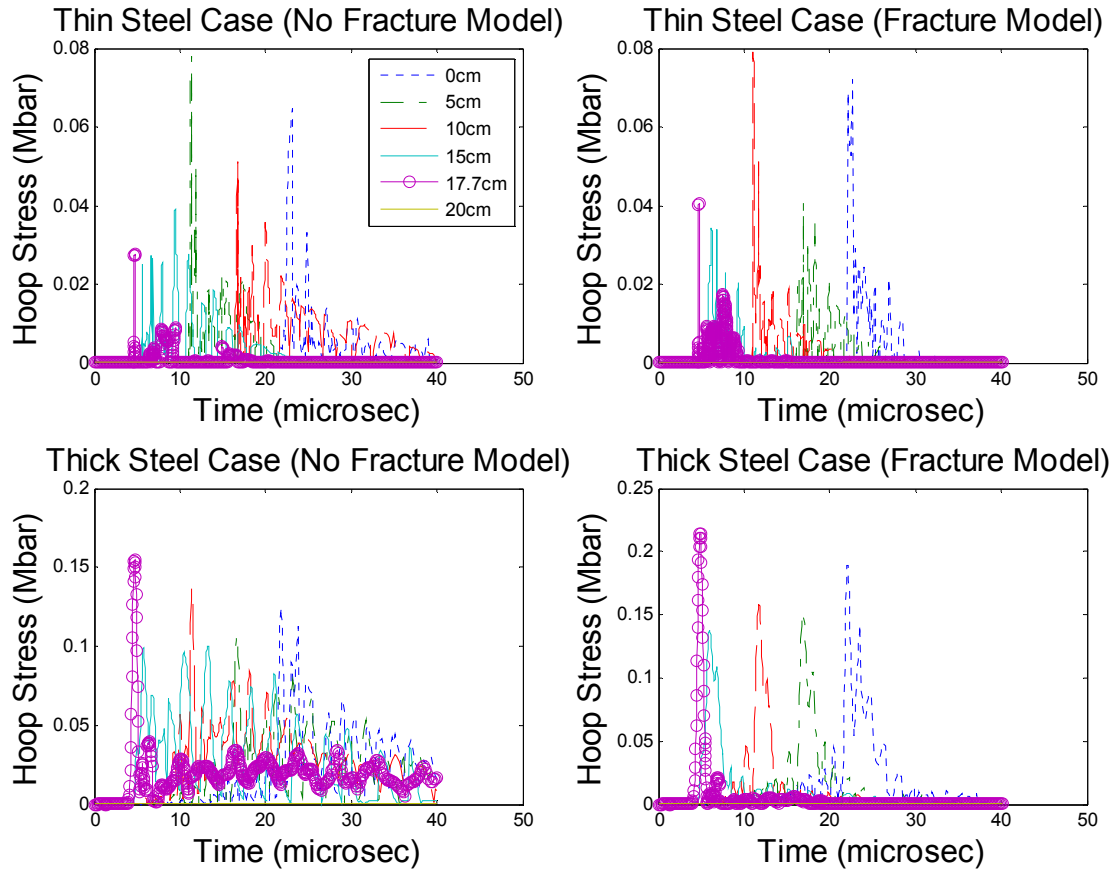


Figure 43. Hoop stress of steel cases at varying axial locations.

Table 7. Maximum and average pressures exerted on the interior case wall by the C4.

Model	Max Pressure (GPa)	Average Pressure (GPa)
Carbon Fiber Case (1/8")	9.5445	0.6880
Thin Steel Case(no fracture model)	5.4790	0.1851
Thin Steel Case (fracture model)	5.1944	0.1290
Thick Steel Case (no fracture model)	9.5895	1.2984
Thick Steel Case (fracture model)	14.7924	0.8138

Pressure of the C4 (internal pressure) at various axial locations along the length of the cases is represented by the CFC case in Figures 44–48. Appendix C contains additional Figures with the pressure results for the steel cases. Average pressure values exerted on the cases at various time steps closely follow the average hoop stress results; although peak localized pressure values do not appear to follow any trend with respect to case thickness or failure model. As observed in Table 6, the average pressures for the thick steel cases were significantly larger than that of the thin steel cases. This increased C4 pressure exerted on the case is expected since the thick steel case exhibited a longer containment time, allowing pressure to build for slightly longer. The CFC case exhibited an average internal pressure value that fell between the thick and thin steel cases, although it experienced the largest average hoop stress due to thinning of the case.

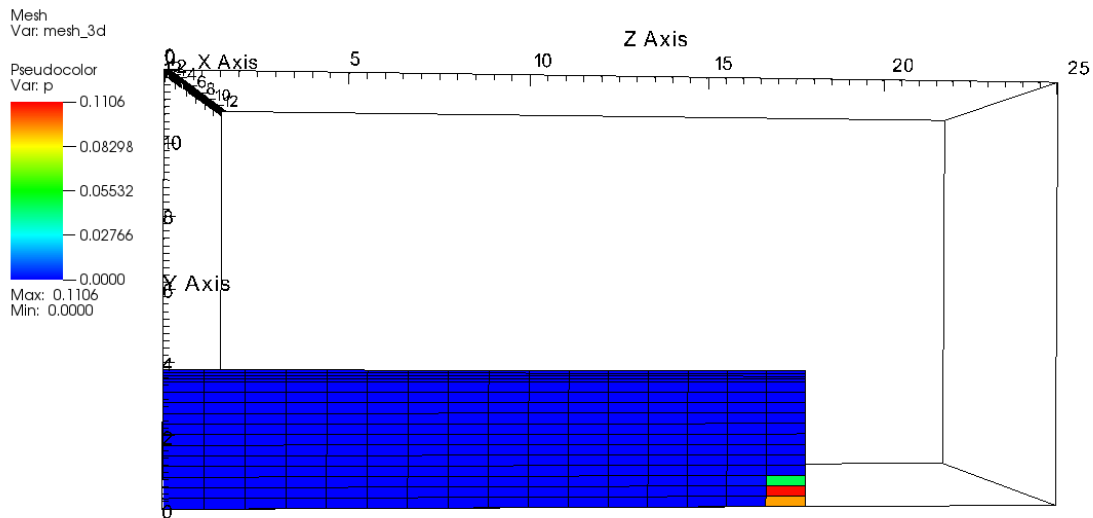


Figure 44. HE pressure within the CFC case at a time of 1 microsecond.

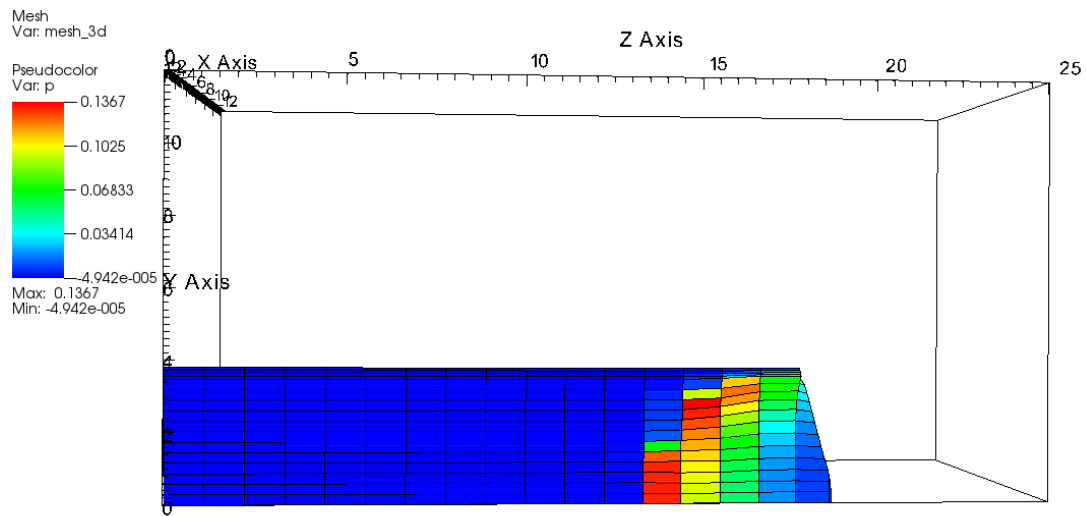


Figure 45. HE pressure within the CFC case at a time of 5 microseconds.

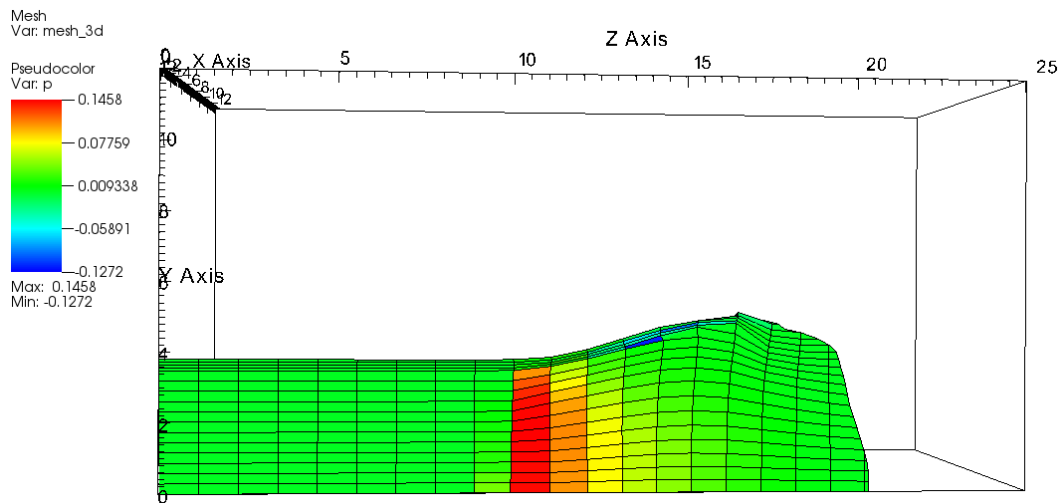


Figure 46. HE pressure within the CFC case at a time of 10 microseconds.

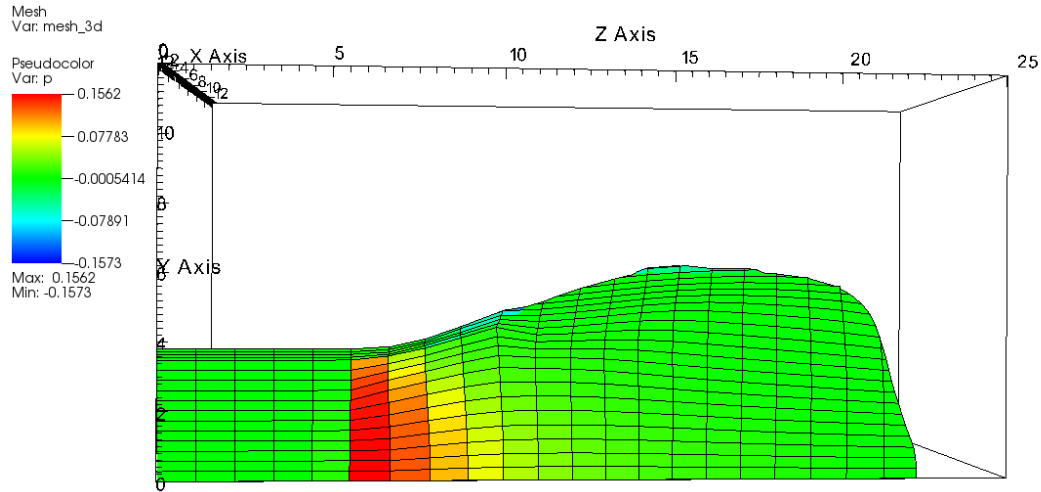


Figure 47. HE pressure within the CFC case at a time of 15 microseconds.

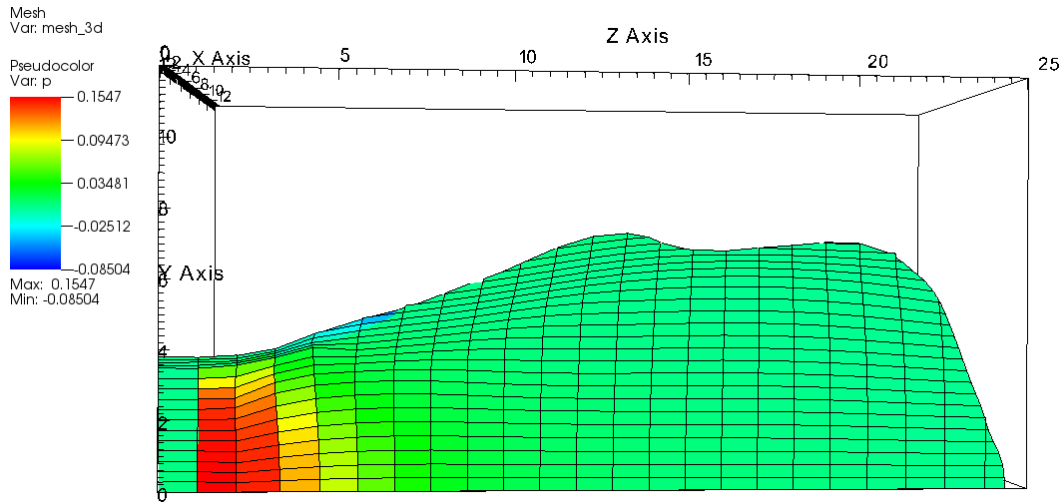


Figure 48. HE pressure within the CFC case at a time of 20 microseconds.

Approximate case containment times were established on the basis that the case would be considered completely failed when 75% of the case material was fractured. The cases with failure models contained time history files of the damaged parameters, so estimation of case failure was straight forward. The cases without failure models required estimation of hold time based on the fracture pattern of the case, radial expansion and Von Mises stress. The most accurate comparison will be achieved once the dynamic failure model is implemented for the CFC case.

Both the carbon fiber and the “thin” steel case (with failure model) exhibited containment times of approximately 20 microseconds. The “thick” steel case (with and without failure model) lasted 50% longer, exhibiting a containment time of about 30 microseconds. Although it was difficult to ascertain the extent of damage on the “thin” steel case without the failure model, it appeared that this case fractured prior to 20 microseconds.

Lastly, in addition to observing the Von Mises and hoop stress of the CFC case, which were calculated from the average constituent properties, the stress was observed at the fiber and matrix unit cell level. Figures 49 through 51 illustrate the fiber stress at 15cm, 10cm and 5cm axial locations for each layer of fiber orientation. The fiber stress at the unit cell was plotted by taking the average of all unit cells at a given axial location. Additionally, the constituent yield strengths are plotted for the fiber, matrix, and the highest experimentally determined LLNL case yield strength. The fiber stresses were of interest more than the matrix stress since the fibers added stiffness to the composite and were the primary load-carrying components. The matrix primarily served to add toughness [26] and contain the fibers so that the fibers did not buckle under compressive load.

ALE3D Average Fiber Stress for 15cm Axial Location

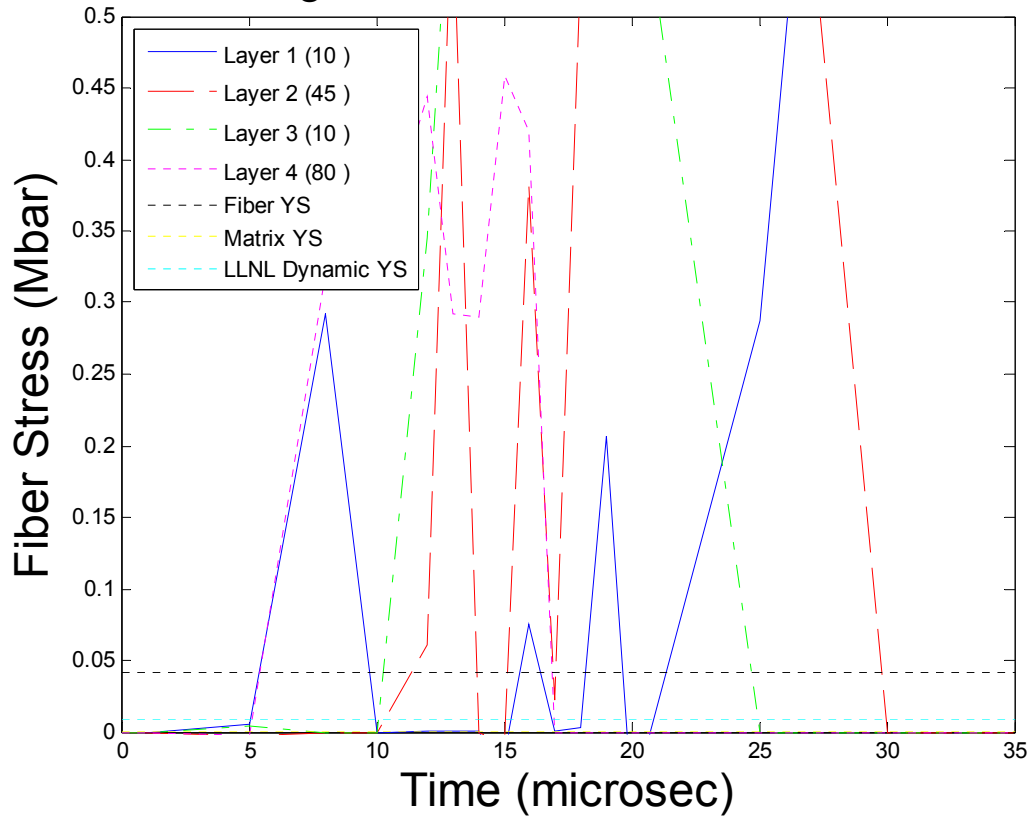


Figure 49. Unit cell level fiber stress averaged for all unit cells along the 15 cm axial location for each layer.

It was expected that the layer(s) containing fibers oriented close to the circumferential direction (90°) would stiffen the composite in the hoop direction and contribute to increased composite strength. From Figure 49, it was layer 1 and layer 4 that reached the critical stress and failed first. This was due to the fact that layer 4 carried more stress due to the larger stiffness associated with that fiber orientation as the HE and product gases expanded outward. Likewise, layer 1 contained fibers oriented perpendicular to the circumferential orientation, which helps explain the early failure.

ALE3D Average Fiber Stress for 10cm Axial Location

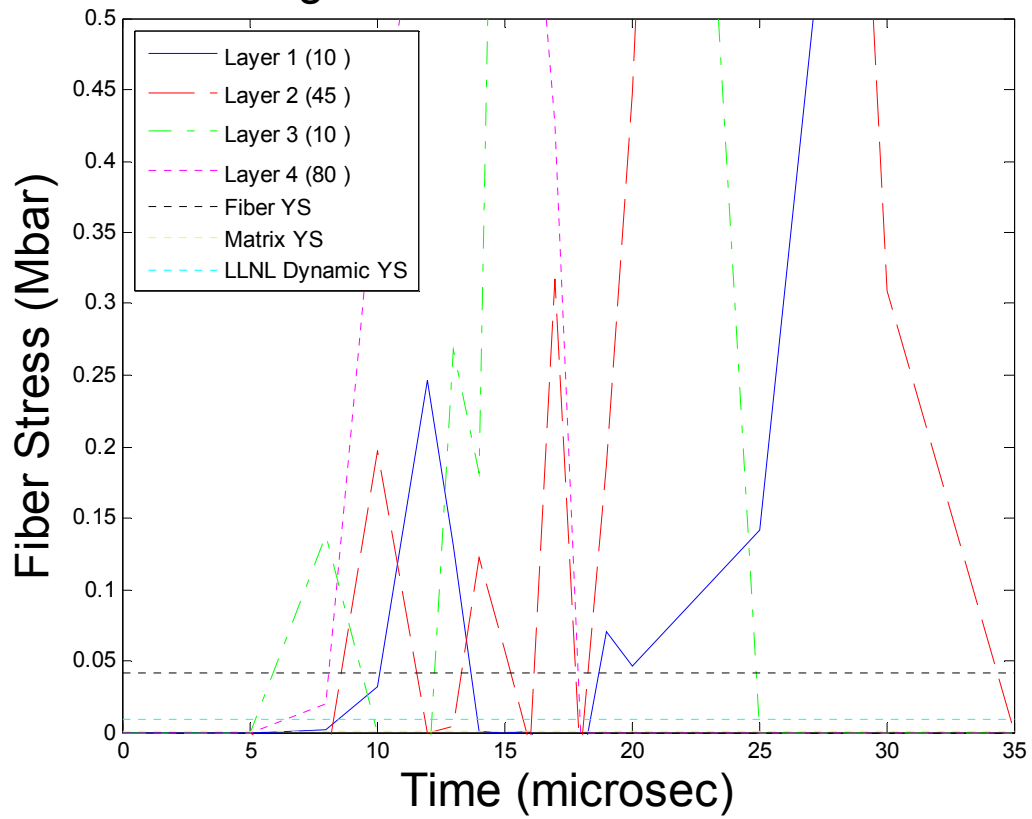


Figure 50. Unit cell level fiber stress averaged for all unit cells along the 10 cm axial location for each layer.

ALE3D Average Fiber Stress for 5cm Axial Location

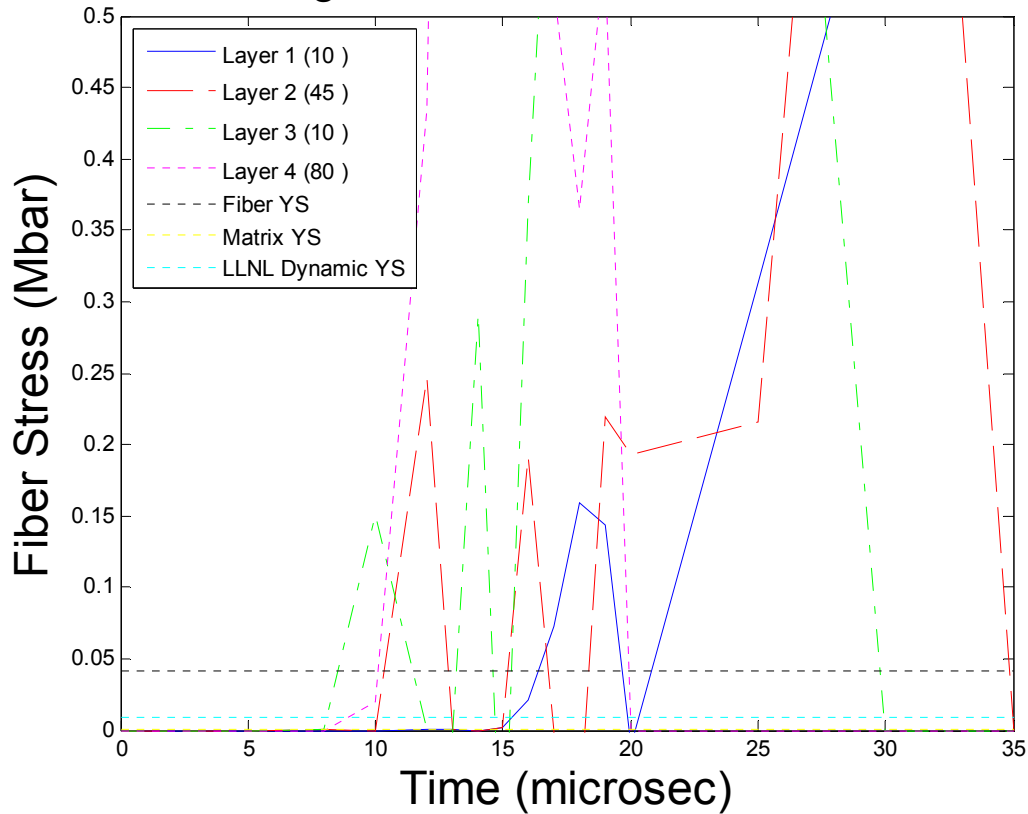


Figure 51. Unit cell level fiber stress averaged for all unit cells along the 5 cm axial location for each layer.

Illustrated in Figure 46, the elements at an axial location of 10cm (Figure 50) experienced an insignificant amount of stress until about 7 to 10 microseconds, when the detonation front reached this location. At this point, fibers in layers 2, 3 and 4 experienced the most stress, primarily due to bending and the deformation of the case above this axial location.

Similarly, the detonation front advanced to the 5cm axial location (Figure 51) at a time of approximately 15 microseconds. By this time, a large portion of the upper half of the case had failed and deformation had put the lower portion of the case in bending. Although significant stress was experienced by all layers with the exception of the innermost layer (layer 1) prior to the detonation front advancing to this portion of the case, the case appeared to be intact. The stresses observed in Figure 51 were based on the original mesh at the onset of

the HE detonation. By this time in the simulation, some of the elements had split and re-meshed as advection of the material occurred. These elements were re-numbered, but were not accounted for in the time history plots. This reduced the accuracy of the fiber stresses observed at the 5 cm axial location. When implementation of the CFC failure model is finished, a more accurate mapping of time history variables will also be incorporated. Additionally, it is evident from Figures 49 to 51 that the fiber stresses reached values significantly higher than practical prior to failure. An accurate failure model will better approximate the fiber stresses prior to failure, and a higher mesh resolution will provide better data around the eroded zones as the case fails.

D. ALE3D MODEL CONCLUSIONS

Although accurate results of the CFC will only be achieved once a failure model has been established, this preliminary model demonstrates the realistic physical results of the CFC case subject to high explosive loading, as observed in Figure 52. Additionally, calculation of the theoretical composite elastic modulus was performed with Kwon's code and compared to the LLNL case actual elastic modulus as measured during the quasi-static compression tests. Table 8 shows good correlation between the model and the experimentally determined values, with a maximum error of 5.9%. Considering the model used for this work was simplified, refinement of the CFC properties to include additional layers for added strength and stiffness should result in more accurate CFC case performance. The current model demonstrates that the carbon fiber composite has the potential to out-perform metal cases in strength-to-weight ratio and containment time once these modifications are made.

Table 8. Comparison of Elastic Modulus between the experimentally determined LLNL results and Kwon's Model.

	LLNL Experimental Results (GPa)	Model Prediction(GPa)	Error (%)
Axial	21.9	23.2	5.9
Hoop	18.1	17.7	-2.2
Radial	12.3	12.9	4.9

The composite case model did not demonstrate containment times similar to experimental cases; however adjustment of the case geometry to better reflect actual CFC cases, by increasing the number of layer repeats, for example, may see increased hold times. Also, once a failure model is developed for the CFC case a better approximation of containment time may be achieved, since it has been established that the fracture model is dependent on mesh size. For this analysis, increasing the mesh resolution by a factor of 2 caused the hold time of the equivalent-thickness steel case (with failure model) to increase by 6.7%. No significant change in hold time was observed for the model with reduced mass.

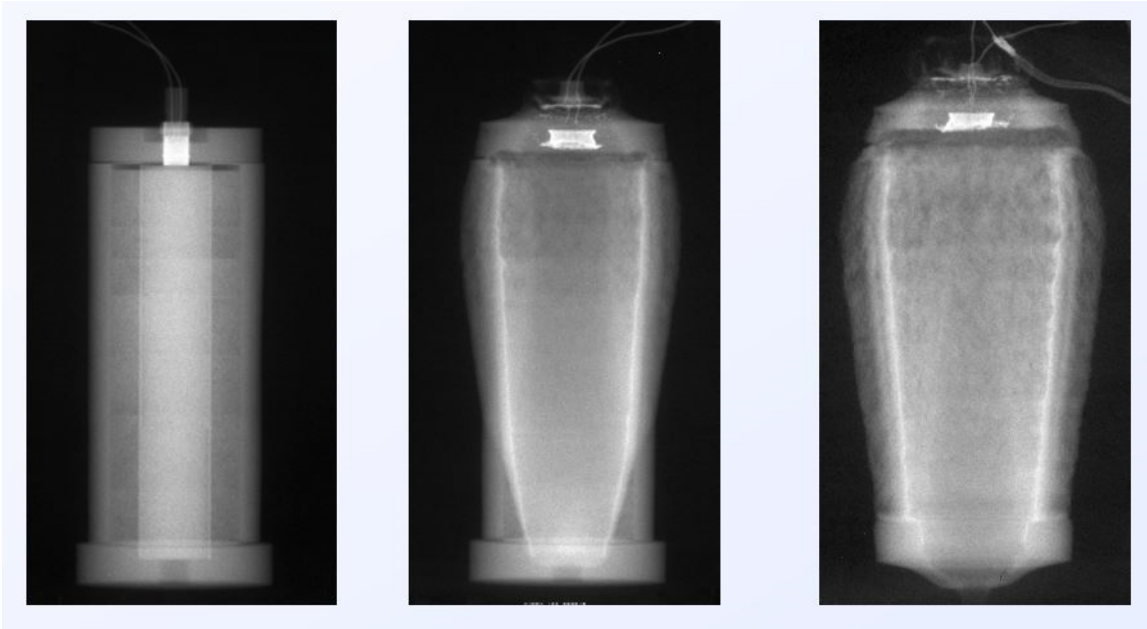


Figure 52. Hydra radiographic time sequence of carbon fiber composite case containing high explosive payload, from [4].

VI. CONCLUSIONS

In support of LLNL EMC's ongoing ADW research, this thesis developed and implemented a carbon fiber composite model utilizing ALE3D and Drs. Kwon and Park's micromechanics composite code. Several different case configurations were analyzed for comparative strength and time to failure. Realistic preliminary results were obtained, setting the stage to incorporate a composite failure model and further adjust and analyze the properties of carbon fiber composites (CFC) to achieve the optimal case performance for the desired application. Additionally, material compression testing of several CFC samples enhanced the accuracy of the model by providing low and high strain rate experimental data. This carbon fiber model provides valuable dynamic data in support of Lawrence Livermore National Laboratory's Agent Defeat Penetrator Project for the Defense Threat Reduction Agency.

A. EXPERIMENTAL TESTING REMARKS

As expected, the properties of anisotropic carbon fiber composites, to include the stress-strain relationship and the yield strength, were highly strain rate dependent. The failure modes were dependent on sample orientation and test type, as summarized in Table 9. Consistently, both quasi-static and dynamic compression tests resulted in shear failure when the CFC was loaded radially and delamination when the CFC was loaded circumferentially or axially. Pendulum impact tests resulted in delamination between the composite layers or fiber breakage, depending on orientation as well as the fabrication method. The delamination and fiber breakage occurred because the sample supports allowed for sample bending upon impact. Failure modes of the samples were consistent with those found in recent literature [6].

Samples subjected to radial compressive loading consistently exhibited the highest strength, toughness and fracture toughness values for both cases. Generally, the CFC structure is strongest when the load is applied parallel to the

fiber orientation [16]. Since the LLNL CFC contains most fibers aligned closer to the axial direction, this axial orientation is significantly stronger than the circumferential direction. Additionally, interfaces between the composite layers were formed when the filament winding manufacturing process changed winding orientations in the LLNL case. These interfaces were one of the weakest points in the composite. Loading the CFC samples axially or circumferentially applied stress parallel to these interfaces and caused delamination failure. The radial orientation applied stress perpendicular to the interfaces and resulted in the greatest yield strength.

Table 9. Summary of failure modes of carbon fiber cases for various experimental tests.

Sample Orientation		Primary Failure Mode
Compression Testing		
KAFB Case 1	Circumferential and Axial	Delamination between layers (layer separation)
	Radial	Shear failure/ Fragmentation of composite
LLNL Case 2	Circumferential and Axial	Delamination between layers (layer separation)
	Radial	Shear failure/ Fragmentation of composite
Hopkinson Pressure Bar		
KAFB Case 1	Circumferential	Delamination between layers (layer separation)
	Radial	UNK
LLNL Case 2	Circumferential	Delamination between layers (layer separation)
	Radial	Shear failure/ Fragmentation of composite
Izod Impact Testing		
KAFB Case 1	Circumferential	Fiber Breakage
	Radial	Fiber Breakage
LLNL Case 2	Circumferential	Fiber Breakage
	Radial	Delamination between layers (layer separation)

B. ALE3D MODELING REMARKS

This thesis was the first successful attempt at NPS to utilize ALE3D for research work. A steel case with HE fill detonated at TDC was developed into a working model with the help of LLNL using a combination of Lagrangian and

Eulerian principles. Once the steel case model was functioning as expected, Drs. Kwon and Park's micromechanics model for composite structures was integrated into ALE3D as a user-defined subroutine and the steel model was modified to use a cylindrical multi-layer composite. Although currently lacking a failure model, the integrated code successfully demonstrated realistic results using quasi-static yield strength and properties associated with the carbon fiber and epoxy resin type utilized by LLNL winding facility. This was demonstrated first by the accurate micromechanics model calculation of the CFC elastic modulus in three principle directions, as compared to the experimentally determined moduli. Second, the CFC ALE3D model demonstrated reasonable radial expansion, Von Mises stress, hoop stress, and containment time as compared to the steel cases. Last, fiber stress at the unit cell level followed reasonable trends with respect to fiber orientation and proximity to the detonation location.

C. RECOMMENDED FUTURE WORK

Several approaches exist when meshing a dynamic problem in ALE3D. The chosen method for this thesis was to use a combination of Lagrangian and Eulerian approaches by meshing air around the case and allowing for the case material to advect as the detonation progressed. This resulted in material moving through the mesh, so that gases could escape from the case. Also, this approach causes advected material to exhibit eroded zones due to lost mass.

Another way to simulate this problem is to mesh it completely Lagrangian by modeling the pipe bomb case embedded into a Lagrangian background mesh of air or void and the explosive. In this manner, the damage parameters would never need to advect, yet product gases would still be allowed to "escape" in the background. This method would potentially allow for better detail around the fragmented case, with less mass lost. This functionality will be improved upon in the next version of ALE3D, scheduled to be released in early 2015.

Additionally, once the CFC failure model is fully functional, the ALE3D simulation can be used to vary CFC fiber orientation, layer numbers and volume

fraction to determine the optimal configuration to achieve a desired containment time. This ideal case can be manufactured and tested for comparison to the ALE3D model. Once it is established that this simulation accurately models the experimental results, the CFC simulation will then allow for future alterations to the case with fewer expensive experimental tests required.

APPENDIX A. CALCULATIONS FOR CONTROL SAMPLE (HY-80 STEEL) TO DETERMINE TEST MACHINE COMPLIANCE

Test machine compliance was determined by running a SATEC Instron compression test on a sample of HY-80 steel under the same test conditions as the CFCs. The compliance was related through the relationship [13]:

$$\begin{aligned} S_{equivalent} &= S_{machine} + S_{specimen} \\ \frac{1}{C_{equivalent}} &= \frac{1}{C_{machine}} + \frac{1}{C_{specimen}} \\ C_{machine} &= \frac{1}{\frac{1}{C_{equivalent}} - \frac{1}{C_{specimen}}} \end{aligned} \tag{1.8}$$

where stiffness is the inverse of compliance. The known modulus for HY-80 steel was used as the specimen compliance; the equivalent compliance is given by the linear elastic region of the stress-strain data.

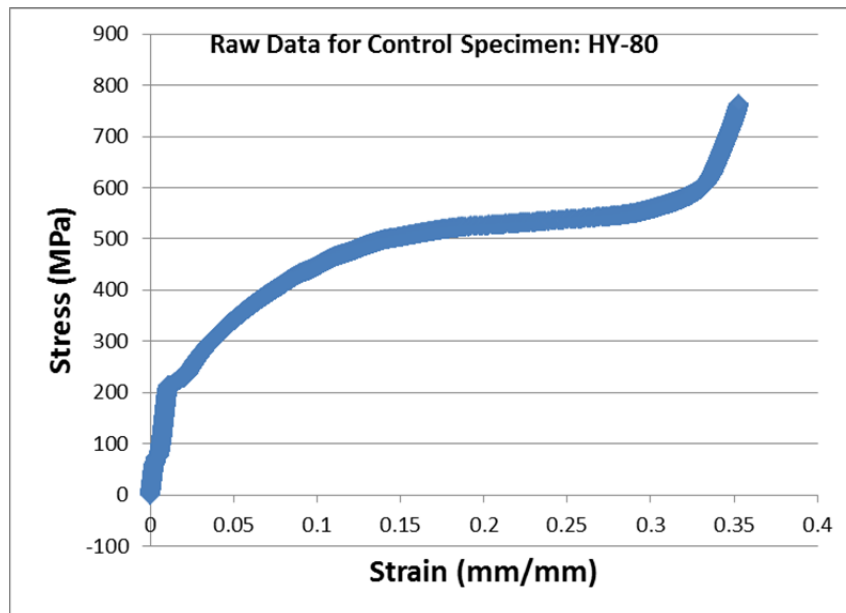


Figure 53. Plot of compression stress-strain data as-received from SATEC test. This data includes test machine compliance and requires “toe compensation.”

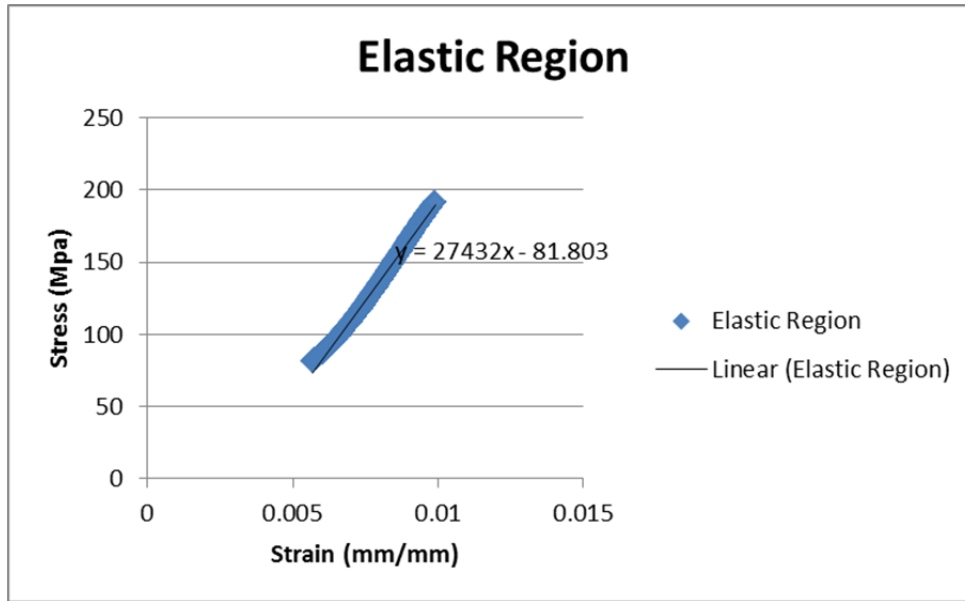


Figure 54. Determination of equivalent young's modulus from linear elastic region of raw data. The trend line is utilized to provide toe compensation.

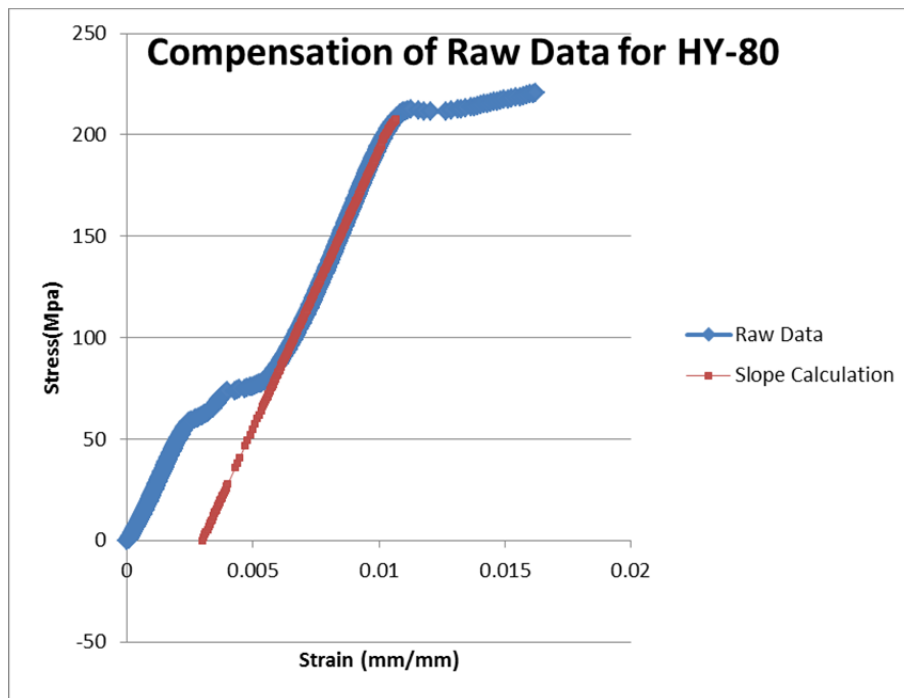


Figure 55. Graph showing corrected data as compared to raw data. Note the non-linear region at the “toe” of the graph due to slack in the machine and alignment of the specimen. To achieve the correct yield strength, this artifact must be compensated for and a new “zero point” established [15].

From the equivalent modulus calculated from Figure 28, the machine compliance was determined:

(1.9)

$$\frac{1}{C_{equivalent}} = \frac{1}{C_{machine}} + \frac{1}{C_{specimen}}$$

$$C_{machine} = \frac{1}{\frac{1}{27.432GPa} - \frac{1}{213.8GPa}}$$

$$C_{machine} = 31.427GPa$$

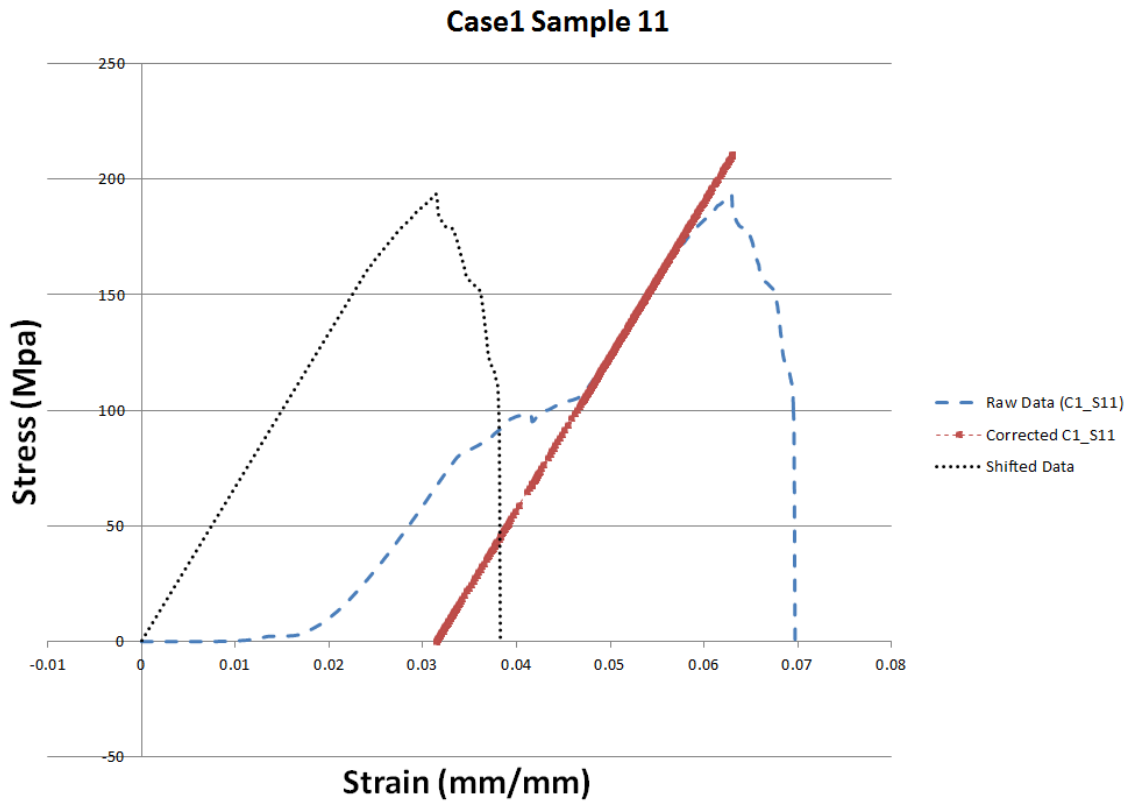


Figure 56. Graph illustrated Raw Data (blue dashed line), corrected elastic region (red dot-dashed line) and final, shifted data (black dotted line) for a carbon fiber composite sample.

THIS PAGE INTENTIONALLY LEFT BLANK

APPENDIX B. ADDITIONAL EXPERIMENTAL RESULTS

A. LLNL CASE 2 “SCRAP” SAMPLE RESULTS



Figure 58. Image of LLNL case 2 “Scrap” samples following impact testing. Similar to actual samples, Scrap samples 1 through 4 show similar failure as case 2 samples 1 through 3. Scrap samples 1 through 4 were struck radially and demonstrated significant delamination between carbon fiber winding layers. Samples 5 through 7 closely resemble actual case 2 samples 4 and 5. These were struck circumferentially and exhibited fiber breakage. Scrap sample 6 was mechanically separated by hand to better examine fiber.



Figure 59. Image of LLNL case 2 "Scrap" samples following impact testing.

Table 10. Summary of IZOD test results for set of LLNL case 2 "scrap" samples. Even though geometry does not match Izod ASTM standards, the standard deviation among fracture energy results is small.

	Sample Number	Orientation of Strike	Dimensions	Energy (J)	kJ/m ²	J/m
			(W x D) (mm)			
"Scrap" Composite Case Sample	1	Radial ID	7.71 x 7.71	9.5990	161.4800	1245.0100
	2	Radial ID	7.66 x 7.69	11.8550	201.256	1547.660
	3	Radial ID	7.69 x 7.69	11.1660	188.819	1452.020
	4	Radial ID	7.7 x 7.69	11.0950	187.390	1441.030
	5	Hoop	7.62 x 7.68	7.9930	136.583	1048.950
	6	Hoop	7.69 x 7.73	7.5724	127.388	984.710
	7	Hoop	7.71 x 7.72	7.4110	124.511	961.229
	Avg Radial			10.9288	184.7363	1421.4300
	STD Dev (Radial)			0.9505	16.7079	126.9881
	Avg Hoop			7.6588	129.4940	998.2963
	STD Dev (Hoop)			0.3005	6.3055	45.4113

APPENDIX C. ADDITIONAL ALE3D CODE

A. CFC CODE AND NOTES

DB: Steel_madj_nofail_final_001.00358
Cycle: 358 Time: 5.0034

Mesh
Var: mesh_3d

Pseudocolor
Var: p

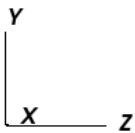
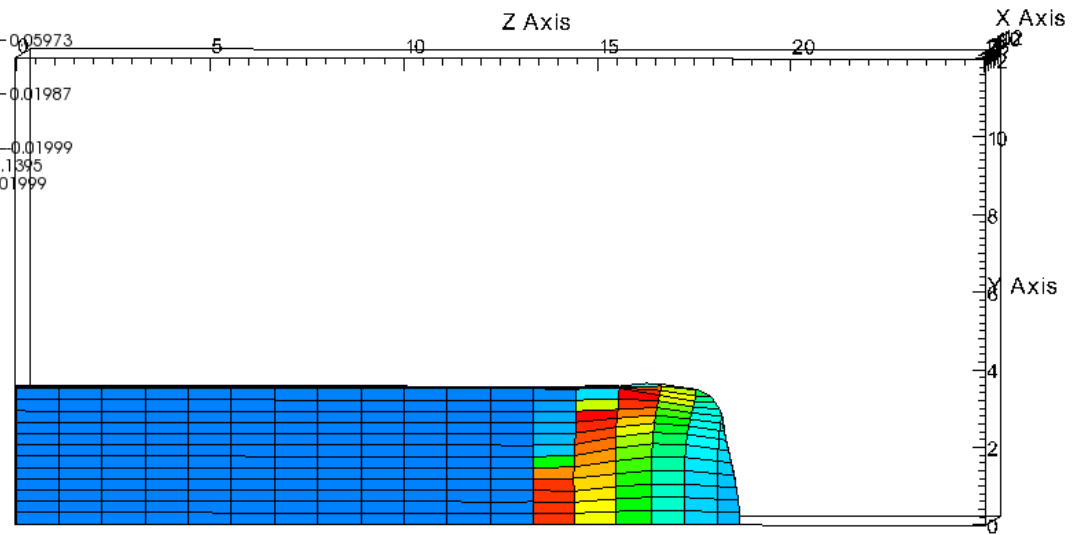
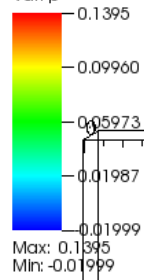


Figure 60. Internal (C4) pressure distribution for the thin steel case with no failure model at a time of approximately 5 microseconds.

DB: Steel_madj_fail_coarse_001.00359
Cycle: 359 Time: 5.00965

Mesh
Var: mesh_3d

Pseudocolor
Var: p
0.1400
0.1019
0.06385
0.02578
0.01229
Max: 0.1400
Min: -0.01229

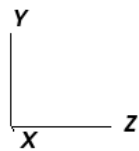
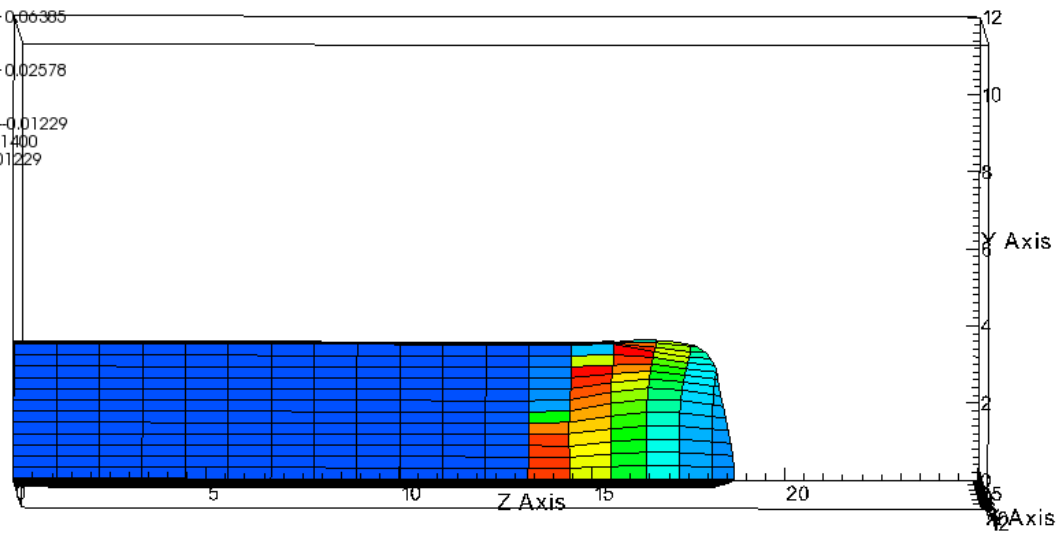


Figure 61. Internal (C4) pressure distribution for the thin steel case with failure model at a time of approximately 5 microseconds.

DB: Steel_fail_coarse_001.00090
Cycle: 90 Time:5.03493

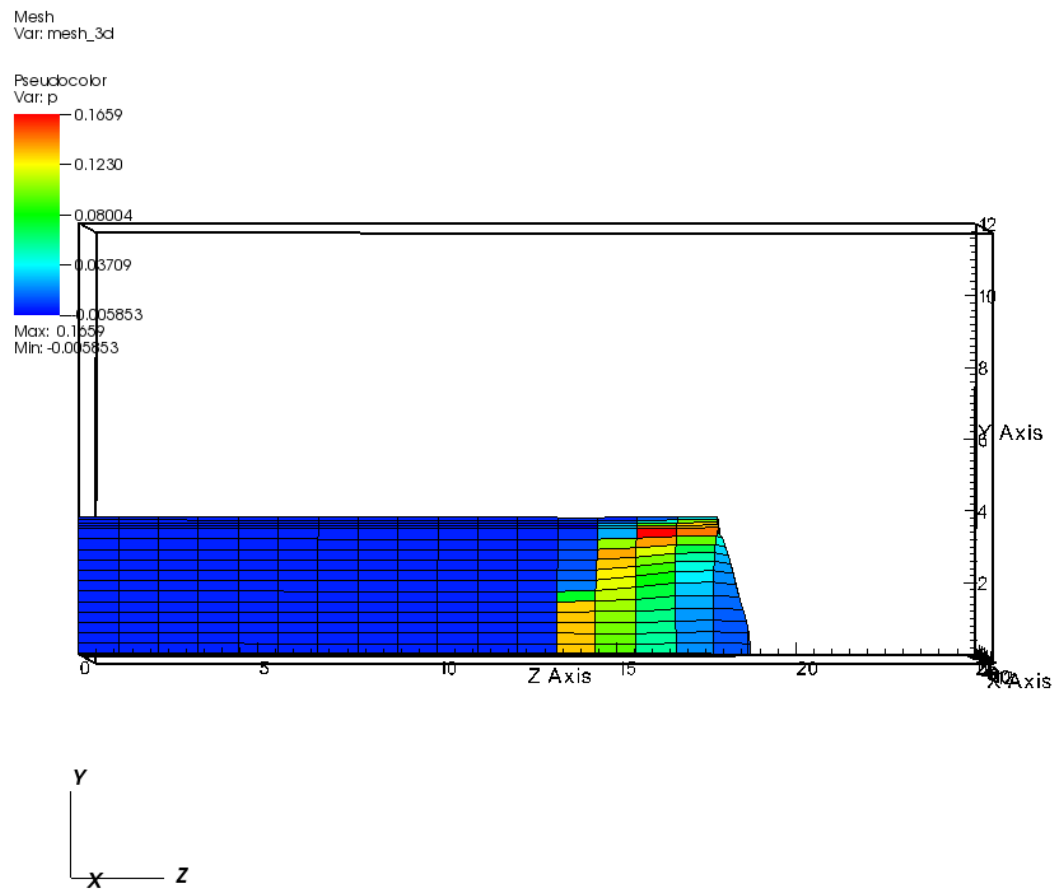


Figure 62. Internal (C4) pressure distribution for the thick steel case with failure model at a time of approximately 5 microseconds.

DB: Steel_nofail_coarse_001.00089
Cycle: 89 Time: 5.01814

Mesh
Var: mesh_3d

Pseudocolor
Var: p

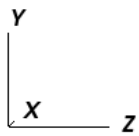
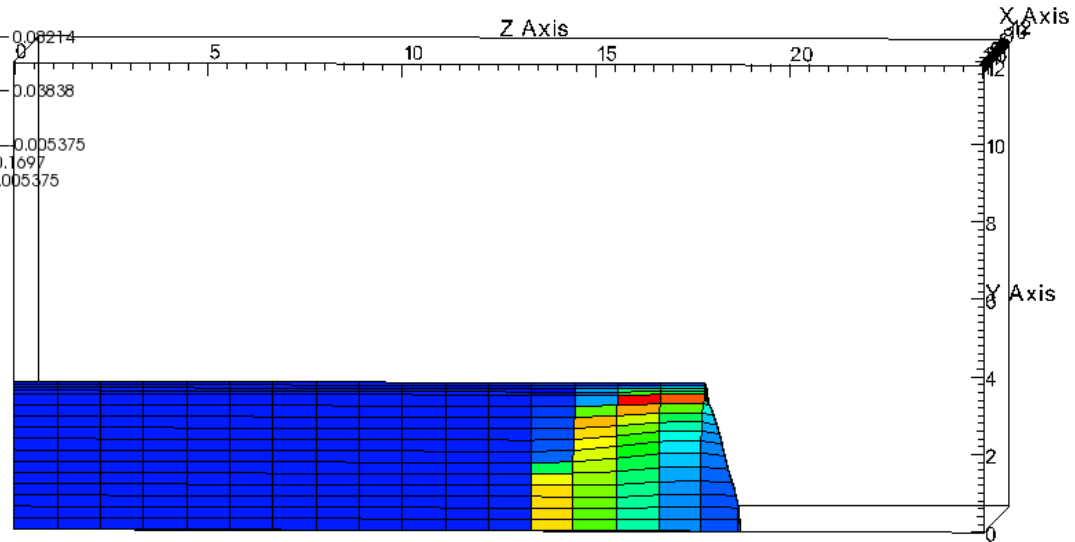
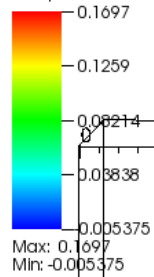


Figure 63. Internal (C4) pressure distribution for the thick steel case with no failure model at a time of approximately 5 microseconds.

B. CFC ALE3D INPUT CODE

```
#####
#####
# Multi-layer Composite cylinder mesh With C-4 center
# Initiation point occurs at TDC of C-4
#
# Notes: Reference page numbers are found in ALE3D manual volume 1 or 2
# ALE3D class notes, or ALE3d class examples (as specified)
#
# Geometry: 4 layers, with fiber orientations of 10, 45, 10, 80 degrees
#         Composite properties per Kwon's email (16Jan15) as follows:
#         model vf Efl vf12 Em   vm   afl   afm
#         2 0.50 2.2 0.11 0.035 0.36 5.0 54.0
#         shear mod 0.04
#         density of LLNL case 2 measured to be (AVG) 1.517 gm/cm^3
#
# units: cm, gm, us, Mbar, EU
#
#####
#####

#####
#####
# Defined parameter block
#####
#####
def mres 30 # mesh resolution
def dim 3 # dimensionality
def boxsize 25.

#####
#####
# CONTROL parameter block
#####
#####
CONTROL

# Stop time/ stop cycle
stoptime 40

#log message every 10 cycles
notify 10

# initial time step (V1 pg 157)
```

```

dtinit 0.01
  e_cut 1e-15 # energy cutoff
  p_cut 1e-15 # pressure cutoff
  q_cut 1e-15 # artificial viscosity cutoff
  u_cut 1e-15 # velocity cutoff
END

#####
#####
# HYDRO parameter block
#####
#####

HYDRO
# quadratic q for mixed zones
  czerox 2.0

# linear q for mixed zones
  qfbx 0.0

# use sound speed for q calculation for mixed zones
  linqflag 1

# Set Courant prefactor to just below 2/3
  courant .6

# presseq = 0 => do not equilibrate pressure
# = 1 => shockImpedance (ss) = 0.0
# = 2 => bulkImpedance (ss**2) = 0.0
# = 3 => everything
  presseq 3
  voidseedopt 1
  voidseedcrit damage
  voidseeddam 0.99
  voidseedrelv 1.03
END

#####
#####
# OUTPUT parameter block
#####
#####
OUTPUT
# plot every until
  plottime 1 100

```

```

# plot at cycles 0 and 1
  plotac 0 1
# restarts every until
  dumpcycle 100 100000

# plot tracer locations
  atcycle 1 plot_tracers 1
  atcycle 2 plot_tracers 0

# plot all nodesets until t=1
  nodesetplot * 1.0
  timehist_fileext .ult
  timehist_group_begin dataset

# tracer particle located at ignition point
  tracer_fixed tr1 0 0 17.7
  timehist p tracer tr1

# Calculating hoop stress
  derivedvar sxx diff sx p # total x-stress
  derivedvar syy diff sy p # total y-stress
  derivedvar sz0 constantzonal 0.0 # Dummy zone variable
  derivedvar hoop magnitude sxx syy sz0 # Hoop stress assembled from total x
& y stresses

  for theta = 0 45 90
  for th = 0 5 10 15 17.7 20
    tracer      ss<<theta_count>>_<<th_count>>      {3.6*cosd(<<theta>>)}
{3.6*sind(<<theta>>)} <<th>>
    timehist fun2j tracer ss<<theta_count>>_<<th_count>>
      # Time history plot of von mises stress at 0, 45 and 90 deg
    timehist x   tracer ss<<theta_count>>_<<th_count>>
      # Time history plot of x coordinate at 0, 45, 90 degrees
    timehist y   tracer ss<<theta_count>>_<<th_count>>
      # Time history plot of y coordinate at 0, 45, 90 degrees
    timehist p   tracer ss<<theta_count>>_<<th_count>>
      # Time history plot of p at 0, 45, 90 degrees
    timehist hoop tracer ss<<theta_count>>_<<th_count>>
      # Time history plot of Hoop Stress (I hope!) 0, 45, 90 degrees
  endfor
  endfor

  timehist_group_end
END
#####

```

```
#####
# ADVECTION parameter block
#####
#####
ADVECTION

# Use "modequipotential" method by B.I. Jun (used in blast3D and vent)
rlxmethod 5
# Least restrictive node motion constraint
rlxdxopt 3
# Allow relaxation to take place immediately (before node even has velocity)
rlxumin 0
# starting position for relaxation calculation is pre-lagrange
rlxginit 1
# advection time step control
advdtcon 0.5
# advection starts on cycle 1
advcycle 1.
# relaxation distance constraint - start small
rlxdxmnf 0.05
atcycle 100 rlxdxmnf 0.3
# weight equipotential relaxation based on q (follow shocks)
#      variable floor min-wgt max-wgt
rlxweightvar q 0 1 5
# at 1000 rlxweightvar q 0 1 1
# Convert "lost" Kinetic Energy to internal energy
fracke 1
END
```

```
#####
#####
# BURN parameter block
#####
#####
BURN 2 #burning c4 region
#burn velocity (From class example "vent.ain") for a C4 burn
bvel 0.819
# Defining the detonation point
detx 0
detz 17.7
dety 0
delay 0
END
```

```
#####
```

```
#####
# MESH
#####
MESH
# refining the mesh
    def res 1
#Notes: Remember that fracture model is mesh-size dependent!

# defining variable parameters
    def steel_rad {3.81}
    def rad4 {3.7306}
    def rad3 {3.652}
    def rad2 {3.5719}
    def tnt_rad {3.4925}
    def air_rad 12
    def det_rad 0.4
    def pipe_length 17.8
    def height {boxsize}
    def frust_length 2
    def det_length 1

# multi-shell/layer cylindrical mesh full depicting 3 different regions
    mcyllinder name body type quarter
    region_rad 2 7 8 9 10 3
    region_rad 3 3 3 3 3 3
        translate 0 0 0
        elems_core {4*res} # blocks in core
        elems_rad {12*res} {res} {res} {res} {res} {16*res} # blocks in each
radius
        elems_axi {16*res} {(height-pipe_length)*res} # blocks in length
        radius {tnt_rad} {rad2} {rad3} {rad4} {steel_rad} {air_rad} #
assigning parameters to each actual radius
        length {pipe_length} {height} # actual length

## Change the following boundary condition as you add/subtract layers. The
#number is associated with the outermost radius as the outflow surface. "outcyl"
#is the outflow nodeset

surface r 6 ns outcyl

spacetable sp 1.0 xabs 0 xy 0.0 0.0 expr2d x y y/sqrt(x*x+y*y)
spacetable cp 1.0 xabs 0 xy 0.0 0.0 expr2d x y x/sqrt(x*x+y*y)
END

#####
```

```
#####
# BOUNDARY parameter block
#####
#####
BOUNDARY

# Symmetry plane through x=0 (symx)
symmetry x 0.0
# Symmetry plane through y=0
symmetry y 0.0
# Symmetry plane through z = 0 (symz)
symmetry z 0.0

# Constrain "walls" of box for OUTFLOW
nodeset zmax zplane {height}
          outflow zmax          0.0 0.0          1 1 0          1
#Notes for prevline          (inflow energy density) (Relax in x,y,z) (Flag-> no
inflow)
          outflow outcyl          0.0 0.0          0 0 1          1
#Notes for prevline          (inflow energy density) (Relax in z only) (Flag-> no
inflow)

pres_continuous zmax
non_reflecting zmax
END

#####
#####
# REGION
#####
#####

REGION 3 # void/air
  matname air
  advinput advmat 1 rlxwmat 1.0 rlxumat 0.0
END

#REGION 2 # alum
# matname Alum6061
# advinput advmat 1 rlxwmat 4.0 rlxumat 1.0e-3
#END

# Kwon's Composite model: adjusting geometry for cylinder (as opposed to flat #
composite plate) with the use
# of coordinate transformation and space table.
```

```

REGION 6
matname umat530
advinput advmat 1 rlxwmat 4.0 rlxumat 1.0 rlxtmat .7
END
if gen begin
for theta = 10 45 10 80
REGION {6+<<theta_count>>} # Composite
matname umat530
  advinput advmat 1 rlxwmat 4.0 rlxumat 1.0 rlxtmat .7
  reginit f_11 spacetable sp const {-cosd(<<theta>>)}
  reginit f_12 spacetable cp const { cosd(<<theta>>)}
  reginit f_13          const { sind(<<theta>>)}
  reginit f_21 spacetable sp const { sind(<<theta>>)}
  reginit f_22 spacetable cp const {-sind(<<theta>>)}
  reginit f_23          const { cosd(<<theta>>)}
  reginit f_31 spacetable cp const 1.
  reginit f_32 spacetable sp const 1.
  reginit f_33          const 0.
END
endfor
endif

if { maincode and init } begin
for theta = 10 45 10 80
REGION {6+<<theta_count>>} # Composite
matname umat530
mergeinput mergeto 6
END
endfor
endif

REGION 2 # C4
  matname C4
  advinput advmat 1 rlxwmat 2.0 rlxumat 2.000E-05 rlxtmat .7
END

REGION 1
matname ms_steel
advinput advmat 1 advtmat 0 rlxtmat .5 rlxwmat 10 rlxumat 1
#      advinput advmat 1 rlxwmat 0 rlxumat 2.000E-05
# from fragcy.ain file - JC failure model
#Johnson-Cook Damage model with statistical distribution for D1
  reginit jc_fail_0 gaussian 0.7 0.15
# reginit jc_fail_0 const 0.7
  reginit jc_fail_d const 0.0

```

```

timehist failure vsum
timehist damage vsum
timehist failure msum
timehist damage msum
timehist failure mmean
timehist damage mmean
timehist failure vmean
timehist damage vmean
END

```

```

REGION 5
matname void
advinput advmat 1 rlxumat 0. rlxwmat 3
END

```

```

#####
# MATERIAL
#####

```

```

# air
MATERIAL Air
matinput rho 1.3e-3 e0 2.5e-6 v0 1.0 pmin 0.0
          eosvmin 1.e-5 eosvmax 1.e+2
koinput iform 5 isol 0 coef .4
end

```

```

# Steel
MATERIAL Steel
matinput rho 7.9 czero 2.0 qfb .15 crq .1
          pmin -0.027 epsfail 0.5 v0 1.0
          eosvmin 0.5 eosvmax 1.5

use ko 28
end

```

```

# C-4 (91% RDX)
MATERIAL C4
matinput rho 1.650E+00 e0 9.000E-02 v0 1.000E+00
          pmin -1.000E+00
          czero 2.000E+00 qfb 1.000E-01 crq 1.000E-01
koinput iform 1
          coef 6.054E+00 1.112E-01 4.500E+00 1.500E+00 3.700E-01
          bhe 3.000E+00 burndl -1.
          isol 0
END

```



```

# defining the material of steel
MATERIAL ms_steel
matinput rho 7.81 e0 0. v0 1. t0 300. cvav 3.559924133e-5 vhlimit 100
      linq 1 czero 2. qfb .15
msinput
ysmodel 100
elasmodel 1
  e_mod 0. poisson 0.3 shr_mod 0.801 lin_press 2.06 lin_temp 3.0e-4
  ref_temp 298.3825677 nonlinear 1
  etalolim 1. etauplim 3.8
eosmodel 304
  rhoc2 1.65 s1 1.49 g0 1.93 a 0.5
  ec0 -1.06797724e-02 ec1 -2.06872020e-02 ec2 8.24893246e-01
  ec3 -2.39505843e-02 ec4 -2.44522017e-02 ec5 5.38030101e-02
  em0 7.40464217e-02 em1 2.49802214e-01 em2 1.00445029e+00
  em3 -1.36451475e-01 em4 7.72897829e-03 em5 5.06390305e-02
  eosvmin 0.7 eosvmax 1.1
hardmodel 201
  y0 0.012 ybet 2. n 0.1 eps_0 0.
# Additional feature inserted into J-C damage model; this enables stress
# triaxiality; nonlinear from compression to tension until jc_fail_min;
# linear behavior from jc_fail_min to (histinit_jc_strength,jc_fail_min); # if not
# constant then place this in the REGION block.
failmodel 400
  healable 0 jc_fail_a .5 jc_fail_crit -1.5 jc_fail_min 0.35
  histinit jc_strength -1.
END

MATERIAL void
  matinput vhlimit 1.01
  voidinput ss0 0.2 v0 1.0 e0 0.0
END

# Kwon's Composite Material Model
if win32 begin
MATERIAL umat530
matinput rho 1.517 e0 0.0 v0 1.0 t0 293. cvav 2.e-5
msinput
ysmodel 180
  num_constants 8 num_depvars 68 umat_number 1
  shear_mod 0.04 bulk_mod 0.8
  constants
# model vf Efl vf12 Em vm afl afm
  2 0.50 2.2 0.11 0.035 0.36 5.0 54.0
  library ABAQUSUmat.dll

```

```

umat_function nps_umat2
elamodel 99
hardmodel 299
eosmodel 399
failmodel 499
END
endif
else begin
MATERIAL umat530
matinput rho 2.7 e0 0.0 v0 1.0 t0 293. cvav 2.e-5
msinput
ysmodel 180
  num_constants 8  num_depvars 68  umat_number 1
  shear_mod 0.25  bulk_mod 0.8
  constants
#  model vf  Efl  vf12  Em  vm  afl  afm
   2  0.5 0.7238 0.2 0.0275 0.35 5.0 54.0
  library ./userumat.so
  umat_function nps_umat2
elamodel 99
hardmodel 299
eosmodel 399
failmodel 499
END
endif

```

LIST OF REFERENCES

- [1] About DTRA/SCC-WMD. (n.d.). Defense Threat Reduction Agency & USSTRATCOM Center for Combating WMD & Standing Joint Force Headquarters-Elimination. [Online]. Available: <http://www.dtra.mil/About.aspx>. [Accessed 6 Jan 2015].
- [2] Agent defeat weapon- NAVY/DTRA. (2013, May 09). Global Security. [Online]. Available: <http://www.globalsecurity.org/military/systems/munitions/adw.htm>. [Accessed 12 2015 Jan].
- [3] National Research Council and the Committee on the Effects of Nuclear Earth-Penetrator and Other Weapons, *Effects of Nuclear Earth-Penetrator and Other Weapons*, Washington, DC: The National Academies Press, 2005.
- [4] J. Molitoris, Image Courtesy of LLNL EMC via private communication, Livermore, CA: Lawrence Livermore National Laboratory, Jan. 2015.
- [5] A. T. Nettles, "Instrumented impact and residual tensile strength testing of eight-ply carbon/epoxy specimens," NASA., Huntsville, Al, Rep. #2981, Jan. 1990.
- [6] P. Ma, G. Jiang, Q. Chen, X. Maio and S. Zhao, "Compression behaviors of carbon woven composites with carbon nanotube-filled epoxy resin under high strain rates," *Textile Research Journal*, vol. 85, no. 1, pp. 36–50, Jan. 2015.
- [7] S. Thirupukuzhi and C. Sun, "Testing and modeling high strain rate behavior of polymeric composites," *Composites*, vol. 29, no. 5, pp. 519-672, Sept. 1998.
- [8] D. Siromani, J. Awerbuch, and T.-M. Tan, "Finite element modeling of the crushing behavior of thin-walled CFRP tubes under axial compression," *Composites*, vol. 64, pp. 50-58, Apr. 2014.
- [9] N. Saad, M. Hamzah, and A. Hamzah, (2014). "Experimental and numerical simulation of impact fracture toughness of polyphenylene sulfide basis composite material. [Online]. Available: https://www.uobabylon.edu.iq/uobcoleges/filesshare/articles/...repository1_publication2491_29_5234.pdf
- [10] M. Kumar, M. R. Devaraj, and H. LakshmiNarayana, "Finite element modelling for numerical simulation of charpy impact test on materials," in *International Conference on Challenges and Opportunities in Mechanical Engineering, Industrial Engineering and Management Studies*, UNK, 2012.

- [11] R. Anbazhagan and G. Ragamani, "Modelling and analysis of impact properties on polyurethane composites using FEA," *International Journal of ChemTech Research*, vol. 6, no. 1, pp. 114–123, 2014.
- [12] C. Alexander, C. Key, and S. Schumacher, "Dynamic response and modeling of a carbon fiber-epoxy composite subject to shock loading," *Journal of Applied Physics*, vol. 114, pp. 1–10, 2013.
- [13] B. Baker, "Processing, microstructure and material property relationships following friction stir welding of oxide dispersion strengthened steels. (Doctoral dissertation)," Calhoun Institutional Archive of the Naval Postgraduate School., Monterey, CA, 2013.
- [14] P. Han, *Tensile Testing*, Materials Park, Ohio: ASM International, 1992, pp 1-12.
- [15] *Standard Test Method for Compressive Properties of Rigid Plastics*, ASTM Standard D695, 2010.
- [16] W. D. Callister, *Materials Science and Engineering an Introduction*, New York, NY: John Wiley & Sons, 2003.
- [17] Jordan, Foley and Siviour, "Mechanical properties of EPON 826/DEA epoxy," Air Force Research Lab., Eglin AFB, FL, Rep. AFRL-RW-EG-TP-2008-7418, Aug. 2008.
- [18] J. Courm, R. Battiste, K. Lui, and M. Ruggles, "Basic properties of reference crossply carbon-fiber composite," Oak Ridge National Lab., Oak Ridge, TN, Rep. ORNL/TM-2000/29. Feb. 2000.
- [19] American Society of Mechanical Engineers, "Split-Hopkinson Pressure Bar Apparatus: An Historic Mechanical Engineering Landmark," Southwest Research Institute, San Antonio, TX, 2006.
- [20] Split-Hopkinson pressure bar testing. (n.d.). Department of Materials Science and Engineering, University of Illinois and Urbana-Champaign. [Online]. Available: <http://hrdg.matse.illinois.edu/hopbar.html>. [Accessed 16 Jan 2015].
- [21] *Standard Test Methods for Determining the Izod Pendulum Impact Resistance of Plastics*. ASTM Standard D256, 2002.
- [22] M. Manahan and R. Stonesifer, "The difference between total absorbed energy measured using an instrumented striker and that obtained using an optical encoder," in *Pendulum Impact Testing; A Century of Progress*, ASTM STP 1380, West Conshohocken, PA, American Society for Testing and Materials, 1999.

- [23] *Model IT 504 Pendulum Impact System Instruction Book*, #04-03, Tinius Olson, Horsham, PA, 2012.
- [24] H.H. Lee, *Finite Element Simulations with ANSYS Workbench 14; Theory, Applications, Case Studies*, Mission, KS: SDC Publications, 2011.
- [25] Lawrence Livermore National Laboratory ALE3D Team, *ALE3D User's Manual*, 4.22.x ed., Livermore, Ca: LLNL, 2014.
- [26] M. S. Park and Y. W. Kwon, "Elastoplastic micromechanics model for multiscale analysis of MMC structures," *Computers and Structures*, vol. 123, pp. 28–38, 2013.
- [27] Y. Kwon and M. Park, "Versatile micromechanics model for multiscale analysis of composite structures," *Applied Composite Materials*, vol. 20, no. 4, pp. 673–692, 2013.
- [28] J. Molitoris, H. Andreski, W. Howard, M. DeHaven, R. Simpson, and R. Doherty, "Combustion evaluation of PBXIH-135, Tritonal and TNT for thermobarics and Enhanced Blast," Lawrence Livermore National Laboratory Energetic Materials Center, Livermore, CA, Rep. UCRL-TR-202329, 2004.
- [29] J. Molitoris, J. Batteux, R. Garza, J. Tringe, and P. Souers, "Mix and Instability Growth from Oblique Shock," Lawrence Livermore National Laboratory, Energetic Materials Center, Livermore, CA, Rep. LLNL-PROC-491379, Jun. 2011.

THIS PAGE INTENTIONALLY LEFT BLANK

INITIAL DISTRIBUTION LIST

1. Defense Technical Information Center
Ft. Belvoir, Virginia
2. Dudley Knox Library
Naval Postgraduate School
Monterey, California